MAGNETIC RESONANCE PHASE VELOCITY MAPPING OF CARDIAC DYSSYNCHRONY

A Dissertation
Presented to
The Academic Faculty

by

Jana G. Delfino

In Partial Fulfillment
of the Requirements for the Degree
Doctor of Philosophy in the
School of Biomedical Engineering

Georgia Institute of Technology/Emory University
August 2007

MAGNETIC RESONANCE PHASE VELOCITY MAPPING OF CARDIAC DYSSYNCHRONY

Approved by:

John N. Oshinski, PhD, Advisor
School of Biomedical Engineering
Georgia Institute of Technology/Emory University

Angel R. Leon, MD
Department of Medicine
Division of Cardiology
Emory University

Paul J. Benkeser, PhD
School of Biomedical Engineering
Georgia Institute of Technology

Oskar Skrinjar, PhD
School of Biomedical Engineering
Georgia Institute of Technology

Robert Eisner, PhD
School of Medicine
Department of Radiology
Emory University

Date Approved: 5/8/2007

ACKNOWLEDGEMENTS

First and foremost, I would like to thank my advisor, Dr. John Oshinski without whom this project would never have come to fruition. Thanks for all of your encouragement, guidance, and support, especially during the times when I didn’t believe that this project would ever come together.

I would also like to thank the other members of my committee, Drs. Benkeser, Eisner, Leon and Skrinjar. Special recognition needs to be given to Drs. Eisner and Leon for making it possible for me to conduct the majority of my imaging work on the clinical MRI scanner at Crawford Long Hospital.

I would also like to thank the MR technologists at Crawford Long, Susan Eder and Leah Mims, for helping me acquire beautiful MR images and for being patient with me while I learned my way around the Philips Intera magnet.

Thanks also needs to be given to my fellow cave dwellers: I appreciate all of you who jumped into the magnet for me on more than one occasion and were always available to bounce ideas off of. Thanks especially to Kevin Johnson and Brandon Fornwalt, for help with the phantom and strain studies respectively.

Finally, I would like to thank my husband, who affectionately became known as our “lab guinea pig” during the course of this project. In addition to your many trips into the MR magnet, I need to thank you for all of the indirect support you offered throughout the five years I worked on this project. I cannot list everything you did here, but know that I appreciate it all.

TABLE OF CONTENTS

CHAPTER 3 – AIM 1: DEVELOPMENT OF IMAGING PROTOCOL AND ANALYSIS SOFTWARE FOR MR PVM TISSUE VELOCITY IMAGES

CHAPTER 4 – AIM 2: CONSTRUCTION OF AN IMAGING PHANTOM, VALIDATION OF MR PVM SCAN ACCURACY, AND OPTIMIZATION OF ACQUISITION PARAMETERS FOR TISSUE TRACKING

CHAPTER 5 – AIM 3: COMPARISON OF MR PVM AND TDI MYOCARDIAL TISSUE VELOCITIES

CHAPTER 6 – AIM 4: DEVELOPMENT OF DATABASES DESCRIBING THE NORMAL MYOCARDIAL CONTRACTION PATTERN

LIST OF TABLES

LIST OF FIGURES

LIST OF SYMBOLS AND ABBREVIATIONS

ε	Strain
AHA	American Heart Association
CRT	Cardiac Resynchronization Therapy
LV	Left Ventricle
MR PVM	Magnetic Resonance Phase Velocity Mapping
MR	Magnetic Resonance
RV	Right Ventricle
SR	Strain Rate
TDI	Tissue Doppler Imaging

SUMMARY

Cardiac resynchronization therapy (CRT) has recently emerged as an effective treatment option for heart failure patients with dyssynchrony. Patients have traditionally been chosen for CRT based on a prolonged QRS interval. However, this selection method is far from ideal, as approximately 30% of those receiving CRT do not show any clinical improvement.

Tissue Doppler imaging (TDI) suggests that one of the best predictors of response to CRT is the underlying level of mechanical dyssynchrony in the myocardial wall prior to CRT. As a result, there has been growing interest in direct imaging of the myocardial wall. Because myocardial contraction is a complex, three-dimensional movement, providing an accurate picture of myocardial wall motion can be challenging. Echocardiography initially emerged as the modality of choice, but the long list of limitations (limited echocardiographic windows, one direction of motion, poor reproducibility) has fostered interest in exploring the use of MR for myocardial wall imaging. Although MR presents some unique drawbacks (expensive equipment, longer imaging times), it is able to overcome many of the limitations of TDI. In particular, Phase Velocity Mapping (MR PVM) can provide a complete, three-directional description of motion throughout the entire myocardial wall at high spatial and temporal resolution.

The overall goal of this project was to develop a patient-selection method for CRT based on myocardial wall velocities acquired with MR PVM. First the image acquisition and post-processing protocols for MR PVM imaging of myocardial tissue were developed. A myocardial motion phantom was used to verify the accuracy of, and optimize the acquisition parameters for, the developed MR PVM sequence. Excellent correlation was demonstrated between longitudinal myocardial velocity curves acquired with the optimized MR PVM sequence and Tissue Doppler velocities. A database describing the normal myocardial contraction pattern was constructed. A small group of dyssynchrony patients was compared to the normal database, and several areas of delayed contraction were identified in the patients. Furthermore, significantly higher levels of dyssynchrony were detected in the patients than the normal volunteers. Finally, a method for computing transmural, endocardial, and epicardial, radial strains and strain rates from MR PVM velocity data was developed.

CHAPTER 1

PROJECT SPECIFIC AIMS

Introduction

Approximately 30% of the 5 million people living with heart failure in the United States will develop a conduction delay in which the ventricles do not beat synchronously[1,2]. Cardiac resynchronization therapy (CRT) has shown promise as a treatment option for these patients who have not responded well to conventional medical therapy. To date, patients have been chosen as candidates for CRT based primarily on the width of the QRS interval on a surface electrocardiogram. However, this classification system is far from ideal as up to 30% of patients undergoing CRT do not show any improvement with treatment. Because CRT involves the implantation of a device and insertion of leads into the heart, there is a clear need for a better method to identify patients who will benefit from the procedure. Given that dyssynchrony is a mechanical delay in the contraction of the myocardial wall, directly examining the velocity of the myocardial wall may provide a better way to quantify the extent and severity of dyssynchrony. Although tissue Doppler imaging (TDI) is able to obtain myocardial velocity information, a magnetic resonance technique called phase velocity mapping (MR PVM) presents several advantages for imaging the mechanical delay of dyssynchrony. While TDI can only retrieve regional long-axis myocardial motion, MR PVM can extract *multidirectional* velocity for the *entire* myocardium, and may, therefore, be a better tool for identifying and quantifying dyssynchrony.

Specific Aims

The **objectives** of this project are to validate and optimize the MR PVM technique in a model of the myocardium, to develop a database of the myocardial contraction pattern in normal subjects, and to examine how that contraction pattern is altered in patients with dyssynchrony. The **long term goal** of this project is to utilize MR PVM to identify patients as candidates for CRT.

The specific aims of this project were to:

1) **Develop imaging protocol and analysis software for MR PVM tissue velocity images**. Develop the MR PVM scan protocol used to acquire myocardial tissue velocities. Develop post-processing software that removes background phase errors, tracks individual myocardial pixels throughout the cardiac cycle, and standardizes the LV into the AHA 17-segment model of the myocardium. *Successful completion of this aim resulted in standardized image acquisition and post-processing protocols that were applied to all collected datasets.*

2) **Construct an imaging phantom and validate the MR PVM tissue velocity scan and optimize acquisition parameters for tissue tracking.** Construct an MRI-compatible phantom model of the LV capable of controlled, three-dimensional motion. Image the motion-controlled phantom with the finalized MR PVM protocol to verify the accuracy of velocity data acquired via MR PVM. Optimize MR PVM scan parameters to produce the most accurate tracking results. *Successful completion of this aim resulted in a velocity imaging technique optimized for imaging myocardial tissue motion.*

3) **Compare MR PVM and TDI myocardial tissue velocities.** Compare myocardial tissue velocities acquired with the optimized MR PVM velocity acquisition protocol

and TDI in a group of normal volunteers and heart failure patients prior to device implantation with CRT. Compare peak velocities and time-to-peak velocities in the septal and lateral walls via a correlation coefficient and Bland-Altman analysis. Assess the reproducibility of both velocity imaging techniques in the group of normal volunteers. *Successful completion of this aim demonstrated excellent correlation between MR PVM and TDI.*

4) **Develop a database describing the normal myocardial contraction pattern**. A database describing the normal myocardial contraction pattern was constructed from a group of normal volunteers with no history of cardiac disease. The database contained the mean and standard deviation of each motion parameter (peak systolic velocity, peak diastolic velocity, time-to-peak systolic velocity, and time-to-peak diastolic velocity) in each of the three myocardial velocity directions (radial, circumferential, and longitudinal). As a proof of concept, velocity data from a small group of heart failure patients imaged prior to CRT was compared to the normal database. *Successful completion of this specific aim resulted in a database describing the normal regional myocardial contraction pattern.*

5) **Develop software for computing radial strain and SR from MR PVM velocity data**. Develop an algorithm for computing myocardial strain and strain rate from MR PVM velocity images. Compare peak strain values computed by the developed algorithm to peak strain values computed from contours drawn on cine SSFP images. Differentiate between transmural, endocardial, and epicardial strains and strain rates. *Successful completion of this aim resulted in an algorithm for computing myocardial strain and strain rate that could differentiate between transmural, endocardial, and epicardial values.*

CHAPTER 2

BACKGROUND AND SIGNIFICANCE

Cardiac Dyssynchrony

American Heart Association statistics for 2004 indicate that 5,000,000 individuals in the United States live with chronic heart failure[1]. Approximately 30% of heart failure patients develop an intraventricular conduction delay that causes the ventricles to beat asynchronously, further contributing to decreased cardiac function[2]. Cardiac dyssynchrony is usually observed in heart failure patients with dilated cardiomyopathy (both ischemic and nonischemic in origin) and left bundle branch block (LBBB). In the healthy heart, the electrical impulse initiating contraction arrives at both ventricles concurrently, and the two ventricles contract simultaneously. In patients with LBBB, the onset of electrical depolarization is significantly delayed in the lateral free wall of the left ventricle, causing this area to contract much later than normal. Since ventricular contraction time usually remain normal in the septal wall, the ventricle beats dyssynchronously[3].

Dyssynchronous contraction of the ventricular wall contributes to a decrease in systolic function. The earlier activated septal wall shortens at low stress and pre-stretches the later activated posterolateral wall[4]. As systole progresses, the late activated region develops higher load and stretches the early-activated region to limit further shortening. Late systolic stretching of the septal wall decreases ejection fraction by acting as an sink for blood that would normally be ejected[4]. The net result is a sloshing of the blood from early to late to early activated regions and a decrease in ejection fraction. In addition, the late stretch of the septal wall can break cross bridges in the contracting muscle fibers, thus diminishing the force developed during systole[4].

The contraction of the myocardial wall during dyssynchrony not only represents a net loss effect of systolic contraction, but it also causes increased energy consumption and increased wall stress in the myocardium[5,6]. The work produced by the early-activated regions is largely converted to prestretch of other regions and does not contribute significantly to ejection because ventricular pressure is low during its activation[4,6]. The late-activated free wall starts to contract at higher wall stress and also wastes work by stretching the early-activated region rather than contributing the ejection of blood[6]. Therefore, dyssynchronous activation of the myocardium results in a transfer of work from one side of the heart to the other, thereby reducing ejection efficiency[4]. Until recently, there was little that could be done to correct this dyssynchrony and improve the quality of life for this specific group of heart failure patients.

Cardiac Resynchronization Therapy

In recent years, cardiac resynchronization therapy (CRT) has emerged as an effective treatment option for heart failure patients with dyssynchrony who are at optimal medical management. Treatment with CRT involves the implantation of a pacing device under the skin of the chest and the transvenous insertion of leads into the heart. A sensing lead is placed in the right atria, and leads that simultaneously depolarize the ventricles are implanted into opposite walls of the left ventricle. The InSync® cardiac resynchronization system (Medtronic, Minneapolis, MN) has been available globally since August 2001[7] and the Guidant Cardiac Resynchronization Therapy Defibrillator

System (Guidant Corporation, St. Paul, MN) was approved by the US Food and Drug Administration in 2002[8].

Clinical Results

Over 5,000 patients have participated in numerous observational studies, as well as several randomized, controlled trials that have demonstrated the efficacy, safety, and beneficial long-term effects of CRT[9].

The InSync trial was the first observational study of CRT as a therapy for heart failure patients. The study included 103 patients n Europe and Canada with idiopathic or ischemic dilated cardiomyopathy, in New York Heart Association (NYHA) class III and IV, with left ventricular ejection fraction (LVEF) <35% and QRS duration >150 ms[9-12]. Improvements were observed in the quality of life score (as measured by the Minnesota Living with Heart Failure questionnaire), NYHA functional class, and exercise capacity (measured by a six-minute walk distance). NYHA class improved an average of one class during the twelve month follow-up period. Although InSync was not a randomized trial, it demonstrated that the benefits of CRT exceeded traditional drug therapy (including diuretics, digitalis, ACE-inhibitors, beta-blockers, carvediol, antiarrhythmics, and amiodarone), thus encouraging further randomized, controlled trials of CRT.

InSync was followed by several randomized, controlled trials that demonstrated the efficacy of CRT. The Multisite Stimulation in Cardiomyopathy (MUSTIC) study, the Multicenter InSync Randomized Clinical Evaluation (MIRACLE), and CONTAK CD all showed that CRT patients improved clinically only during periods of active pacing. In the MUSTIC study the mean 6-minute walk distance increased 23% during the period of active pacing and improvements were seen in quality of life, NYHA functional class, and the number of hospitalizations decreased[9]. MIRACLE (n=453) reported that patients in the active pacing group demonstrated significant improvements in the quality of life score (-18.0 vs. -9.0, p=0.001), 6-minute walk distance (+39 vs +10 m, p=0.005), NYHA functional class (-1 vs 0, p<0.001), treadmill exercise time (+81 vs +19 sec, p=0.001), and peak VO_2 (+1.1 vs. +0.2 mL/kg/min, p<0.1) compared to the control group[9,13]. During CONTAK CD (n=581), peak VO_2, 6-minute hall walk distance, quality of life, and NYHA class were all significantly improved in the active pacing group, as compared to the controls[13]. The MIRACLE-ICD study showed that CRT was safe even for those patients requiring an ICD[9].

The Comparison of Medical Therapy and Pacing Defibrillation in Heart Failure (COMPANION) study was the largest study enrolled 2200 patients with moderate or severe heart failure (enrollment criteria= NYHA Class III or IV, EF<=35%, QRS>120ms and more than one hospitalization related to heart failure in the past year) between 2000 and Nov 2002[13,14]. The goal of COMPANION was to compare traditional drug therapy alone with drug therapy in combination with CRT, either with or without an ICD. Patients were randomized into one of three groups: optimal medical therapy alone, optimal medical care therapy and CRT, and optimal medical therapy and CRT with an ICD. The study was terminated prematurely for ethical reasons in November of 2002 after an independent data and safety monitoring board reported a nearly 20% reduction in all-cause mortality in the patients who received CRT, as compared to the patients receiving only medical therapy, and deemed that withholding treatment for the control group was unethical.

Mechanisms

Although the exact mechanism of CRT remains unclear, it is believed that CRT increases cardiac function by improving coordination between the ventricular walls[15,16]. It has been hypothesized that increased coordination between the ventricular walls improves systolic function by increasing LV filling time, reducing mitral regurgitation, reducing left ventricular wall stress, and triggering left ventricular reverse remodeling[16].

In many patients with an intraventricular conduction delay, atrial activation remains normal[16]. Therefore, early passive ventricular filling and atrial kick may occur simultaneously, leading to decreased filling of the left ventricle[16,17]. After treatment with CRT, the ventricles contract simultaneously, allowing the left ventricle to complete its contraction earlier, thereby increasing diastolic filling time[16]. This in turn increases systolic efficiency by allowing the ventricle to eject a larger blood volume with each contraction.

Normal mitral valve function depends on proper timing of the atrial and ventricular contraction[16]. In the presence of an intraventricular conduction delay, mitral valve closure will be compromised because the contraction of the atria is not followed by an appropriately timed ventricular contraction. If the time delay between atrial and ventricular contraction is sufficiently large, an atrioventricular pressure gradient may develop, leading to mitral regurgitation. Septal wall motion is normally timed in patients with an inter-ventricular conduction delay, even if lateral wall motion is significantly delayed, meaning that the septum has completed its contraction and is already relaxing—and actually moving away from the ventricular free wall—when the rest of the ventricle is contracting[16]. This paradoxical movement of the septum during ventricular systole decreases the efficiency of mitral valve closing by distorting the mitral valve apparatus [18].

Biventricular pacing restores mitral function by activating both walls of the ventricle simultaneously—thereby forcing the lateral free wall to contract with the septum—and ensuring that ejection occurs before the septum relaxes [16,18].

Chronically high wall stress in the ventricles is associated with ventricular remodeling. In heart failure patients with dilated cardiomyopathy, wall stress is chronically elevated, leading to progressive remodeling of the left ventricle, and further dilation. By improving global left ventricular function and making the contraction of the left ventricle more synchronous, CRT is believed to reduce left ventricular wall stress. This reduction in wall stress is believed to trigger the left ventricular reverse remodeling that is often observed in patients who respond positively to CRT [5].

It is especially important to note that the increased systolic function observed with CRT is actually accompanied by a *reduction* in global myocardial oxygen consumption[5,6]. It has been hypothesized that the left ventricular reverse remodeling observed with CRT is responsible for the diminished oxygen demand of the myocardium[5]. This is in stark contrast to the inotropic agents used to enhance systolic function which actually increase the energy demand of the failing heart[6,19].

Patient Selection

The QRS wave on a surface electrocardiogram signifies electrical depolarization. Since electrical depolarization initiates mechanical activation, the duration of the QRS interval was believed to be an electrical marker of the underlying mechanical dyssynchrony. Indeed, it has been shown that QRS duration measured on a surface electrocardiogram is a good marker for inter-ventricular dyssynchrony[20]. Therefore, heart failure patients were originally selected as candidates for biventricular pacing if they exhibit a prolonged QRS interval (usually >120ms) on a surface electrocardiogram. However, this system of selecting patients is far from ideal, as <u>up to 30% of patients undergoing cardiac resynchronization therapy do not experience any clinical improvement and are deemed as "non-responders" to the treatment[21-24]</u>.

Many attempts have been made at identifying baseline clinical parameters that consistently and accurately separate responders from non-responders[22,23,25-29]. No significant differences have been found in baseline parameters for responders and nonresponders in age[22,23,26,27], heart rate[29], gender [22,23,25-27], LVEF[22,23,25-29], medication regimen[27], duration of heart disease[22,26], NYHA function class[22,23,25,26], left ventricular end diastolic pressure[25,28,29], LV volume[22,23,26,28,29], presence of atrial fibrillation[22,26,27], pacing site[22,26], presence of LLBB[25], diastolic arterial pressure[25], aortic pulse pressure[25], left ventricular diastolic filling time[28], cardiac input[26], cardiac output[26], peak oxygen intake[26], quality of life score[23], 6-minute walk distance[23], pulmonary vascular resistance[26], or pulmonary capillary wedge pressure[26].

Studies examining electrical markers as a means of separating responders and nonresponders have produced conflicting results. Some found that responders had a longer baseline QRS interval than non-responders[25,28], while others observed that there was no difference in QRS duration between responders and non-responders prior to device implantation [22,23,25-29]. Pitzalis et al. concluded that responders had a slightly longer baseline PQ interval than non-responders[29], but other studies found no difference in the length of the baseline PR interval[22,25,28].

Investigations of non-electrical differences between responders and non-responders have produced similarly conflicting results: Oguz et al. reported that the duration of mitral regurgitation prior to device implantation was longer in responders than non-responders[28], but other studies have found no difference in the presence or degree of mitral regurgitation prior to device implantation between responders and non-responders[22,25,26,29]. It has previously been reported that non-responders were more likely to have ischemic heart disease or a history of myocardial infarction than responders, and recently it has been suggested that a larger scar burden and fewer viable myocardial segments is predicative of non-response to CRT[27,30-35]. A cutoff value of 15% total scar has been proposed as a means of predicted clinical response to CRT with a sensitivity of 85% and a specificity of 90%[33], and a significant inverse relationship has been established between total scar burden and a reduction in LV end-systolic volume 6-months post CRT[34]. In addition to total scar burden, it has been suggested that the presence of scar tissue within the posterolateral wall of the myocardium is one of the most important predictors of response to CRT[31,32]. However these conclusions have been challenged by several other studies which have found no differences in the etiology of heart disease between responders and non-responders[22,23,25,26]. Part of these conflicting findings may be due to the heterogeneous patterns of myocardial scarring found within the heart failure population[33], and the small numbers of patients enrolled in these preliminary studies.

These conflicting results highlight the inadequacy of current methods for selecting patients for CRT. Treatment with CRT is an expensive, invasive procedure involving the implantation of a pacing device and the insertion of leads into the walls of the heart. Furthermore, CRT devices can cost up to $40,000 with total hospital charges per patient approaching $100,000[36,37]. Clearly, there is a need to better identify patients who will benefit from this treatment.

One of the reasons for the relatively high percentage of non-responders to CRT could be a result of the method by which patients are identified as candidates for the procedure. CRT studies have enrolled patients primarily based on the presence of a prolonged QRS interval on a surface electrocardiogram, as it has been shown that the width of the QRS interval on a surface electrocardiogram was a good marker for *inter*-ventricular dyssynchrony[20 9,14,38,39]. However, it has since been shown that a shortening of the QRS interval does not necessarily indicate a positive response to CRT[4,26,27,40] and that heart failure patients with a normal QRS interval can also benefit from CRT[4,40-42]. These studies suggest that the QRS interval is an unreliable marker of the underlying mechanical problem either because electrical delay times and mechanical dyssynchrony in the heart are not directly related[4,9,43], or because response to CRT is based on *intra*-ventricular dyssynchrony (dyssynchrony *within* the left ventricle). In fact, some recent research suggests that intra-ventricular dyssynchrony may be important in predicting response to CRT than *inter*-ventricular dyssynchrony[44,45]. Furthermore, approximately 30% of patients with wide a QRS interval do not exhibit intra-ventricular dyssynchrony[40], which may at least partially explain the low response rates in the initial CRT trials. Therefore, a better way to quantify the extent and severity of dyssynchrony—and to select patients as candidates for CRT—is to directly examine the motion of the ventricular walls.

Normal Myocardial Wall Motion

Myocardial contraction is a complex, three-dimensional movement involving longitudinal and radial shortening, torsion and shear. During systole, the normal left ventricle shortens along the radial and longitudinal directions and twists in different directions along the length of the LV to create a wringing motion. In diastole, the motion is reversed and the ventricle returns to its original shape.

Longitudinal Motion

Longitudinal motion describes the movement of the LV along the basal-apical axis. During systole, the left ventricle shortens along its longitudinal axis, with the base of the LV moving closer toward the apex. This motion is reversed during diastole when the base moves away from the apex[46,47]. During diastolic relaxation, there is a slight overshoot of the base past its initial starting position, followed by a brief period of motion back toward the apex[46,48]. The longitudinal velocity curve shown in Figure 2.1 illustrates this motion extremely clearly. Recall that longitudinal motion is defined as positive for motion towards the LV apex and negative for motion toward the base of the myocardium. In the basal slice where the velocity curve was measured, the descent of the base toward the apex is seen as positive velocity during systole (A), and the movement of the base away from the apex during diastole is seen as the negative velocity peak (B). The slight overshoot of the base during diastolic relaxation is seen as the positive peak during diastole (C).

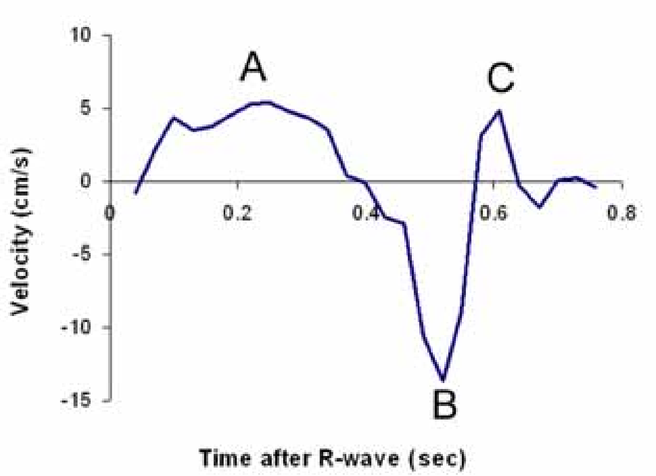

***Figure 2.1**: Longitudinal velocity curve.*

In the left ventricle, greater longitudinal displacement is observed in the lateral wall than in the septal wall, as motion in the septal wall is restricted by the right ventricle. This is illustrated in Figure 2.2 by a finite element model of myocardial contraction taken from a 1994 paper by Young et al.[49]. The end-diastolic location of the wire mesh is shown in lighter gray lines and the end-systolic position is shown by the darker lines. Note that when the LV shortens longitudinally during systole, the base moves significantly toward the apex, while the apex remains almost stationary. Also observe that longitudinal displacement is not uniform throughout the LV, with greater displacement observed in the lateral wall than the septal wall.

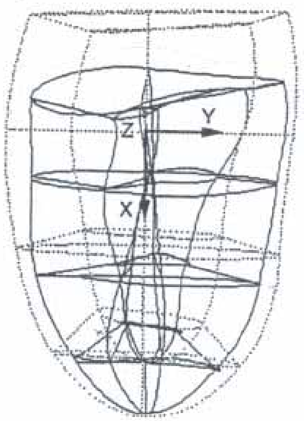

Figure 2.2*: Finite element model of myocardial displacement (from Young et al, 1994).*

Several studies have suggested that longitudinal movement is the first motion to occur during cardiac contraction. It has been documented that longitudinal fibers start to shorten before radial fibers, so both the onset of shortening and peak shortening occur in the longitudinal direction before the radial direction[47]. By M-mode echocardiography, it has been shown that long axis shortening begins 25+/-40msec earlier than short axis shortening[47], and that peak longitudinal velocity during systole occurs before peak radial velocity[47].

Radial Motion

Radial motion describes the movement of the left ventricular walls toward and away from the center of the LV blood pool. During systole, myocardial wall thickening occurs as the walls of the LV move toward the center of the blood pool. The epicardial side of the LV experiences significantly less motion than the endocardial side, as thickening occurs primarily in the endocardial layers. During diastole, the myocardial walls relax and return to their original thickness.

Figure 2.3 shows an example of a radial velocity curve from a basal myocardial slice. Motion toward the center of the LV blood pool during systole is seen as positive (A), while motion away from the center of the LV blood pool during diastole is seen as negative (B). Note that the velocity magnitudes in the radial curve are significantly lower than that of the longitudinal curve shown in Figure 6.1.

Radial displacement is fairly constant throughout the longitudinal length of the myocardium[50]. It has been suggested that there is slightly less radial displacement in the septum than in any other myocardial region[51], again on account of tethering effects from the right ventricle.

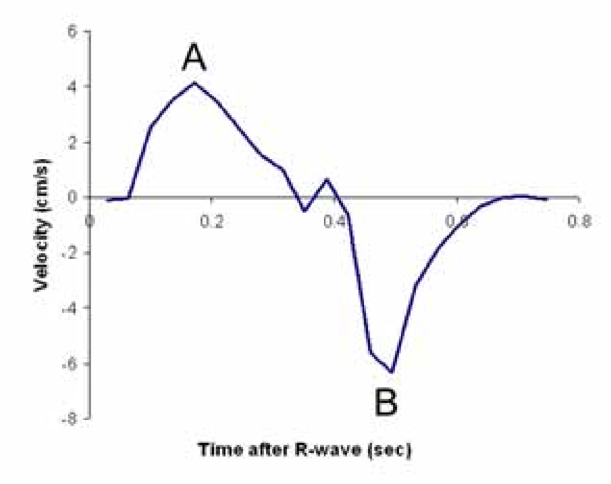

Figure 2.3: Radial velocity curve.

Circumferential Motion (Myocardial Torsion)

The twisting of the LV is the by far the most complex motion. During systole, the LV creates a wringing motion with clockwise rotation at the base and counterclockwise rotation at the apex (when viewed from the apex)[52-60]. Apical segments twist counterclockwise for the duration of systole[55-57]. In basal segments, however, there is a transition from counterclockwise twist during early systole to clockwise twist during the remainder of systole[54,57,61]. This transition from counterclockwise to clockwise twist in basal segments of the LV occurs between 45 and 60% of the duration of systole[56]. Young et al. noted that this reversal of twist occurred between the first and second frames in tagging studies (first frame =13msec after R-wave, and second frame 60-90 msec later)[49]. Consistent with this finding is that in the present study, the reversal of twist was only documented in subjects who were imaged with a trailing navigator (first frame 26 msec after detection of R-wave) and not those in whom images were imaged using a leading navigator (first frame=74msec after R-wave detection). During diastole, the twisting motion is reversed and a counterclockwise rotation is seen in the base and a clockwise rotation is observed in the apex [52-60]. There is no reversal of twist in basal slices during diastole.

A transition from the rotation of basal slices to the rotation of apical slices occurs along the long-axis length of the LV. Therefore, the pattern of twist within mid-ventricular slices is less clearly defined; rotation of the mid-ventricular slices depends on location along the length of the LV. However, it is generally acknowledged that mid-ventricular segments experience decreased twist and primarily contract in the radial direction[51,58].

Figure 2.4 shows circumferential velocity curves from a basal slice imaged with a trailing navigator. The initial counter-clockwise twist of the base was observed as a negative peak (A), peak velocity during systole is positive indicating a clockwise rotation (B), and diastolic relaxation is negative, indicating a counterclockwise rotation (C). The reversal of twist seen during early systole (transition from A to B) can only be seen when images are acquired with a trailing navigator.

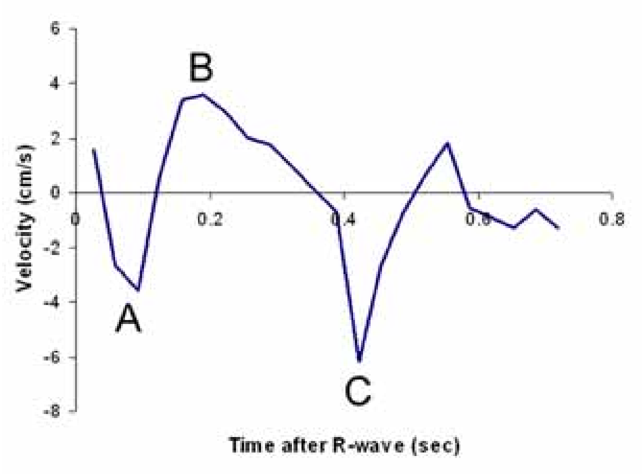

Figure 2.4*: Circumferential velocity curve from a basal myocardial slice*

During systole, torsion develops within the left ventricle primarily during isovolumic contraction with minimal rotation during the ejection phase[52,58,59,62]. Similarly, diastolic untwisting occurs primarily during isovolumic relaxation, before diastolic filling begins[52,58,59,62]. More specifically, it has been documented that over 80% of diastolic untwisting occurs during isovolumic relaxation (after aortic valve closure and before mitral valve opening)[52,59,61-63]. Put another way, torsion decreases most sharply *before* mitral valve opening, whereas the length of the LV increases sharply *after* mitral valve opening, supporting the hypothesis that rapid untwisting of the LV is an important mechanism in generating a suction force instrumental to rapid filling[62].

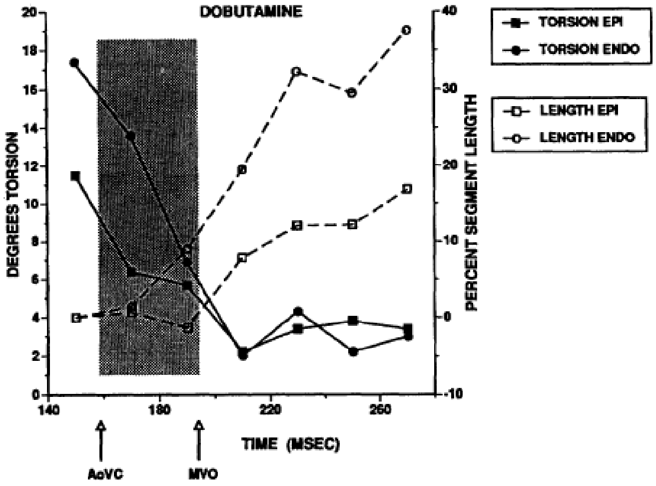

***Figure 2.5**: Dissociation between LV length and torsion (from Rademakers et al, 1992).*

Figure 2.5, which was taken from a 1992 *Circulation* paper Rademakers et al.[62], illustrates this dissociation between untwisting and lengthening in an apical slice of the LV during diastole. The figure clearly shows that the change in torsion is almost inversely related to the change in LV length. The figure only shows the period of diastole from just before aortic valve closure. Isovolumic relaxation, the period between aortic valve closing (AVc) and mitral valve opening (MVO), is shaded.

Methods to Assess Myocardial Motion and Dyssynchrony

Ultrasound imaging and Magnetic Resonance Imaging are two non-invasive methods currently available for the evaluation of myocardial motion. Ultrasound has the advantages of being more cost efficient, portable, and better able to provide images extremely rapidly. However, it is not possible to obtain ultrasound images in all myocardial regions due to interference from the bones of the rib cage or the lungs. Magnetic resonance imaging has the advantage of being able to image the entire heart without the anatomical restrictions encountered by ultrasound, but MR imaging is much more costly, generally takes longer, and is not portable.

Ultrasound Imaging

Conventional echocardiography

Echocardiography is a well-established clinical tool for the noninvasive assessment of regional and global LV function. B-mode echocardiography is generally not used for quantitative evaluation of myocardial motion. Echocardiographic methods for measuring LV dyssynchrony include M-mode measurement of the septal-to-posterior wall motion delay (SPWMD)[64], Fourier phase angle analysis of wall displacement[65], and calculation of regional fractional area changes using contrast imaging[66]. The septal-to-posterior wall motion delay, SPWMD (defined as the delay between the motion of the septum and left posterior wall), was shown to be predictive of a positive clinical response to CRT (responders baseline SPWMD = 246+/- 68 ms, non-responders baseline SPWMD = 110+/-55 ms, $p<0.001$) [29]. A SPWMD greater than 130ms could separate responders and non-responders with a specificity of 63%, a positive predictive value of 80%, and an accuracy of 85%; in contrast, the specificity of QRS duration for separating responders and non-responders in the same study was 13%, with a positive predictive value of 63% and an accuracy of 65%[29].

Although these echocardiographic techniques have shown promise in better identifying asynchrony patients, they are restricted by the use of a single imaging plane and, therefore, do not quantify dyssynchrony throughout the entire ventricle[45]. Three-dimensional echocardiography and modeling can overcome this limitation[67], but limited availability and the prolonged time required for image processing has, until very recently, limited clinical applicability.

Tissue Doppler Imaging

Tissue Doppler Imaging (TDI) is an ultrasound technique for the imaging of myocardial motion that relies on the principle of the Doppler effect: myocardial velocities are calculated based on the phase shift of the ultrasound signal reflected from the contracting myocardium. While traditional Doppler flow studies acquire the high-frequency, low-amplitude signals of flowing blood, TDI filters out these high frequency signals and focuses on acquiring the low-frequency, high-amplitude signals of the moving myocardium. Using TDI, it is possible to obtain a time-varying velocity curve for a single ventricular wall at frame rates approaching 300 Hertz. In this manner TDI can provide information on the magnitude and direction of myocardial motion.

TDI has been used extensively to measure myocardial contraction and relaxation velocities in healthy volunteers[68-70], and has also been used successfully to identify the presence of mechanical delays in dyssynchrony[18,29,44,45,71-74]. Furthermore, several studies have been successful at identifying TDI motion parameters that separated responders from non-responders based on data acquired prior to device implantation.

Most TDI measurements of dyssynchrony are based on differences in time-to-peak systolic myocardial velocity between two or more walls of the LV. For example, a septal-to-lateral delay (the difference in time-to-peak-systolic velocity between the septal and lateral wall) greater than 60ms predicted response to CRT with a sensitivity of 76% and a specificity of 88%[75]. Peak velocity difference (MaxDiff)—defined as the difference between the longest and shortest time-to-peak velocity across six regions (septal, lateral, inferior, anterior, anteroseptal, and posterior) of the left ventricle—greater than 65msec was able to separate responders from non-responders with a sensitivity of 78% and a specificity of 33%[76]. LV dyssynchrony—defined as the maximum delay between peak systolic velocity in four basal ROIs (anterior, inferior, septal, and lateral)—separated responders and nonresponders with a sensitivity and specificity of 92% when a cutoff value of 65msec was used [24].

Yu et al. extended this "time-to-peak" analysis by looking at variation in time-to-peak systolic velocity (Ts) and the standard deviation of this time-to-peak velocity (Ts-SD) in six basal and six mid-segmental myocardial regions as a measure of dyssynchrony[71,77]. Yu et al reported that the baseline Ts was significantly different for responders and nonresponders (responders = 45.0 +/-8.3ms, non-responders = 24.8+/-4.5ms, p<0.001) [18,71,77]. By quantifying Ts-SD in 88 normal subjects and taking the mean (17ms) plus two standard deviations (2 * 7.8 = 15.6ms) of Ts-SD in these normals, Yu *et al* determined a threshold value of 32.6 ms could be used to diagnose LV dyssynchrony[78]. However, multiple threshold values for Ts-SD dyssynchrony have been reported by Yu et al: the authors used a threshold of 31.4 ms to predict response to CRT with a sensitivity of 96% and a specificity of 78%[79], and in a different population of patients, a threshold of 34.4 ms was used to predict response to CRT with a sensitivity of 87% and a specificity of 81%[80].

Recently, several extensions of TDI imaging have been developed, including tissue displacement imaging and tissue synchronization imaging. The theory behind tissue displacement imaging is that a delay in time-to-peak tissue *displacement* may be more sensitive at identifying dyssynchrony than a delay in time-to-peak tissue *velocity*. TDI velocity data is acquired normally, and then tissue displacement is calculated from the underlying TDI velocity data by integration[81,82]. While some differences have been shown in the timing of displacement curves between normal volunteers, LBBB patients, and idiopathic dilated cardiomyopathy patients, no single parameter was able to clearly separate the three groups[81,82]. Tissue synchronization imaging (TSI) also uses underlying TDI velocity data, but applies post-processing in real-time to display the time-to-peak velocity as a color-coded readout. Response to this technology has been mixed, with some groups claim that TSI provides a useful display of dyssynchrony and makes it easier to identify delayed regions, and other claiming that the additional post-processing of TDI data fails to provide any additional benefit[83-85].

It has been suggested that current guidelines for patient selection for CRT should be expanded to include TDI assessment of LV dyssynchrony[44]. However, a recent study showed that the most commonly used TDI dyssynchrony parameters agree on a diagnosis of dyssynchrony only half the time[86]. Thus, despite the success of TDI parameters in predicting response to CRT in small, single-center studies, there is a lack of consensus on exactly which parameters should be used in assessing LV dyssynchrony.

In summary, Tissue Doppler Imaging has demonstrated that there are differences in the myocardial contraction pattern between responders and non-responders prior to device implantation and that some of these differences can be used to separate responders and non-responders. These findings support the idea of using baseline motion parameters to select patients for CRT. However, TDI suffers from some significant limitations: First, TDI can only retrieve velocity information for objects moving directly toward or away from the transducer, meaning that velocity information is only available for a single direction. Secondly, the acquired velocities are limited to regions that can be accessed through the echocardiographic window of the torso. Therefore, TDI is only able to retrieve local long-axis velocities for regional areas of the myocardium, usually near the base of the ventricles. While this information is useful, it is far from a complete description of myocardial motion. Thirdly, the poor reproducibility of TDI parameters may limit their clinical utility.

Magnetic Resonance Imaging

There are two categories of MR methods available for the assessment of myocardial motion: tissue tagging techniques and phase contrast techniques. In MR tissue tagging a series of signal voids is applied to the tissue prior to imaging, and the deformation of the tags is tracked throughout the cardiac cycle. Phase contrast imaging encodes myocardial motion or deformation within the spins of the myocardial tissue.

Magnetic Resonance Tissue Tagging

During myocardial tissue tagging, a series of presaturation planes are placed within the myocardium prior to MR imaging[87,88]. These planes effectively eliminate the MR signal from tissue and create a series of signal voids. Depending on the orientation and quantity of presaturation planes applied, either dark bands or grids will appear across the image. Presaturation affects the spins of hydrogen atoms within the myocardial tissue and is a property of the myocardial tissue itself. Therefore, changes in the shape of the presaturation pattern mirror changes in the shape of the underlying tissue[87,89]. If the myocardium is imaged after application of the presaturation pattern, the lines or grids will appear on the image. If a cine acquisition is used, deformation of the presaturation pattern throughout several time points within the cardiac cycle can be seen. During post-processing, deformation of the areas of presaturation can be tracked throughout the cardiac cycle to quantify myocardial tissue motion. Since the presaturation pattern can be applied in any direction and prior to any imaging sequence, the technique is very versatile.

Figure 2.6 shows an example image of myocardial tagging applied to the myocardium. Two sets of parallel tags are laid during late diastole before cardiac contraction begins (Figure 2.6A). Figure 2.6B shows how the tags within the myocardium deform with systolic contraction, but tags in regions without motion (such as the chest wall) remain parallel. Tags begin to fad early in diastole, making quantification of diastolic movement challenging, Figure 2.6C. At end-diastole, the location of tag intersections is difficult to determine, Figure 2.6D.

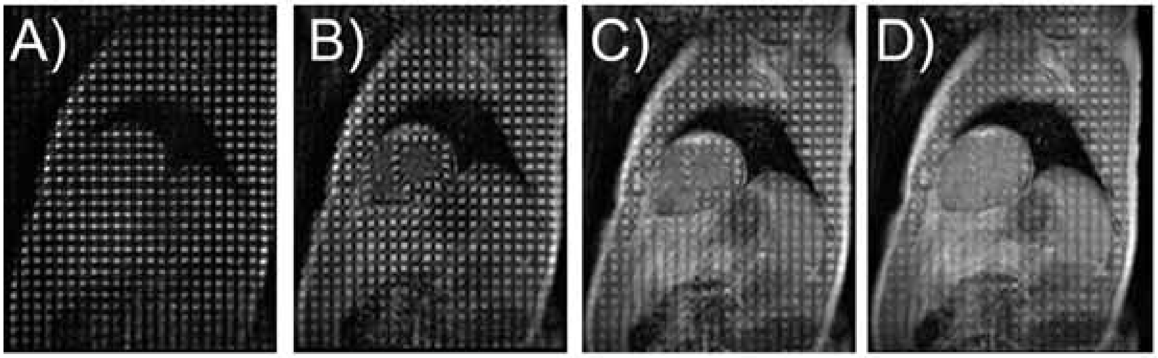

***Figure 2.6**: Example tagged MR image of the contracting myocardium.*

However, tissue tagging also has several limitations. As mentioned previously, the tag lines are dependent on the spins of individual hydrogen atoms within the myocardial tissue, so they fade as a result of T1 relaxation[88]. This makes it difficult to image diastolic events, particularly in subjects with low heart rates. In addition, the spatial resolution of the derived deformation data is limited by the number of tag intersections. Since tagging planes are usually between 5 and 7mm apart, motion information is only available for one or two material points in the myocardial wall. In addition, a major drawback of tagged MRI images has been the lengthy post-processing time. Historically, tagged MRI images have been analyzed by tracking the location of tag intersections over time, which is a tedious, time-consuming process that has been difficult to automate. Therefore, it can take up to one week to analyze data from a single imaging session[90]. Another drawback of tagged MRI is that images give information about either a single direction of motion (if parallel tags are used) or about both in-plane directions (if grid tags are used). However, without an additional image acquisition perpendicular to the first, tagging cannot provide any information about the third direction of motion.

Attempts have been made to utilize tagged MRI image data as a means of quantifying dyssynchrony, but these studies have been preliminary and have been limited by the large amount of post-processing time required to quantitatively interpret tagged MRI images. Based on tagged MRI data from mongrel dogs, Leclercq et al showed that a positive response to biventricular pacing was more dependent on the uniformity of mechanical activation in the circumferential direction than electrical depolarization within the ventricle[43]. While this result is interesting and appears to support the current ideology of decoupling between electrical depolarization and mechanical activation, the limitations of the tagged MRI data meant that no information was available about mechanical activation in the longitudinal direction and limited information was available in the radial direction.

Harmonic Phase (HARP) Analysis of tagged MR images

Harmonic Phase (HARP) analysis of tagged MR images has recently been developed in an effort to reduce the amount of time-consuming post-processing necessary to interpret tagged MRI images. Instead of relying on user input to track the movement of tag intersections in the time domain, HARP determines cardiac motion by using a bandpass filter to isolate spectral peaks of the tagged images in the Fourier domain[91]. The inverse Fourier transform of the bandpass region yields a complex harmonic image, the magnitude of which shows changes in the geometry of the heart and the phase of which gives detailed information regarding myocardial motion[92]. From the phase of this harmonic image, the HARP algorithm is able to calculate radial and circumferential strain within the myocardium.

The clear advantage of HARP is that tagged MR images can be rapidly and automatically processed. Furthermore, because HARP computes deformation from the k-space information of the image, the spatial resolution of the computed strain data is dependent on the size of the k-space filter, not on the frequency of tag spacing[91]. However, there are several drawbacks to the HARP algorithm. First, HARP is based on the analysis of 2D tagged images; since cardiac motion is three-dimensional, the derived motion parameters represent the projection of the true 3D motion onto a 2D plane[92]. Second, although HARP should be able to extract both radial and circumferential strain information from the tagged MR images, in practice, the radial strain measurements are often noisy and difficult to interpret. Thirdly, it is important to keep in mind that the HARP algorithm can only be used to extract myocardial strain, not velocity or displacement, from the tagged MR image.

Magnetic Resonance Phase Velocity Mapping (MR PVM)

Magnetic Resonance Phase Velocity Mapping (MR PVM) is a phase-contrast imaging technique based upon the principle that spins moving inside of a magnetic field accumulate a net shift in phase relative to stationary spins[93-96]. If acceleration is assumed to be constant, the change in phase of the moving spins is proportional to velocity[94]. However, phase is also affected by many other phenomena, including pulse sequence timing, magnetic field inhomogeneities, radio-frequency effects, magnetic field eddy currents, and motion in other directions besides the one being studied[93]. Therefore, a set of two images is needed to gather data for each velocity-encoded direction. A reference phase image is acquired first, and then the first moment of the gradient waveform (which is sensitive to motion) is modified for the acquisition of the second image. Both images contain all of the unwanted phase effects, but each image has a different phase shift due to motion in the velocity-encoded direction. Subtraction of the two images yields a phase difference image in which the magnitude of the phase shift is directly related to velocity in the encoded direction[94]. The result is an image in which the intensity of each pixel corresponds directly to velocity in the given direction. Through a total of four acquisitions (a reference scan and three orthogonal velocity scans), three-dimensional velocity information can be acquired. The resulting three velocity images (V_x, V_y, and V_z) provide a complete description of myocardial motion.

In the PVM images, objects moving in the direction of positive velocity appear light, while objects moving in the direction of negative velocity appear dark. The directions of positive and negative velocity are determined by the orientation of the slice and the velocity-encoded direction. Static structures experience no phase shift in the difference image and appear gray. Figure 2.7 shows an example MR PVM image of the thru-plane motion of a basal myocardial slice throughout the cardiac cycle.

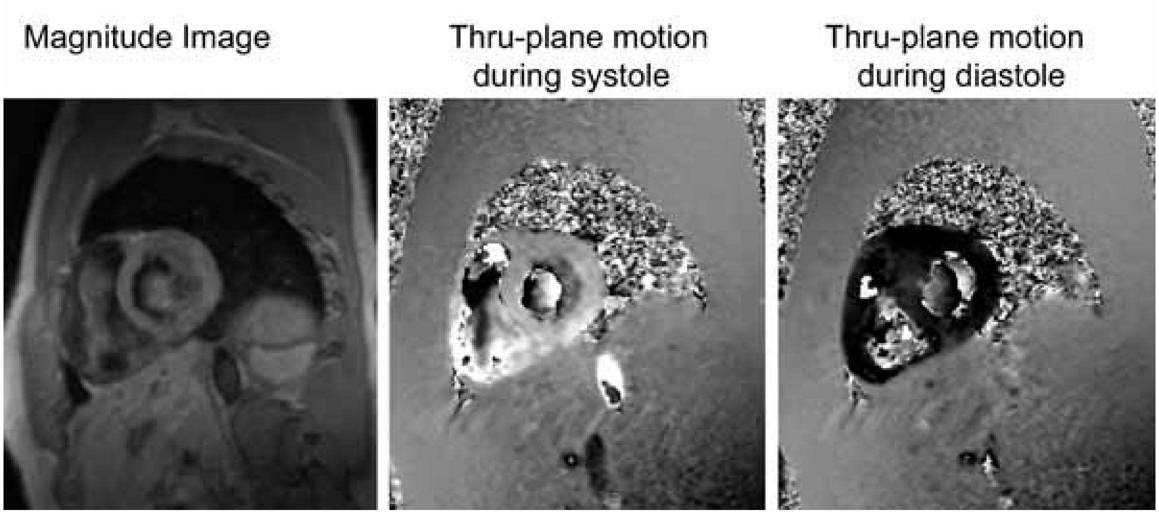

***Figure 2.7**: Example MR PVM image.*

Several features of phase velocity mapping make it especially well-suited for imaging the mechanical delay of dyssynchrony. In contrast to echocardiography, MR PVM is not limited by the acoustical windows of the chest and can acquire *multidirectional* velocity information throughout the *entire* myocardium. In addition, velocity information is acquired for each voxel within the image at the same spatial resolution as the magnitude image. Therefore, PVM is able to provide *a complete three-dimensional description of myocardial motion for the entire heart*. This allows for the analysis of three-directional motion on a pixel-to-pixel basis, making it possible to accurately quantify the location and extent of the mechanical contraction delay present in dyssynchrony.

Displacement Encoded Imaging (DENSE)

Displacement Encoding with Stimulated Echos (DENSE) is another MR phase contrast method for the measurement of myocardial motion. DENSE imaging uses the same principles of encoding motion within myocardial spins as MR PVM, but with DENSE, the phase of each pixel is modulated according to its position rather than its velocity[97]. Like MR PVM, DENSE provides motion information for each pixel within the image. The main distinction between DENSE and MR PVM is that DENSE usually generates only a single displacement image (usually for an end-systolic frame relative to an end-diastolic frame) throughout the cardiac cycle[98]. The advantage to this approach is that the displacements encoded by DENSE are larger than those encoded with MR PVM, so contrast is increased and lower gradient strengths are required[97]. Furthermore, the measured displacements can be used to directly compute intra-myocardial strains[89 99]. The clear disadvantage is the low temporal resolution, meaning that much less that data is generated throughout the cardiac cycle.

Methods to Analyze Cardiac Motion

In addition to the direct visualization of the myocardial motion data acquired with MR and echocardiography, several post-processing methods exist to extract additional information from the acquired data. Included in this software are methods to follow individual regions of myocardial tissue throughout the cardiac cycle and methods for the computation of myocardial strain and strain rate.

Tissue Tracking

Accurately describing the motion of the myocardium requires knowledge regarding the motion of individual regions of the myocardium over time. However, this information is difficult to obtain because contraction of the left ventricle during systole is complex, involving shear, twist, and long-axis displacement. The long-axis motion of the left ventricle is especially significant, with estimates of long-axis displacement at the base of the ventricle in the range of 10mm-14mm[49]. Since slice thicknesses of between 5 mm and 10 mm are routinely used in cardiac imaging studies, long axis motion becomes especially problematic when short axis slices of the myocardium are taken; in a short axis slice of the heart, long-axis motion causes the myocardium visualized within the slice thickness to vary throughout the cardiac cycle[100]. Following the trajectory of an individual region of myocardium becomes difficult because a different section of the heart is visualized in each phase of the cardiac cycle.

Motion tracking techniques are necessary to follow the motion of individual regions of myocardial tissue throughout the cardiac cycle. A method for tracking individual particles from MRI phase velocity data was described in 1995 by Pelc et.al[100]. The idea underlying the tracking method is that the location and three-dimensional velocity of a pixel in one frame can be used to compute its location in the next frame. The assumption is made that myocardial motion is periodic, and the restriction is imposed that any given region will always returns to its end-diastolic starting point. This allows motion to be estimated by either a forward or a backwards integration algorithm, with the forward integration determining where the pixel is going, and the backwards integration determining where the pixel came from. The error in the forward integrated trajectory is greatest at the end of the cardiac cycle, while the error in the backwards-integrated trajectory is greatest at the beginning of the cardiac cycle. Since myocardial motion is periodic, the two trajectories can be combined via a weighting term that is dependent on the cardiac phase to produce a more accurate trajectory[100]. This simple motion tracking technique has been verified to be accurate with errors of less than 1mm in both a phantom model and in vivo[100].

It is important to note that this tissue tracking algorithm can only be implemented using MR PVM velocity data. MR PVM is the only myocardial motion imaging technique that provides velocity information with high enough spatial and temporal resolution to track individual regions of the myocardium and examine intra-myocardial motion. Velocity data sets from TDI and tagged MR are incomplete (TDI usually only contains information for long-axis motion, while tagged MR only provides information about the two in-plane directions). Velocity data extrapolated from MR tagging algorithms also has extremely poor spatial resolution, usually only providing information for one or two points within the thickness of the LV wall, and, when processed using the HARP algorithm, provides strain, not velocity information. Although DENSE data is of sufficient spatial resolution, the temporal resolution is often poor or the signal is low.

Strain and Strain Rate

Strain (ε) and strain rate (SR) are measures of myocardial contractility. Strain is defined as the deformation of an object normalized to its original shape, and SR is the speed at which that deformation occurs[101]. Since strain and SR are not affected by contractile function in adjacent myocardial regions, they are more direct measures of regional myocardial function than tissue velocities[102]. Both strain and SR are able to non-invasively determining regional contractility and differentiate between actively contracting and passively tethered myocardium. SR imaging by ultrasound has demonstrated the ability to differentiate between ischemic and non-ischemic myocardium[103,104], and when used in combination with dobutamine stress testing, has been able to differentiate between stunned and ischemic myocardium[105-107].

Peak radial strain values are approximately twice the magnitude of peak longitudinal strain values[108], and peak radial SR are significantly larger than peak longitudinal SR values[109], arguably making radial motion the largest contributor to ejection fraction. It has been demonstrated that during ischemia, radial motion abnormalities are detectable before longitudinal or circumferential motion abnormalities[106]. Furthermore, it has been shown that radial dyssynchrony (defined as the standard deviation of time-to-peak in six basal segments) is associated with depressed LV function and that radial dyssynchrony greater than 130 msec is predicative to acute response to CRT[110,111].

Although the applications of strain and SR imaging have been promising, myocardial strain and SR, and *radial* strain and SR in particular, continue to be difficult quantities to measure in-vivo. SR is a particularly elusive quantity, as two derivatives (one spatial and one temporal) are required to extract this value from displacement data such as ultrasound speckle tracking or MR tagging[112]. Since each derivative introduces additional noise into the signal, SR curves have often been difficult to interpret.

Measuring SR from Tissue Doppler velocity data has been proposed as a way of overcoming this limitation. By this method, SR is computed as the spatial gradient of velocity, and strain in computed as the temporal integral of the SR values[101]. This method has been successfully applied to measure longitudinal strain and SR within the myocardium[101,108,113]. However, ultrasound studies are restricted by the angle of the ultrasound beam to measuring radial strain only within the posterior wall in mid and basal slices[101,103]. MR PVM tissue velocity measurements offer the ability to overcome this limitation. Since MR PVM is able to acquire three-dimensional velocity information throughout the entire myocardium, it is possible to compute radial SR for every region within the myocardium. Since SR is computed directly from velocity measurements, and SR is integrated to compute strain, strain and SR values computed using this method have some potential signal-to-noise advantages. Furthermore, the high spatial resolution of the underlying MR PVM velocity data offers the possibility of differentiating between endocardial and epicardial strain and SR values.

Summary of Background

Cardiac Resynchronization Therapy (CRT) has been proven as an effective treatment option for heart failure patients with dyssynchrony who are at optimal medical management. Patient selection criteria for CRT have been based primarily on the presence of a prolonged QRS interval on a surface electrocardiogram. Although most patients selected for CRT by this method almost immediately experience clinical improvement after device implantation, up to 30% of patients implanted with a CRT device do not see any benefits. Many unsuccessful attempts have been made to identify differences in clinical parameters between these responders and nonresponders.

Recently, Tissue Doppler imaging has suggested that one of the best predictors of response to CRT is the level of underlying mechanical dyssynchrony in the myocardial wall prior to CRT. As a result, there has been growing interest in direct imaging of the myocardial wall. Because myocardial contraction is a complex, three-dimensional movement involving longitudinal and radial shortening, torsion and shear, providing an accurate picture of myocardial wall motion can be challenging. Echocardiography initially emerged as the modality of choice, but the long list of limitations (limited echocardiographic windows, one direction of motion, poor reproducibility) has fostered interest in exploring the use of MR for myocardial wall imaging. Even though MR presents some unique drawbacks (expensive equipment, longer imaging times), it is able to overcome many of the limitations of TDI. In particular, Phase Velocity Mapping (MR PVM) can provide a complete, three-directional description of motion throughout the entire myocardial wall at high spatial and temporal resolution and may present an advantage over TDI in identifying and quantifying mechanical dyssynchrony in the myocardial wall.

CHAPTER 3

AIM1: DEVELOPMENT OF IMAGING PROTOCOL AND ANALYSIS SOFTWARE FOR MR PVM TISSUE VELOCITY IMAGES

The goal of this specific aim was to develop the MR PVM scan protocol for the acquisition of myocardial tissue velocities and the image processing software for the acquired velocity data. The developed protocols were applied to all collected datasets throughout the remainder of the project.

MR PVM Tissue Velocity Scan Protocol

All MR imaging was performed on a Philips Medical Systems Intera CV scanner using a 5-element phased array cardiac coil (Phillips Medical Systems, Best NL). Design of the MR PVM protocol began with a segmented, ECG-triggered, gradient-echo phase contrast sequence in which all three directions of velocity were acquired. Raw data was saved, and a separate delayed reconstruction was needed to extract velocity information in each direction. (This limit was imposed by the image reconstruction algorithm on the scanner, not the pulse sequence itself). Several other parameters, including navigator placement, interleaving of velocity directions, reconstruction filters, rest slabs, velocity encoding value, and Sensitivity Encoding (SENSE) were considered in determining the final velocity acquisition protocol.

Navigator Placement

Navigator-echo gating enables the acquisition of velocity data within the myocardium without the need for breath-holding[114-116]. A navigator-echo placed on the diaphragm at the lung-liver interface monitors the position of the diaphragm. This provides real-time monitoring of respiratory motion and can be used to gate image acquisition. The combination of navigator-echo gating with three-directional phase velocity imaging allows myocardial tissue velocity data to be acquired in patient populations with a limited breath-hold capability and ensures that measurements from all three velocity directions are correctly registered for post-processing.

The execution of the navigator is shown in Figure 3.1. The navigator is the green rectangle placed at the lung-liver interface on the MR image at the left. The red dots in the figure on the right represent the position of the lung-liver interface over time. An acceptance or “gating window” is chosen, and image data is only retained when the diaphragm is within this acceptable window. The green dots in Figure 3.1 each represent a point in time in which the acquired velocity data was accepted.

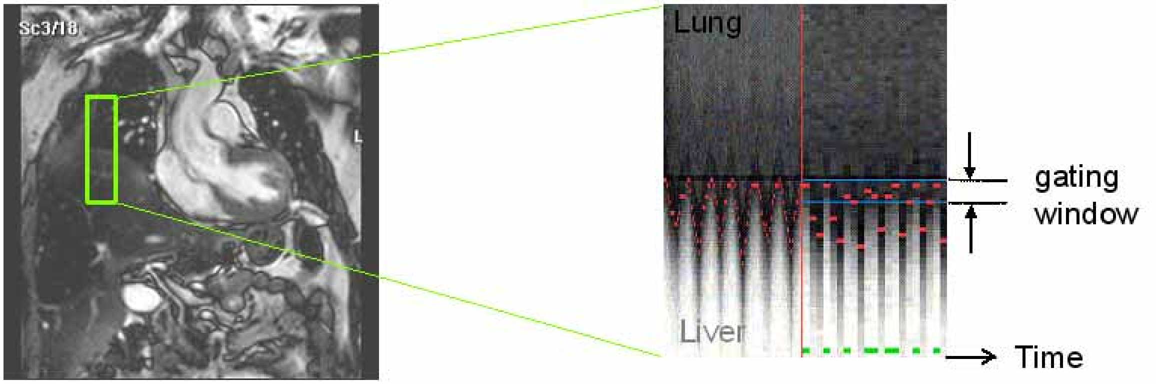

__Figure 3.1__: Navigator Echo Gating

The navigator pulse takes approximately 75msec to execute and can be placed immediately after detection of the R-wave (leading navigator) or during end diastole before the detection of the subsequent R-wave (trailing navigator). The purpose of this study was to determine whether a leading or a trailing navigator would be more suited for use with the MR PVM sequence for the measurement of myocardial tissue velocities.

The study population was a group of five normal volunteers. In all five volunteers, MR PVM velocity data was acquired with both a leading and a trailing navigator within the same scan session. For each acquired dataset, curves of velocity over time in 8x8mm regions of interest (ROIs) were generated in the septal, lateral, anterior, and inferior walls.

Typical longitudinal velocity curves acquired with leading and trailing navigators are shown in Figure 3.2. Curves were generated from the lateral wall ROI in the same volunteer. Note that the trailing navigator curve begins at zero velocity (i.e. before systolic contraction has begun), while velocity data for the leading navigator curve begins after the heart has begun to contract. Also, note that the initial data point in the leading navigator curve has a large velocity offset (depicted by the red arrow in Figure 3.2). Also of importance is that velocity curves from both leading and trailing navigators are able to fully capture diastolic relaxation, and that both curves return to zero at the end of the cardiac cycle.

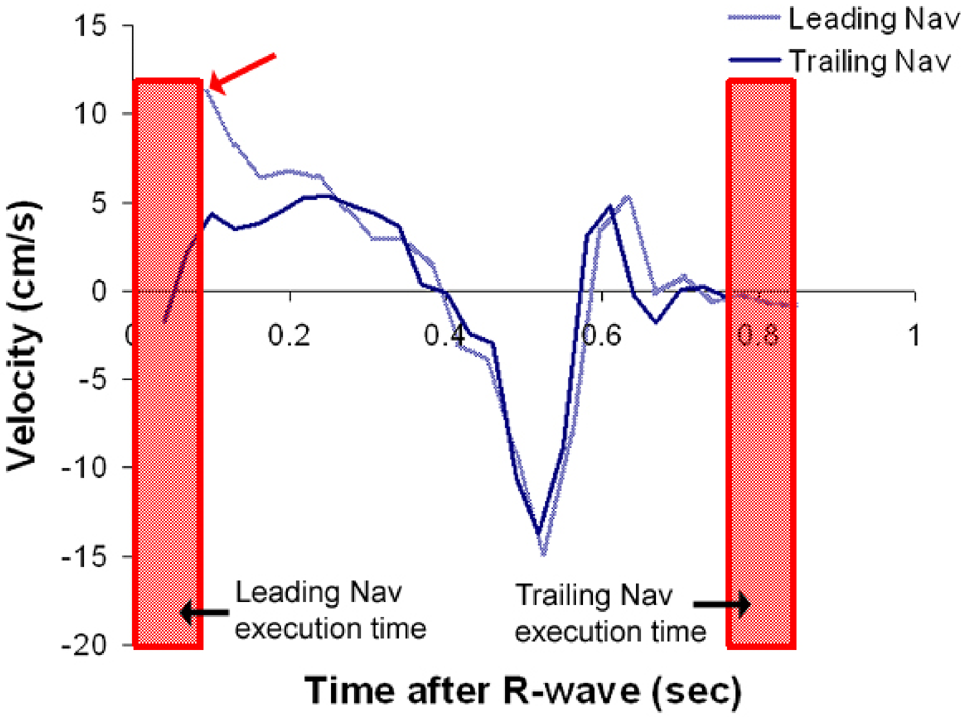

Figure 3.2: *Velocity curves from leading and trailing navigators.*

Based on the above findings and the fact that end-diastole is a relatively quiet period during which the heart undergoes very little motion, a trailing navigator was chosen for the acquisition of MR PVM velocity data. The trailing navigator enabled the acquisition of velocity information throughout the entire active part of the cardiac cycle, including the first 100 msec of early systole that would have been missed with a leading navigator, but still was able to sufficiently capture all of diastolic relaxation.

Velocity Interleaving

When multiple directions of velocity are acquired, Release 11 of the Philips Intera software allows the multiple directions of velocity to be interleaved either by TR or by heartbeat during acquisition. Figure 3.3 illustrates the differences in the two techniques for a segmented, ECG-gated sequence that employs rest slabs and a trailing navigator. During each cardiac phase (P), a rest pulse is executed (rest), and 3 lines of k-space are acquired (k_1, k_2, k_3). Interleaving velocities by heartbeat means that information for different velocity directions (Vx, Vy, Vz, and reference) is acquired in separate heartbeats. This allows velocity data to be acquired at high temporal resolution, but introduces the possibility of errors, as the reference and velocity directions are acquired in different heartbeats. Interleaving velocities by TR means that information for all encoded velocity directions is acquired in each heartbeat. Since the reference and velocity data are acquired in close succession, the probability of introducing errors into the velocity data is reduced. However, less data is able to be acquired and the temporal resolution of the acquired velocity data is reduced.

For the MR PVM velocity acquisition sequence where encoding is performed for n velocity directions, the effective frame-to-frame temporal resolution for velocities interleaved by heartbeat is the sequence TR; that temporal resolution is reduced to (n+1)*TR when velocities are interleaved by TR. So if it were possible to acquire velocity at 12 cardiac phases with velocities interleaved by heartbeat, it would only be possible to acquire 3 cardiac phases with velocities interleaved by TR. Also important to note is that changing the velocity interleaving from heartbeat to TR decreases the imaging time four-fold (because only ¼ as much data is acquired).

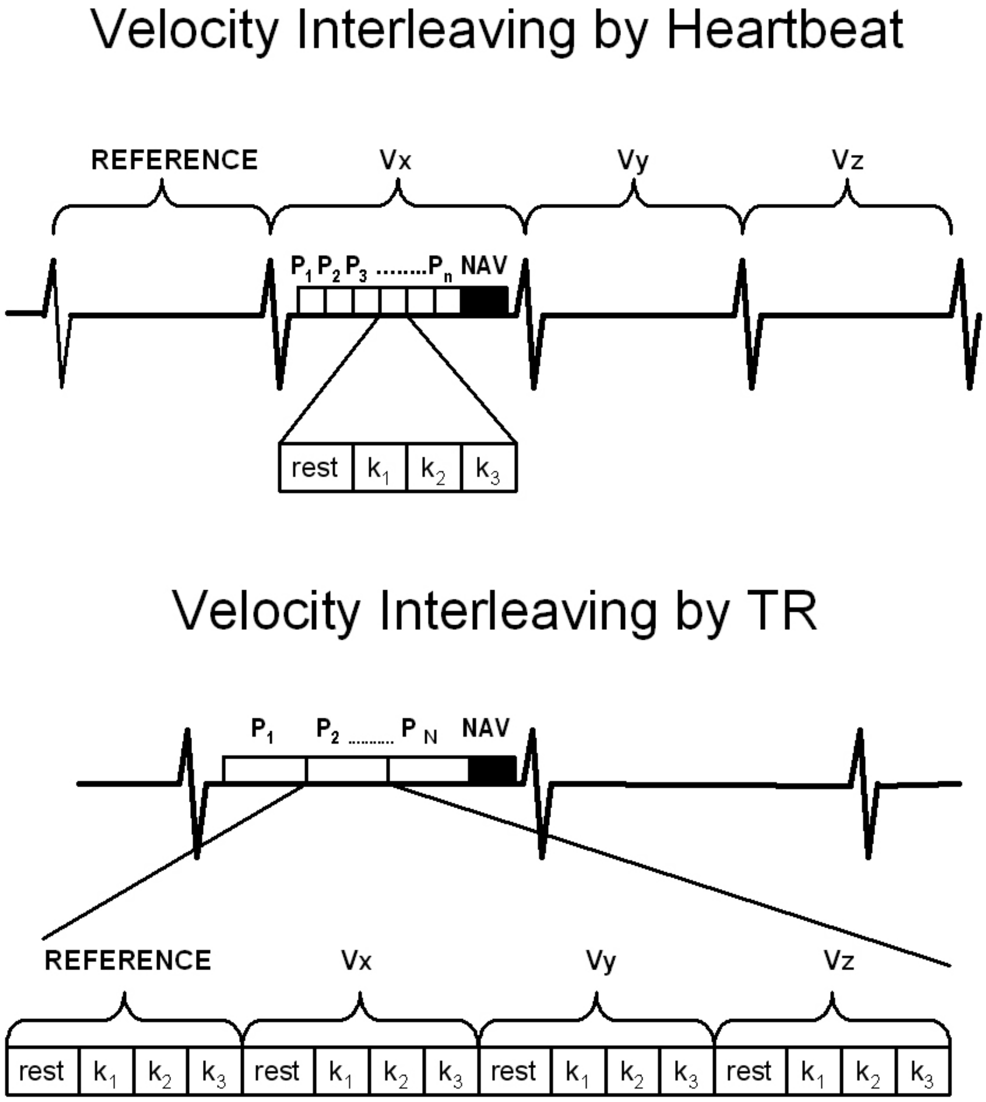

Figure 3.3*: Different modes of velocity interleaving*

Since the objective of this project was to investigate myocardial motion in detail, high temporal resolution was extremely important. Therefore, in the final protocol, velocity directions were interleaved by heartbeat. Although this significantly increased the time necessary for velocity acquisition, the acquired velocity data contained the necessary detailed myocardial motion information.

Velocity Encoding Value (Venc)

The velocity encoding value, or Venc, is the largest phase shift that the sequence can measure without aliasing. Accurately imaging the lower velocities of myocardial tissue requires selecting a Venc value that is significantly lower than is used for blood flow imaging. However, imaging with lower Venc values requires higher gradients, which require longer echo times and higher bandwidths. Therefore, selecting the appropriate Venc value is a compromise between sensitivity in the detection of desired velocities (which requires the smallest Venc possible) and imaging time and readout bandwidth, which increase with decreased Venc.

The purpose of this study was to determine the optimal Venc value for imaging myocardial motion. Venc values of 20, 30, and 40cm/s were considered.

Because of the increased bandwidth and longer echo times associated with smaller Venc values, the lowest Venc value (20cm/s) often led to artifacts within the myocardium. These image artifacts were seen primarily within the lateral and inferior walls, and may have been caused by phase susceptibility of deoxygenated blood in the great cardiac vein or the heart-lung interface[117,118]. Artifacts are denoted in Figure 3.4 by an arrow. Increasing the Venc value from 20cm/s to 40cm/s eliminated the artifacts. (All other scan parameters were held constant for the two acquisitions shown).

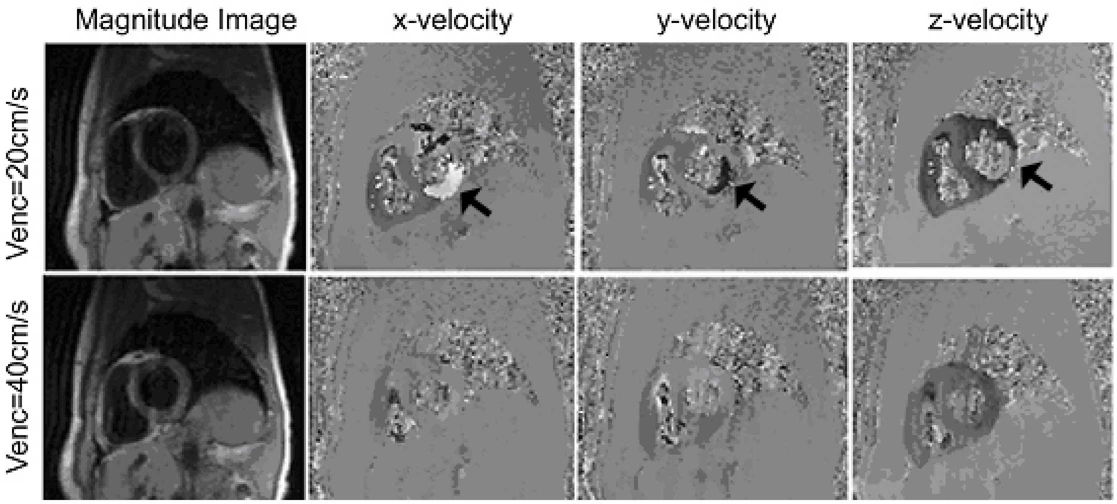

Figure 3.4*: Effects of Venc on MR PVM images of myocardial tissue.*

In the final protocol, a Venc value of 30cm/s was selected as a compromise. This shorter echo time eliminated the artifacts within the myocardium, but was still sufficient to accurately measure lower myocardial velocities.

Reconstruction Filters

By default, Intera Release 11 software automatically applies several post-processing filters to phase contrast images. These filters are intended to ease interpretation of velocity images. Of particular interest to myocardial velocity imaging are the Noise Clip Filters and Local Phase Correction (LPC) filters.

The Noise Clip Filters are a multiplication factor for the calculated noise threshold. During image reconstruction, a background noise threshold is calculated for the entire magnitude image, and this value is multiplied by the Noise Clip Filters. During execution of this filter, image pixels below the noise threshold in the phase image are forced to zero. The LPC filters provide background phase correction for phase contrast (PC) and quantitative flow data (QF). The QF LPC and PC LPC values specify the size of the local phase correction window for the two image dimensions.

The purpose of this study was to determine the effect of the Noise Clip Filters and the phase contrast (PC) and quantitative flow (QF) local phase correction (LPC) filters on the imaging of myocardial velocity with the MR PVM sequence.

It was discovered that the automatic execution of the Noise Clip Filters can obscure myocardial tissue velocity measurements by suppressing low velocity values from within the heartwall. Since increasing the value of the Noise Clip Filter increases the noise threshold, setting the value of the Noise Clip threshold as close to zero as possible minimizes the effects of this filter. Since the filter cannot be set to zero completely (this is not an option with the current software), values of 0.01,0.01,0.01 were selected in the final protocol. Figure 3.5 shows the effects of the Noise Clip Filters on myocardial velocity data. When the filter is left on, velocity in the lungs and outside of the chest wall is forced to zero and appears as a uniform gray color. However, velocity values in some regions of the myocardium (shown with an arrow) are also forced to zero. When the filter is turned off, the lungs and the area outside of the chest wall appear as salt and pepper noise, but the signal from the entire myocardium is preserved. As is clearly visible from Figure 3.5, the Noise Clip Filters need to be turned off in order to accurately measure myocardial tissue velocities with the MR PVM scan.

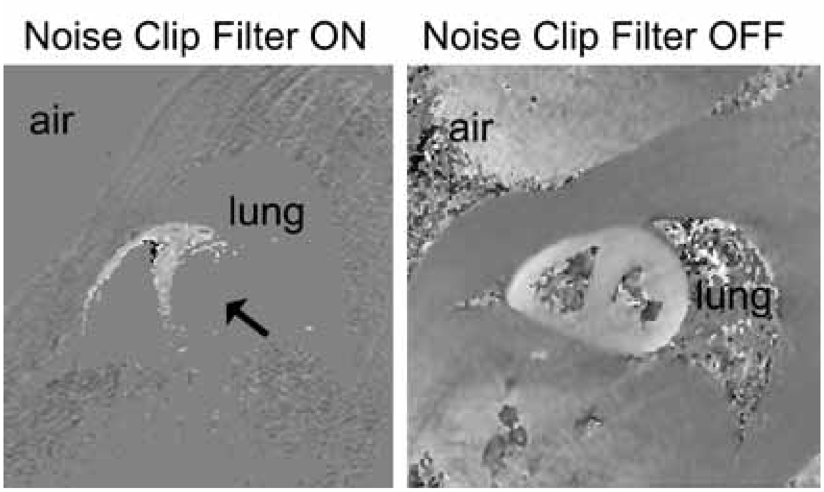

Figure 3.5*: Effect of the Noise Clip Filters on myocardial velocity data.*

The Quantitative Flow Local Phase Correction (QF LPC) and the Phase Contrast Local Phase Correction (PC LPC) filters produced inconsistent results when applied to myocardial velocity datasets. In some datasets the LPC filters helped to reduce background phase velocity offsets, but in other datasets the same filters offset velocity curves within the myocardium so that they did not begin and end at zero velocity. Because a detailed description of how these filters were executed in the Intera Release 11 software could not be obtained, and any patterns could not be found describing when they were helpful and when they were not, the LPC filters were turned off (values of 0,0) in the final velocity acquisition protocol. As a substitute, background phase offset correction was performed manually using an in-house developed Matlab algorithm (the algorithm is described in detail later in this chapter).

Presaturation Slabs

Presaturation slabs can be placed on either side of the imaging slice to null signal from inflowing blood[119]. Presaturation slabs apply a 90 degree pulse to an area adjacent to the imaging slice. This pulse nulls the MR signal from blood as it enters the imaging slice, thus creating a signal void within the myocardial bloodpool and increasing contrast between blood and myocardial tissue. However, the execution of presaturations slabs decreases the frame-to-frame temporal resolution of the acquired velocity data and increases the total imaging time.

The purpose of this study was to test whether rest slabs were necessary in the MR PVM sequence or if adequate image quality could be obtained without them.

When rest slabs were present, there was no signal from the blood pool, and the boundaries of the myocardium were clearly delineated on the velocity images. Without the rest slabs, the myocardial bloodpool retained its signal and appeared bright on the magnitude image. This made it difficult to distinguish between blood and myocardial tissue. Furthermore, the large phase shift from the inflowing blood caused significant artifacts in the velocity images, both during systole and diastole.

Figure 3.6 illustrates the effect of rest slabs on myocardial velocity images. All images are from the same patient and were acquired within the same imaging session. Aside from the presence of rest slabs, all imaging parameters remained constant for the two acquisitions. When rest slabs were used, the LV bloodpool has no signal and appears a dark on the magnitude image and as noise in the velocity images. Without the rest slabs, the bloodpool retains its signal and appears light in the magnitude image, making it more difficult to distinguish between blood and myocardial tissue. Furthermore, the large phase shift from the blood causes signal loss and artifact in the myocardium in the phase image (denoted with arrows on the phase images).

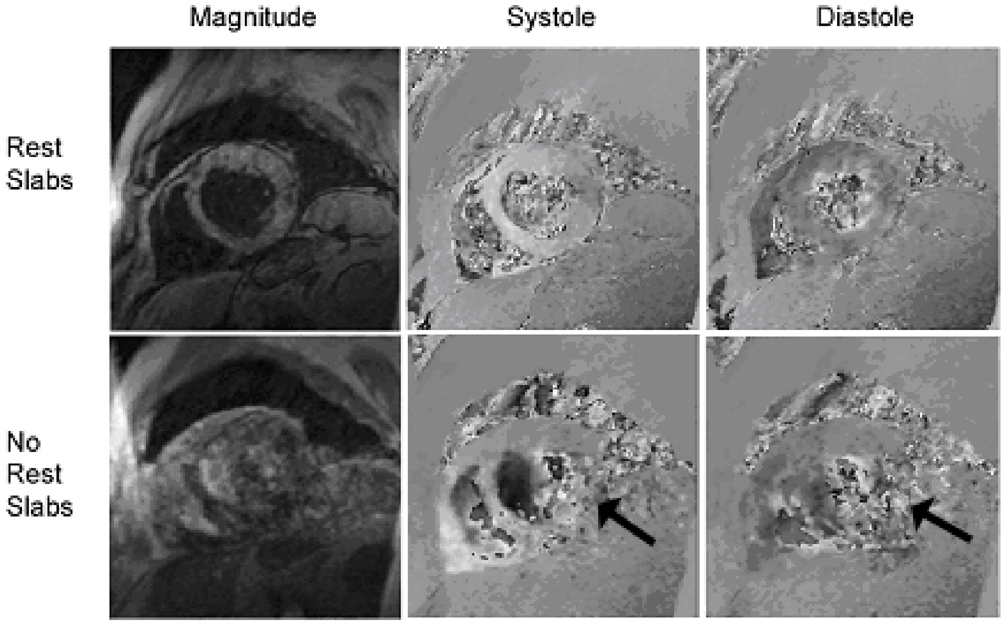

Figure 3.6: Effect of rest slabs on myocardial velocity data.

The clear conclusion was that rest slabs are necessary when imaging myocardial tissue velocities. In the final protocol, we elected to employ two parallel rest slabs, one on each side of the imaging slice.

Sensitivity Encoding (SENSE)

Sensitivity Encoding, or SENSE, is a parallel imaging technique that can be employed with phase velocity mapping to reduce total scan time[120]. The acceleration in imaging time is accomplished by under sampling k-space and using sensitivity information from multiple imaging coils during image acquisition. However, because less data is acquired, images acquired using SENSE have a lower signal-to-noise ratio and suffer some other problems of aliasing during "unfolding" of the image during reconstruction.

The purpose of this study was to test the feasibility of using SENSE with the MR PVM sequence.

A small study with five normal volunteers was performed. Volunteers underwent two myocardial velocity acquisitions with the MR PVM sequence in a single scan session, one without SENSE, and the other with a SENSE factor of two. All other imaging parameters were held constant for the two scans. After acquisition of images, longitudinal velocity was measured in four 8x8mm regions of interest within the myocardium (in the septal, lateral, anterior, and inferior walls). A Bland-Altman analysis was conducted to quantitatively compare myocardial velocities acquired with SENSE and without SENSE.

Curves of velocity collected in the lateral ROI of a normal volunteer with and without SENSE are shown in Figure 3.7. Note that the curves collected with and without SENSE are nearly identical.

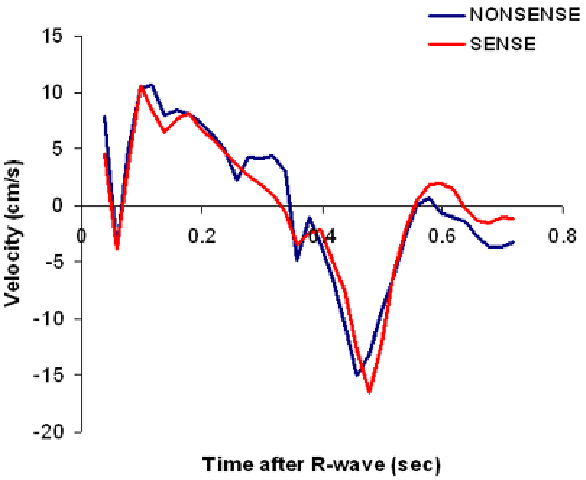

***Figure 3.7**: Velocity curves with and without SENSE.*

The Bland-Altman analysis determined that the mean difference between velocity curves acquired with SENSE and without SENSE was -0.01 +/- 3.5 cm/s. The Bland-Altman plot of the data from all five volunteers is shown in Figure 3.8. Although the mean difference between SENSE and non-SENSE was close to zero (mean difference=-0.01 cm/s), the standard deviation was not insignificant (stdev=3.5cm/s).

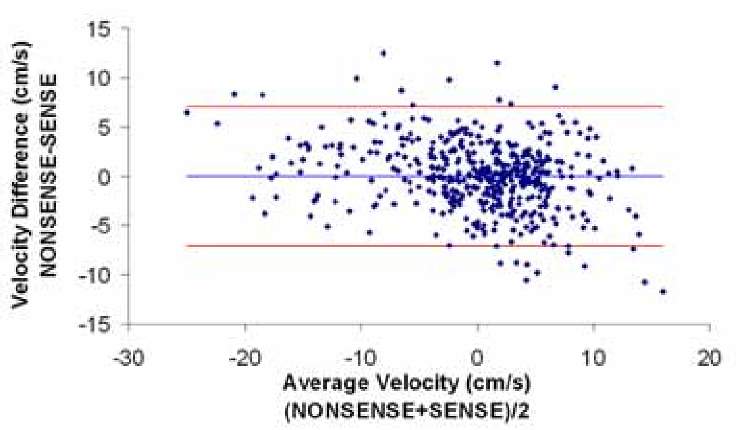

***Figure 3.8**: Bland-Altman of velocity acquired with and without SENSE.*

As expected, the introduction of SENSE decreased image quality and made the images more susceptible to foldover artifacts. Foldover artifacts were often seen in the center of the image, right at the location of the myocardium, thus making interpretation of myocardial velocity impossible. Figure 3.9 shows an example of such a foldover artifact. The area of the chest wall denoted by the arrow in the nonsense image appears within the center of the myocardium when SENSE is employed, making interpretation of myocardial velocities in the SENSE image extremely difficult.

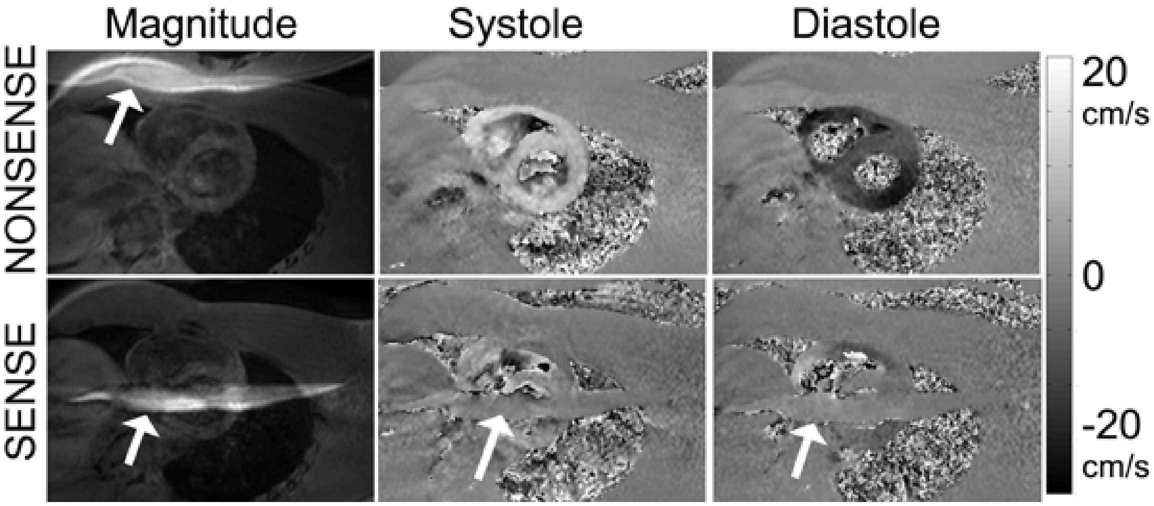

***Figure 3.9**: MR PVM images acquired with and without SENSE.*

Due to the frequent presence of foldover artifacts within the myocardium, SENSE was not employed in the final imaging protocol. However, it is entirely possible that SENSE may have been successfully used if care was taken to avoid any foldover artifacts.

Final Velocity Imaging Protocol

The final velocity imaging protocol was based on results from all the above experiments. Three-directional myocardial velocity was acquired using an ECG-gated, segmented (3 lines of k-space per shot), gradient echo phase contrast sequence[121] In an effort to obtain velocity information for multiple areas of the left ventricle, velocity was acquired at three short axis slices (slice thickness = 10mm, slice gap=10mm), planned during systole so that myocardial tissue remained in the most basal slice throughout the entire cardiac cycle. Velocity encoding was performed in a Hadamard fashion using four-point velocity vector extraction with encoding for different directions interleaved by heartbeat[122].

A schematic of the pulse sequence is shown in Figure 3.10. For each velocity direction (Vx, Vy, Vz) and the reference scan, myocardial velocity was acquired at multiple phases (P_1,P_2,P_3….P_n) throughout the cardiac cycle. During each cardiac phase, a rest pulse was executed (rest), and three lines of k-space were acquired (k_1,k_2,k_3). The X,Y,Z, and RF channels demonstrate gradient and RF activity during the acquisition of each k-space line.

Acquisition parameters were as follows: in-plane resolution=1.4 mm (scan matrix = 144, reconstructed to 256), slice thickness=10mm, velocity encoding value=30cm/sec, flip angle=15 degrees, FOV=370mm, TR=shortest, and TE=shortest. SENSE was not employed. Parallel presaturation slabs (each 30mm thick, placed 10mm away from the imaging slice) were used to null signal from inflowing blood[123,124]. A trailing navigator with an acceptance window of 6mm was placed on the diaphragm at the lung-liver interface to monitor respiratory motion. The navigator pulse was played out during end-diastole and took approximately 74 msec to execute. LPC and QPC filters were turned off (values set to 0,0) prior to acquisition. Noise clip filters were also turned off (value set to 0.01,0.01,0.01). The first velocity frame was acquired 15 msec after detection of the R-wave, and the frame-to-frame temporal resolution was between 26 and 35msec, depending on the orientation of the imaging slice. Total acquisition time for the velocity encoding scan at three myocardial slices was four and a half minutes with a navigator efficiency of 100%; actual scan time depended on navigator efficiency, which ranged between 30 and 80%.

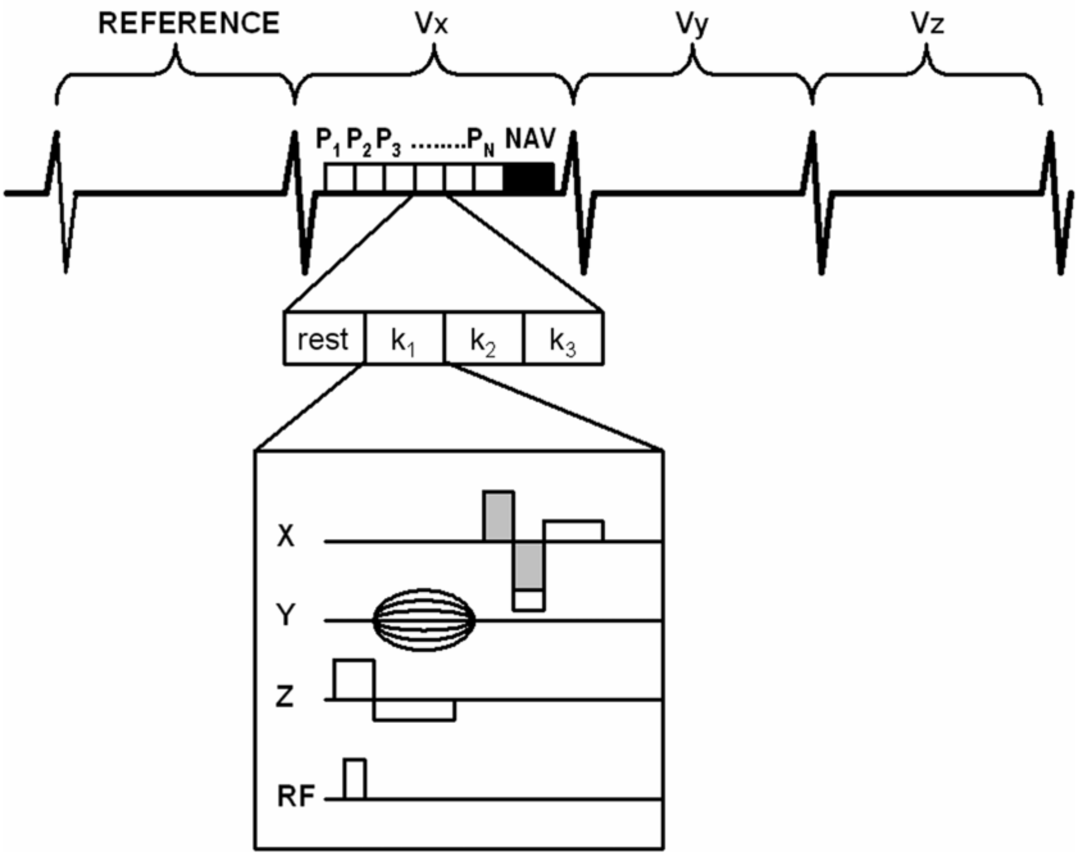

***Figure 3.10**: Schematic of the final MR PVM sequence.*

An example image showing the acquired three-directional velocity maps at a single cardiac phase is shown in Figure 3.11. Figure 3.11A shows the magnitude image, Figure 3.11B shows the phase velocity map of left-to-right motion, Figure 3.11C shows the phase velocity map of anterior-to-posterior motion, and Figure 3.11D shows the phase velocity map of apex-to-base motion. Note that all images are correctly registered for post-processing. Movement in the positive velocity direction appears light and movement in the negative velocity direction appears dark, while static objects are gray. The air in the lungs and outside the chest walls appears as noise.

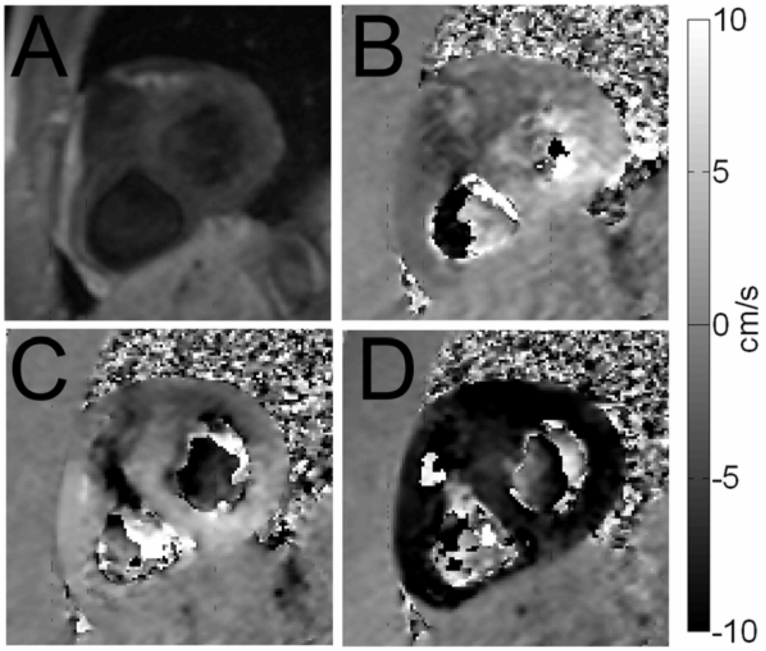

Figure 3.11*: Example MR PVM myocardial velocity image.*

Image Analysis Software

After acquisition, images were exported from the MRI scanner in DICOM format and were imported into Matlab (Mathworks, Natick, MA) for analysis. All image processing was performed in Matlab with custom-written software. Several image processing methods were universal to all acquired datasets, and those methods are outlined below.

Background Phase Correction

Static structures such as the chest wall should have zero velocity in phase contrast images. However, additional sources of phase errors such as gradient overshoots and Eddy currents may introduce phase offsets into the velocity image[125-129]. These offsets will lead to incorrect velocity measurements and errors when the tracking algorithm is applied, and therefore need to be removed before velocity in the image is quantified. Furthermore, since the local phase correction filters on the scanner were turned off as part of the myocardial tissue velocity acquisition protocol, we expected myocardial tissue velocity images to have a background phase offset.

Background phase error was removed using a least-squares fitted plane method that has been described previously[130]. Pixels in which the variance of velocity over time was below a determined cutoff value were identified as static. The static pixel cutoff value was individually tailored to each dataset and each velocity direction. Figure 3.12 shows an example of the areas defined as static tissue based on the variance of pixels within the velocity image in a normal volunteer. Static pixels have been labeled in red and are shown superimposed onto the magnitude image reconstruction.

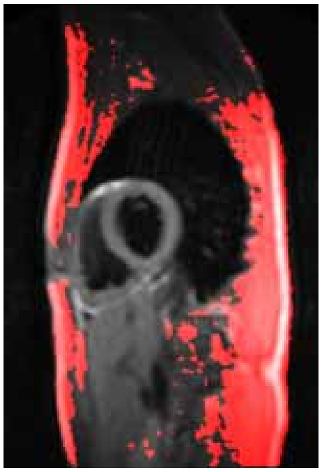

***Figure 3.12**: Tissue defined as static for background phase correction.*

A plane surface was fitted to the velocity in the static pixels using a least-squares fit. This plane, which contained an estimate of velocity errors across the image, was computed for each frame of the velocity data. An average of the velocity offset plane was computed throughout the cardiac cycle, and this average offset value was subtracted from the original velocity data. Correction for each direction in the three-dimensional data set was done independently.

Validation

A simple static imaging phantom that had both a “chest wall” and a “heart” was constructed. Since the phantom was static, any velocity recorded during the MR PVM scan was due to noise or unwanted phase offsets. Velocities of up to 3 cm/s were observed within the static "heart" of the phantom.

To test the ability of the least squares fitted plane algorithm to accurately remove background phase offsets, only the outer chest wall region was used in computing the offset plane. This was done to mimic the scenario from the in vivo scan where only the chest wall is static and can be used for offset computation. The computed plane was then subtracted from the entire image, and velocity values within the static "heart" were measured. The background phase correction was conducted independently for each velocity direction.

The least squares fitted plane algorithm was compared to a simple offset correction algorithm in which a constant offset, determined by finding the average velocity in three static ROIs within the image, was subtracted from the image.

Table 3.1*: Velocity in the static heart phantom before and after background phase correction.*

	Velocity in static "heart" region (cm/s)		
	Without offset correction	**Correction with fitted plane**	**Correction with constant offset**
x-velocity	-3.00+/- 0.05	0.69+/-0.07	-1.49+/-0.06
y-velocity	-0.28+/-0.04	0.05+/-0.04	0.50+/-0.07
z-velocity	-1.99+/-0.04	0.47+/-0.03	1.03+/-0.11

Velocity within the heart region decreased significantly after the phase correction algorithm was applied, and the phase correction algorithm using a fitted plane was the superior background phase offset correction algorithm. Velocity values within the heart region of the phantom are given in Table 3.1. Figure 3.13 shows an example image from the phantom before and after the least-squares background phase correction algorithm was applied. Note that after the correction is applied, velocities within the static heart phantom are closer to zero and more uniform.

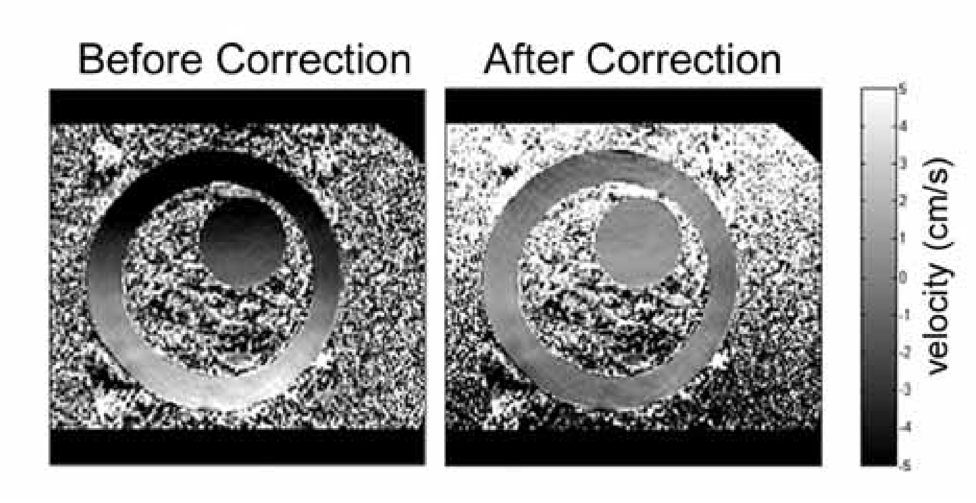

Figure 3.13*: Static phantom before and after background phase correction.*

Based on the previous experiments, it was determined that the least squares fitted plane background phase correction algorithm was an acceptable alternative to the Local Phase Correction filters, and the algorithm was applied to all velocity datasets acquired with the MR PVM scan protocol.

Tissue Tracking Algorithm

A tissue tracking algorithm based on a method for tracking individual particles from MRI phase velocity data described by Pelc et al in 1995 was implemented in Matlab[100]. The idea underlying the method is that the location and three-dimensional velocity of a pixel in one cardiac frame can be used to compute the location of that pixel in the next cardiac frame. Furthermore, if the assumption is made that myocardial motion is periodic, and the restriction is imposed that any given region will always returns to its end-diastolic starting point, motion can be estimated by either a forward or a backwards integration algorithm. The error in the trajectory computed using forward integration is greatest at the end of the cardiac cycle, while the error in the trajectory computed using backward integration is greatest at the beginning of the cardiac cycle. Since myocardial motion is periodic, the two trajectories can be combined via a weighting term that is dependent on cardiac phase to produce a more accurate trajectory[100]. The computed trajectory will give the location of a specific segment of myocardium throughout the cardiac cycle, and that information can be used to determine the velocity of the region over time. The accuracy of the combined forward-backward tracking algorithm has previously been tested and proven to be sufficient for following the motion of myocardial regions throughout the cardiac cycle[100,131-134].

A schematic of the tissue tracking approach is shown in Figure 3.14. In a cardiac cycle with k velocity images taken at time intervals of Δt, the algorithm begins at frame 1. In forward integration, the velocity of a point in the first frame $V(f_1,t_1)$ is used to determine the location of the that point in the next frame, $f_2=f_1+V(f_1,t_1)\Delta t$. In reverse integration, the location of the first point and the velocity in the last frame $V(f_k,t_k)$ is used to determine the location of the point in the frame, $f_k=f_1-V(f_k,t_k)\Delta t$. Because of the periodic nature of myocardial motion, the trajectory of an individual pixel can be obtained either through forward or reverse integration, with the most accurate trajectory being a combination of the two.

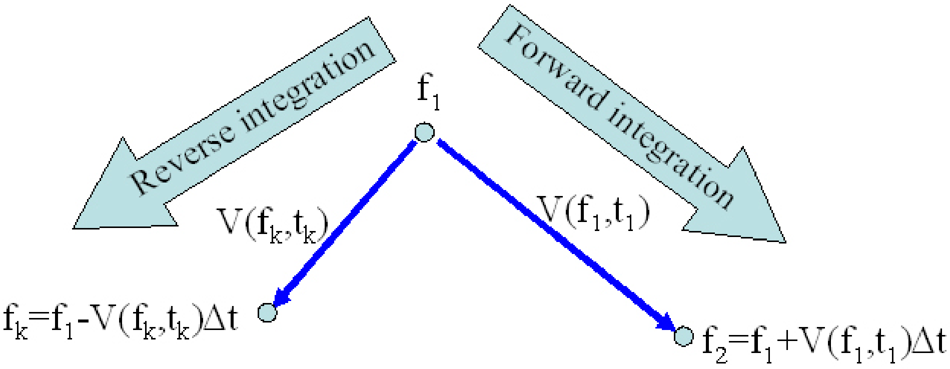

***Figure 3.14** – Schematic of the myocardial tracking algorithm.*

Validation

To test the accuracy of the tissue tracking algorithm in-vivo, the (x,y,z,t) position output of the tracking algorithm was compared to the location of tag intersection points on tagged MRI images. The comparison was done using short axis images, in which tagged and velocity data were acquired at the same myocardial location. Displacement on the tagged images was considered the gold standard.

The tracking algorithm outputs the three-dimensional (x,y,z) location of each pixel within the myocardium at each time point where MR PVM data was acquired; the tagged MRI sequence shows the deformation of tag lines within the myocardium at each time point where the tagged images are acquired. Because the frame-to-frame acquisition intervals were different for the MR PVM and tagged images (and the tagged images were considered the gold standard), positional data from the tracking algorithm was interpolated to match the time points of the tagged images. The trajectories computed from the MR PVM data were then superimposed onto the tagged images.

To quantify agreement between the tagged and tracked images, the distance between the intersection of the true tagged lines and the trajectories computed by MR PVM was measured. In each cardiac phase, this difference was computed for all tag-intersection points within the myocardium. An average value throughout the entire myocardium was computed for each cardiac phase.

Good agreement was observed between the computed trajectories (shown in green and yellow in Figure 3.15), and the tagged MRI images. Note that the agreement was present during late diastole and persisted throughout end-systole, where maximum myocardial deformation is observed. .

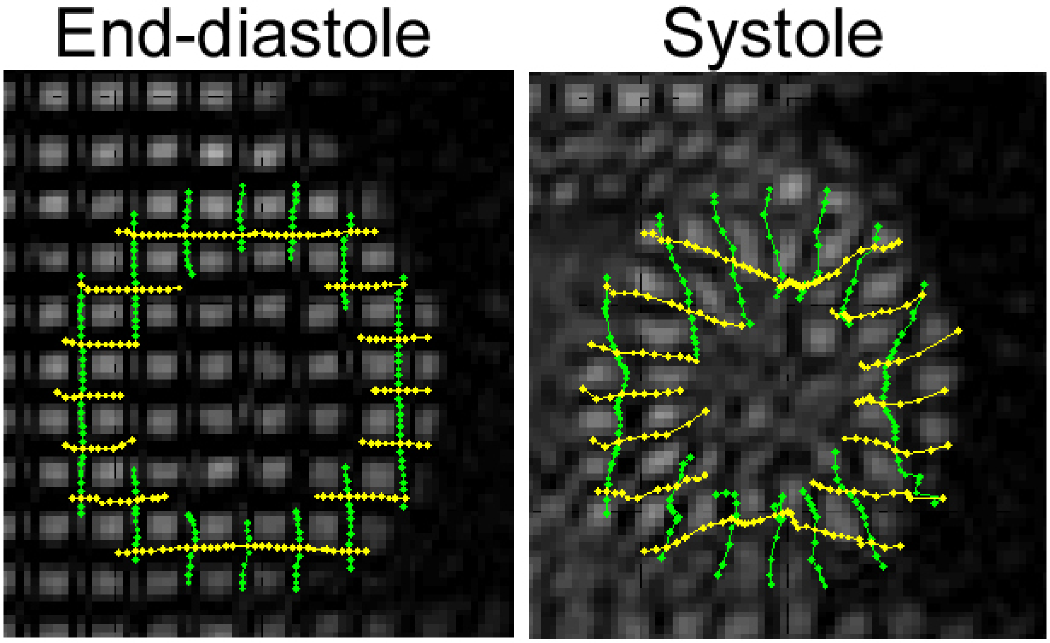

Figure 3.15*: Computed trajectories superimposed onto tagged MRI images.*

As expected, error in the combined forward-backward computed trajectory was greatest in the center of the cardiac cycle. Nowhere throughout the entire cardiac cycle did the error exceed four pixels (in-plane pixel size was 1.4mm). A plot of error in the computed trajectories (in # of pixels) throughout the cardiac cycle is shown in Figure 3.16. Note the shape of the curve, which illustrates that the error was greatest in the middle of the cardiac cycle.

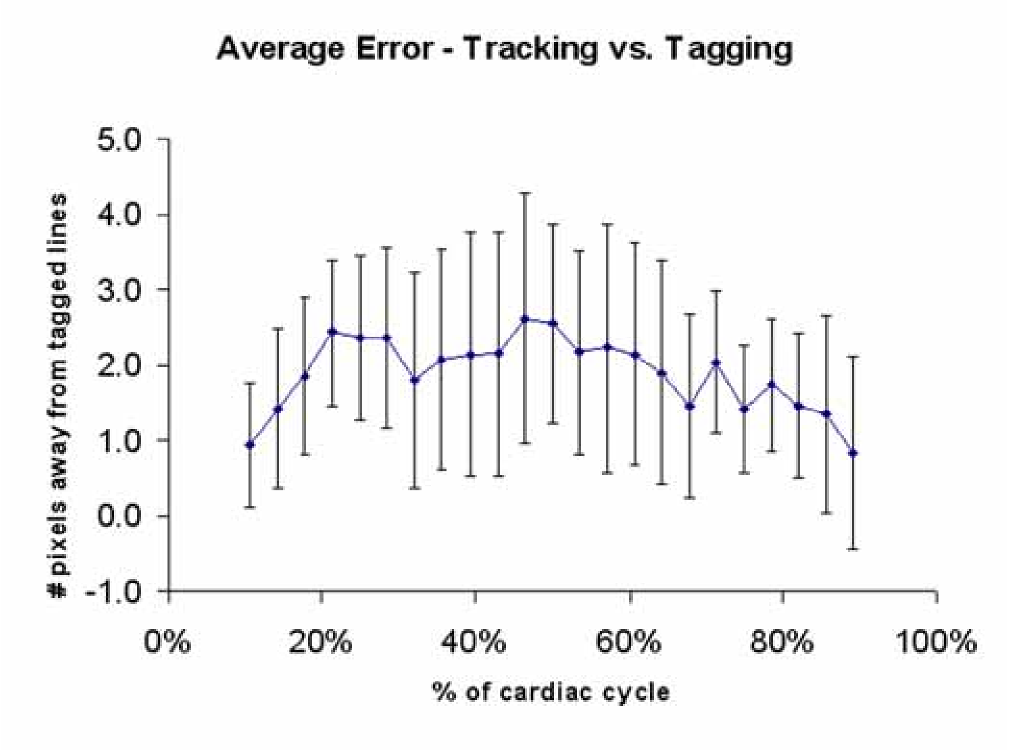

Figure 3.16*: Error between the computed trajectory and myocardial tags.*

It is important to note that tagged MRI images only give information about in-plane motion, while the tracking algorithm—which is computed from three-direction MR PVM data—computes the location of each pixel in three dimensions. Therefore, the error values computed above are only based on in-plane motion and the computed MR PVM trajectory shown in Figure 3.15 is a projection of three-directional data onto planar tagged images. This is significant because it shows that the tracking algorithm can correctly identify in-plane myocardial motion, but also gives information about thru-plane motion at the same time. Unfortunately, without a separate acquisition of tagged images in the long-axis orientation, we cannot verify the thru-plane accuracy of the computed path.

This study demonstrated that the tissue tracking algorithm can produce accurate results when myocardial velocities acquired using the MR PVM scan protocol are used to compute the movement of myocardial points in-vivo.

Velocity Coordinate System

In the Philips Intera magnet, velocity acquisition is performed in the coordinate system of the imaging slice, which is different from the coordinate system of the MRI scanner. Although myocardial velocities in this study were always acquired in a short axis view, slight variations in cardiac anatomy from person to person mean that these short axis images could have been acquired in the transverse, coronal, or sagittal slice orientations. As Figure 3.17 clearly shows, it is impossible to determine the slice orientation by simply looking at the short axis images; this information must be taken from the DICOM header file.

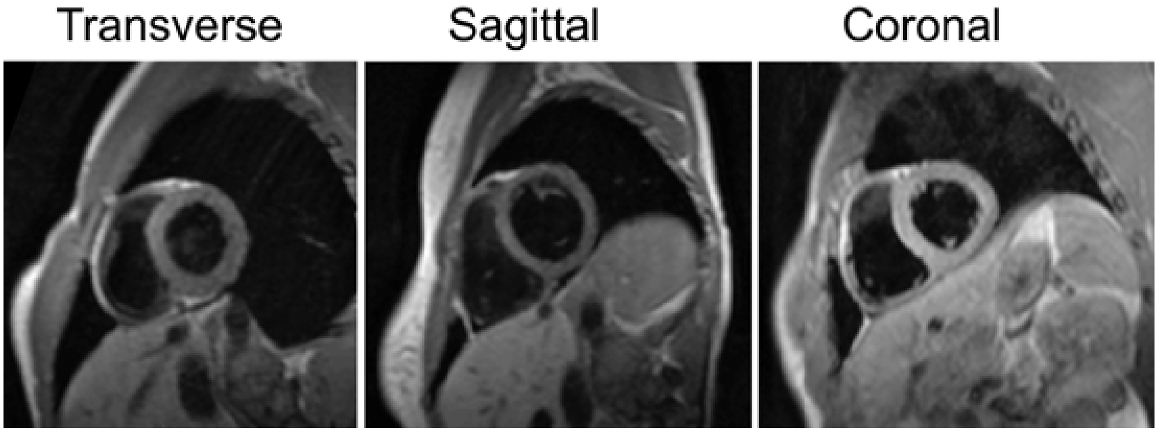

Figure 3.17: Short axis images acquired in different orientations

However, some generalities about cardiac anatomy can be made: the apex of the heart is always located more anterior than the base, and the base of the heart is always more cranial than the apex. With this knowledge, it is possible to create a conversion system so that velocity images from short axis views acquired in transverse, sagittal, and coronal slices can be compared.

As mentioned previously, the direction of velocity encoding moves with the orientation of the imaging slice. This means that regardless of the slice angle or offset, the two in-plane velocity encoding directions will always remain in-plane, and the thru-plane velocity encoding direction will always remain perpendicular to the imaging slice. The different coordinate systems of the magnet and a coronal imaging slice are illustrated in Figure 3.18.

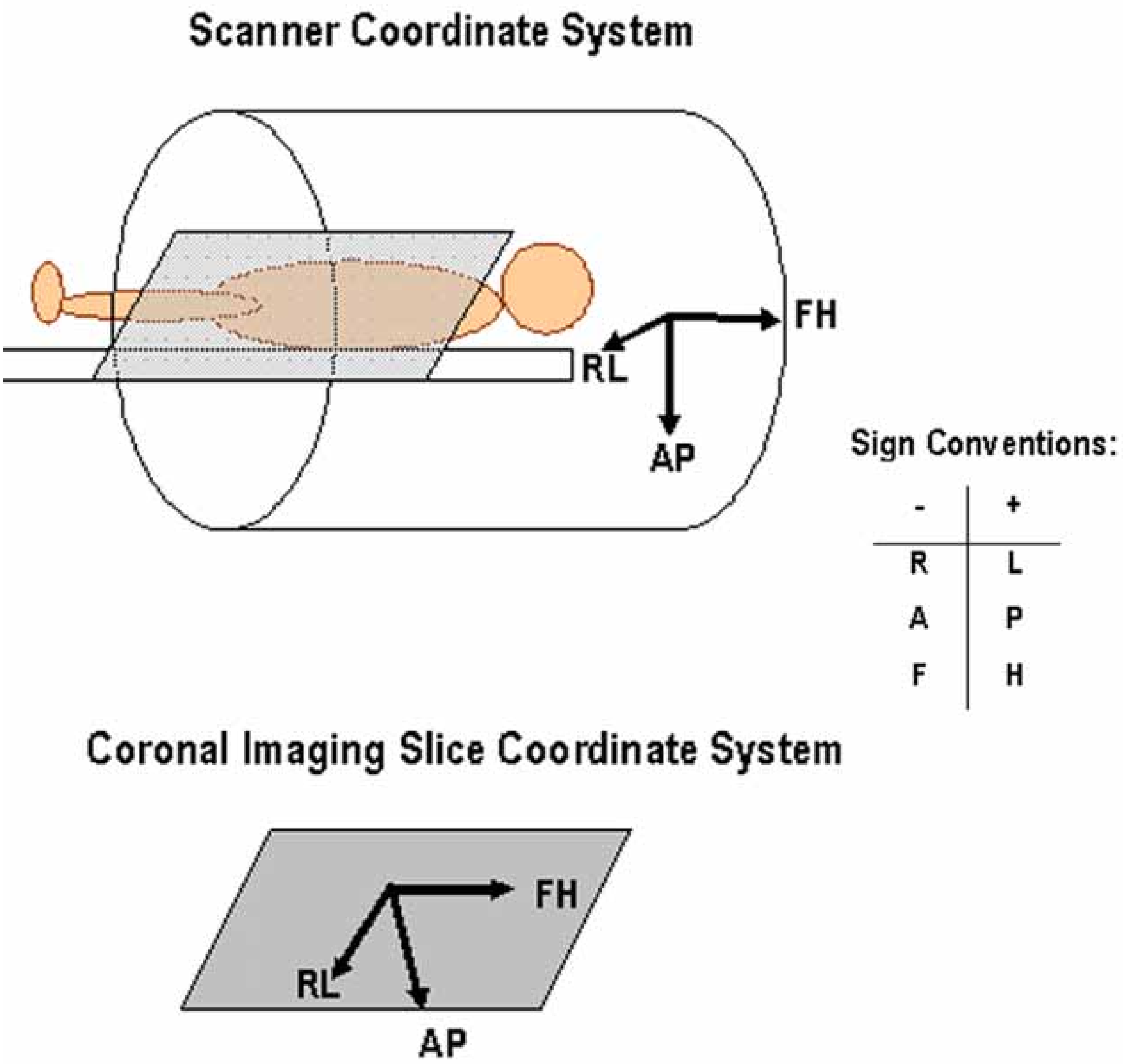

***Figure 3.18**: Coordinate System for the MRI scanner and Imaging Slice*

However, the in-plane and thru-plane velocities will change depending on if the imaging slice is transverse, sagittal, or coronal in orientation. For a transverse slice, the two in-plane directions will always be RL and AP, while the thru-plane direction will always be FH. For a coronal slice, the in-plane velocities will always be RL and FH, while the thru-plane direction will always be AP; for a sagittal imaging slice, AP and FH will be in-plane while RL will always be thru-plane. The Philips convention for velocity encoding is that motion toward the right (R), anterior (A), and foot (F) is encoded as negative, while motion toward the left (L), posterior (P), and head (H) is encoded as positive. On the scanner consol, negative velocities are displayed as dark, while positive velocities are displayed as light. Furthermore, the convention adopted by the Philips Intera magnet is that transverse images are viewed looking from the feet, coronal images are viewed looking from the front, and sagittal images are viewed looking from the left side. Therefore, in the acquired image, the directions considered positive and negative for velocity encoding will vary depending on the orientation of the imaging slice. The coordinate systems for short axis images acquired in transverse, coronal, and sagittal orientations are shown in Figure 3.19.

Let x and y represent the two in-plane directions and z the thru-plane direction in some generic displayed image. If a coordinate system is adopted for this generic image where the origin is located at the upper left hand corner, x is positive to the right, y is positive downward, and z is positive out of the page, a standardized set of transformations can be applied to acquired short axis images such that velocity in all images, regardless of acquisition orientation, is displayed according to the same convention. These transformations are given in Figure 3.19.

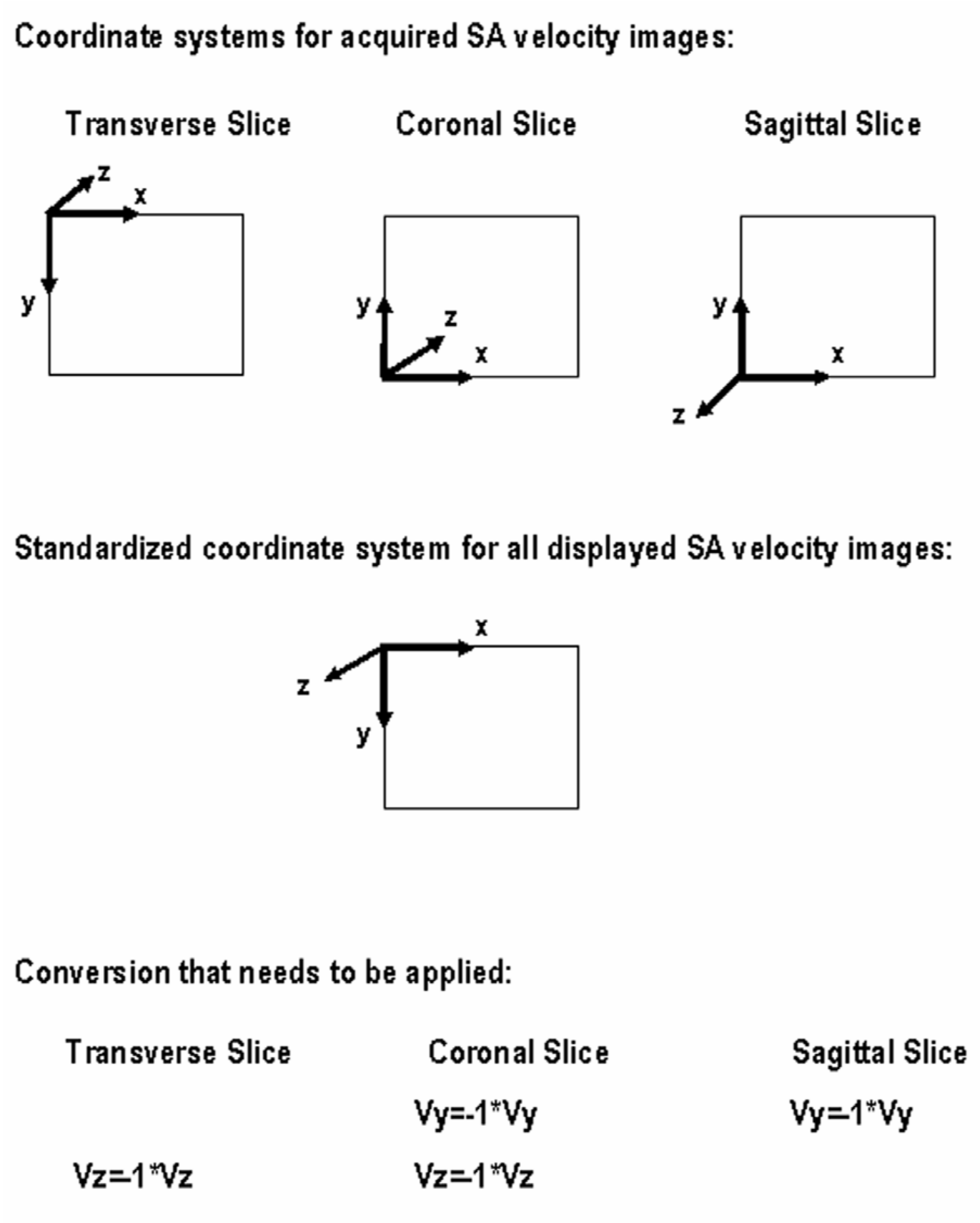

Figure 3.19: *Coordinate systems of acquired and displayed SA velocity images.*

Because these transformations are based on a priori knowledge of the orientation of the heart within the chest cavity, they are only valid for *myocardial short axis images*. It would ***NOT*** be correct to assume that these coordinate transformations applied to all velocity encoded images. Velocity encoded images not in the myocardial short axis orientation will have the same in-plane and thru-plane encoding directions as the SA images, but the positive and negative directions may vary. For example, it is possible to acquire coronal images of descending aortic flow with flow encoded as both positive and negative; if the imaging slice is rotated 44 degrees toward the anterior of the body, descending aortic flow will be encoded as negative; if the slice is oriented 44 degrees towards the posterior of the body, descending aortic flow will be encoded as positive. Figure 3.20 illustrates this phenomenon. It is also important to note that if any slice is rotated more than 45 degrees, the slice orientation will automatically be changed and the in-plane and thru-plane velocity encoding directions will change; for example, a coronal imaging slice rotated 46 degrees toward the anterior of the body automatically becomes a transverse imaging slice.

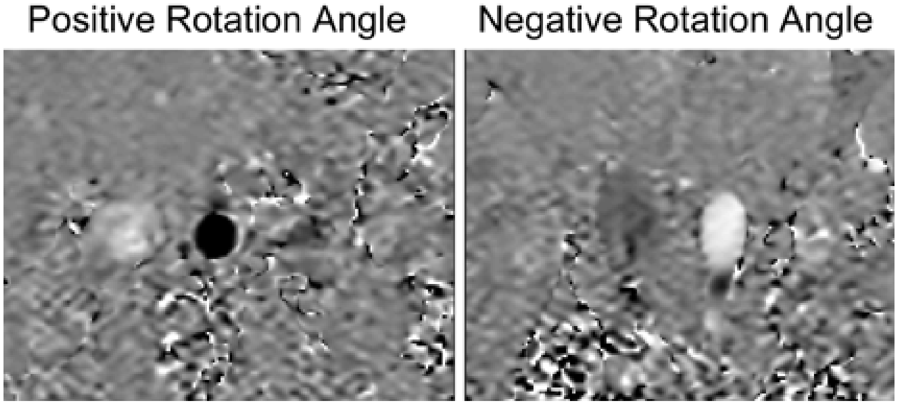

Figure 3.20: Descending aortic flow in a coronal imaging slice.

Once images were transformed into a standardized x,y,z image coordinate system, myocardial velocities were converted into a coordinate system more descriptive of cardiac motion (radial, circumferential, and longitudinal velocities). The center of the LV blood pool was manually selected on an end-diastolic image and was used as a reference point for the velocity conversion. Radial velocity was defined as positive toward the center of the LV blood pool, circumferential velocity was defined as positive for clockwise rotation when viewed from the apex, and longitudinal velocity was described as positive with motion toward the apex.

Image Standardization

Because cardiac anatomy is slightly different for each individual, images need to be standardized to a common template before inter-individual values can be compared. Images were standardized in accordance with American Heart Association recommendations[135]. The inferior RV insertion point was manually identified and was used for registration. In accordance with the AHA 17-segment model, basal and mid slices were divided into six-segments (anterior, anteroseptal, inferoseptal, inferior, inferolateral, and anterolateral), and apical slices were divided into 4-segments (anterior, septal, inferior, and lateral). Figure 3.21 illustrates a Bulls-Eye plot of the standardized AHA model of myocardial segmentation. Because no images were acquired at the LV apex, data was only available for 16 of the 17 segments in the model.

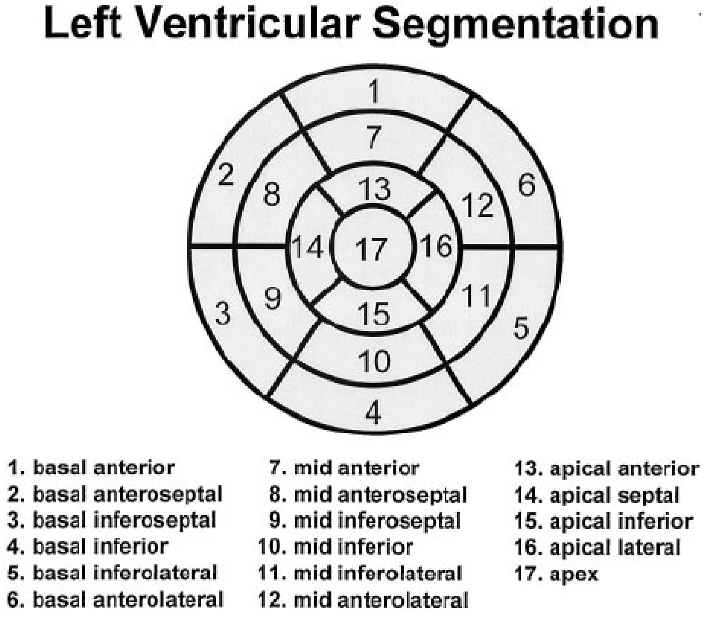

Figure 3.21*: Segmentation of the left ventricle (from Cerqueria et al, Circulation,2002).*

Definition of Systole and Diastole

Systole and diastole in the phase velocity images were defined based on aortic valve opening and closing times. After acquisition of MR PVM velocity data, an additional cine SSFP image was acquired in the LV outflow tract orientation. Systole was defined as the time between aortic valve opening and closing. Diastole was defined as the frame after aortic valve closing thru the end of data acquisition.

Myocardial Segmentation

The myocardium was manually segmented in the MR PVM images. Using the magnitude reconstruction from the MR PVM velocity images, endocardial and epicardial borders were traced throughout the cardiac cycle. Using these borders, a template of the myocardium was created for each phase of the cardiac cycle and velocity data for the myocardium was only analyzed within this template.

CHAPTER 4

AIM 2: CONSTRUCTION OF AN IMAGING PHANTOM, VALIDATION OF MR PVM SCAN ACCURACY, AND OPTIMIZATION OF ACQUISITION PARAMETERS FOR TISSUE TRACKING

Introduction

Motion tracking techniques make it possible to follow individual regions of myocardial tissue throughout the cardiac cycle, thereby overcoming the “fixed frame” limitation inherent in tomographic imaging techniques such as MR PVM[100]. However, the accuracy of the paths computed by the motion tracking algorithm is dependent on the accuracy of the underlying velocity data. Specifically, the spatial and temporal resolution of the velocity data used for tracking have a large influence on tracking accuracy. Temporal resolution affects tracking accuracy by changing the size of the time step used to calculate the next spatial position. Too large of a time step will miss important velocity information and will cause the tracking algorithm to jump to an incorrect position or lead to blurring of the motion tracking curve[131]. Spatial resolution affects tracking accuracy and the reproducibility of MR PVM velocity values. Insufficient spatial resolution (i.e. pixels that are too large) will result in averaging of velocities over large areas and may lead to inaccuracies in the measured velocity maps[131]. This becomes especially problematic when a velocity distribution exists within the voxel volume, such as can occur at the interface of the myocardium and the blood pool, or in regions of the myocardium without uniform velocities.

Ideally, motion tracking should be performed using accurate velocity data that has been acquired with both high spatial and temporal resolution. However, the lack of reference points within the myocardium makes it difficult to verify the accuracy of in-vivo velocity measurements, and imaging time constraints make the acquisition of data at high temporal and spatial resolution unrealistic in a clinical setting. Therefore, the purpose of this study was to: 1) verify accuracy of MR PVM for measuring myocardial tissue velocity in an imaging phantom, and 2) determine how the spatial and temporal resolution of the acquired MR PVM velocity data affects tissue tracking accuracy.

Methods

Description of Motion Phantom

An MRI-compatible phantom capable of three-dimensional movement was built. The phantom consisted of a concentric set of two cylinders rotating in a plane transverse to the MRI bore and moving linearly along the axis of the MRI bore. The outer cylinder had a diameter of 7.5 cm, the inner cylinder had a diameter of 4 cm, and both cylinders were 8cm in length. These cylinders represented the epicardial and endocardial surfaces of the left ventricle. The dimensions of the model were based on *in-vivo* measurements available in the literature[49]. “Myocardial tissue” located between the two cylinders was simulated using a polyvinyl alcohol (PVA) cryogel, a material that has T1 and T2 relaxation times similar to those of myocardial tissue when it undergoes three freeze-thaw cycles[136]. A removable end plate was fixed to the distal end of the cylinder assembly allowing the space between concentric cylinders to be filled with PVA cryogel. O-rings between the end plate and the cylinder ends ensured a water-tight seal.

Movement of the myocardial phantom was controlled by two computer-controlled piezo-powered high-force motors (Bayside manufacturing, Port Washington, NY). One motor moved the phantom linearly along the axis of the MRI bore (z-direction), while the other motor rotated the phantom in a plane transverse to the MRI bore (x-y plane). A 3 meter long, 2.5cm diameter acrylic rod attached the cylindrical myocardial phantom with the computer-controlled motors, allowing the motors to remain outside the 5-gauss line of the MRI scanner. Detailed calculations on the rotational shear, bending moment, and deflection in the control rod indicated that the deformation of the rod during rotation was negligible, with maximum position error from the cylinder to the motor at less than 0.2 mm. The acrylic rod rested on a series of support cradles that allowed the phantom to rotate and translate freely. The wooden supports were lined with Teflon to minimize friction and 10cm in height to ensure that the position of the cylinder correctly simulated the position of the human heart within the MRI scanner bore.

The piezo-control motors were not magnetically-driven, so the fringe magnetic field (<5 gauss) of the scanner did not affect their performance or accuracy. The motors were controlled through an amplified servo-control mechanism. The input signal to the servo control system was a 2-channel, time-varying analog signal, (0-5 Volts), where voltage was linearly related to motion. Channel #1 corresponded to linear (z-direction) translational motion and channel #2 corresponded to rotation in the x-y plane.

The motors were physically coupled and directed by a control program, Galil, (Rocklin, California) which ran on a PC. The Galil program accepted ASCII data in “time-versus-motion” pairs for each channel and provided an output signal to the servo controller to move the model. The program was set to continuously repeat motion in order to simulate the multiple heartbeats needed to complete the scan. The control program on the computer also provided a 5 volt trigger pulse at the start of the motion cycle, which served as an ECG trigger input to the MRI scanner.

The system was equipped with a series of feed-back sensors that measured the actual displacements of both motors versus time. The sensors recorded the exact position versus time curve experienced by the phantom. The displacement information from these sensors served as gold standard of the phantom position. Therefore, knowledge of the true motion of the phantom was known at each time point.

The LV phantom was placed inside of a static chest wall phantom during imaging. The chest wall phantom consisted of two concentric cylinders filled with the same PVA-cryogel as the LV phantom. The outer cylinder had a diameter of 26cm and the inner cylinder had a diameter of 18cm. Velocity in the static chest wall was used for background phase offset correction in the same manner as was done in the in-vivo studies.

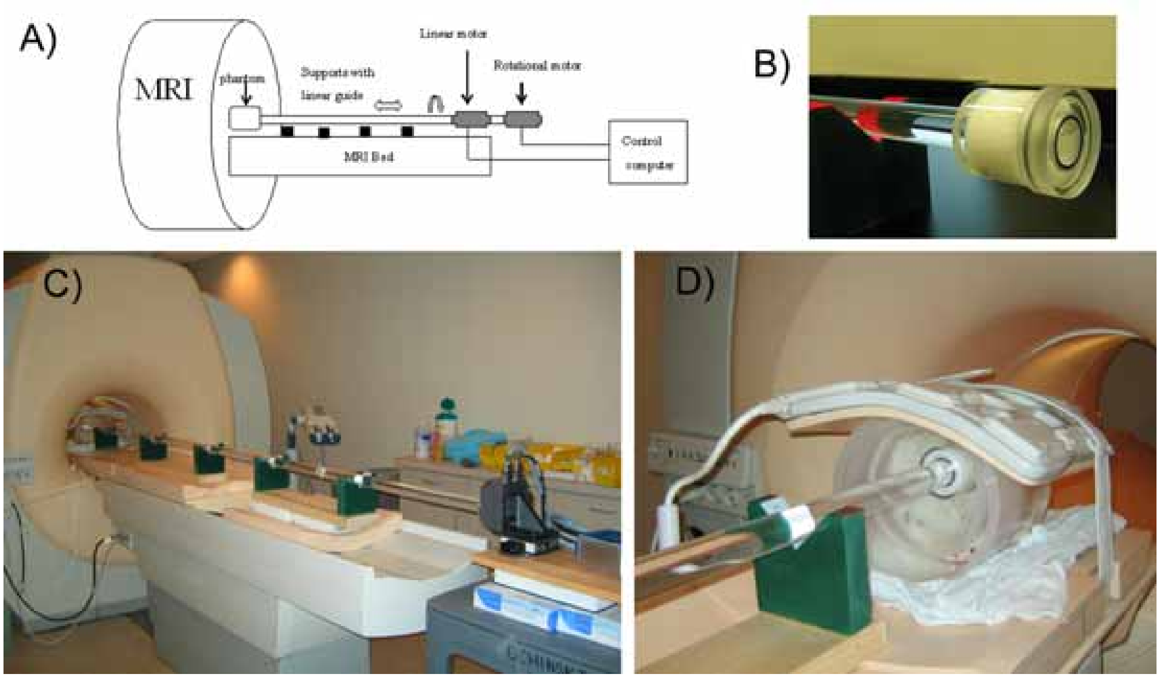

Figure 4.1: *The myocardial motion phantom*

A schematic of the motion phantom is shown in Figure 4.1A. Figure 4.1B shows a close up of the cylindrical "left ventricle". Figure 4.1C illustrates how the phantom was setup within the MRI magnet, with the LV phantom located within the magnet's bore, and the computer controlled motors are outside of the 5-gauss line. Figure 4.1D shows a close up of the LV phantom within the magnet and the static "chest wall" used for background phase offset correction.

Verification of MR PVM Scan Accuracy

Velocity within the myocardial motion phantom was imaged using the MR PVM scan protocol developed in Chapter 3. Background phase errors were removed using a least-squares plane fitted to the outer ring of static tissue, as was also described in Chapter 3. In accordance with the myocardial coordinate system, the acquired three-directional velocities were converted to radial velocity (positive toward the center of the LV blood pool), longitudinal velocity (positive toward the apex), and circumferential velocity (positive for clockwise rotation when viewed from the apex) using the center of LV bloodpool as a reference point.

Velocities were measured within four 8x8mm regions of interest (ROIs) within the phantom (septal, lateral, anterior, inferior walls). Curves of velocity versus time in all three-directions of motion (radial, longitudinal, circumferential) were generated for each ROI. Peak systolic and diastolic velocities, as well as the *time-to-peak* systolic and diastolic velocities, were computed for each ROI.

Correlation between measured and true values was determined via linear correlation analysis. Measured and true values were also compared using a modified Bland-Altman analysis where the difference between the two values was plotted against the known true value, instead of the average of the two[137].

Tissue Tracking within the Motion Phantom

Motion tracking was performed using the acquired velocity data. After background phase correction was performed, a motion trajectory was computed for each pixel within the myocardial phantom.

The motion tracking algorithm generated positional data for each pixel within the myocardium at each time point in the cardiac cycle [position(x,y,z,t)]. The feedback sensors on the motion control system provided the same information about the exact location of the imaging phantom. This allowed the trajectory computed by the motion-tracking algorithm to be quantitatively compared to the true trajectory of the motion controlled phantom. The error between the path computed by the tissue tracking algorithm and the feedback data from the sensors (the reference standard) was calculated as:

$$E_t=[(x_{ref}-x_{pvm})^2+(y_{ref}-y_{pvm})^2+(z_{ref}-z_{pvm})^2]^{1/2}$$

where t is the time step between imaging frames. The total error, RMSE = ΣE_t, was calculated as the sum of error values over time. Therefore, RMSE was the integrated error of each pixel's path throughout the entire cardiac cycle. For each scan, an average RMSE value over the entire myocardial phantom throughout the entire cardiac cycle was computed. Error percentage in any given trajectory was calculated as the average RMSE divided by the true path length.

Temporal Resolution

To test the effects of temporal resolution on tracking accuracy, the temporal resolution of the MR PVM scan was varied by changing the number of k-space lines acquired per cardiac phase. Velocity data was acquired in six different scans, during which the number of k-space lines acquired per cardiac phase was varied from 3 to 13.

This resulted in a frame-to-frame temporal resolution of between18msec (3 lines of k-space/phase) and 82 msec (13 lines of k-space/phase). All other scan parameters were held constant; spatial resolution was fixed at a FOV 370mm and a scan matrix of 144 was used for all scans. All six scan were acquired in a single imaging sequence. The entire protocol was repeated on three different days to assess reproducibility.

Images were processed as described previously, the tissue tracking algorithm was performed in all datasets, and an average RMSE error value was computed for each temporal resolution value.

Spatial Resolution

Spatial resolution can be changed by either altering the scan matrix or the image field-of-view (FOV). For optimization of imaging parameters using the phantom, FOV was fixed and the matrix size was altered. In order to make the phantom studies resemble in-vivo conditions as closely as possible, a FOV of 370mm was chosen. This large FOV was deemed sufficient to eliminate foldover in most patient studies. Theoretically, foldover in static tissue regions should not affect the velocity values in the phase image; however, we have found that foldover artifacts do introduce errors when using background static tissue to correct the background phase errors. This is a significant finding, as accurate background phase correction is critical when performing measurements of the low velocities within the myocardium.

With the FOV held constant at 370mm, seven different scans were acquired in which the scan matrix was varied from 64 to 192. All other scan parameters were held constant; temporal resolution was fixed at 3 lines of k-space/phase. All scans were reconstructed to a matrix size of 256. Velocity data for all seven scans was acquired in a single imaging session, and the entire protocol was repeated on three different days to asses reproducibility.

Images were processed as described previously, the tissue tracking algorithm was carried out in all datasets, and an average RMSE error value was computed for each value of spatial resolution.

Results

Verification of MR PVM Scan Accuracy

Excellent correlation was observed between the motion recorded by the feedback sensors and the velocity determined by MR PVM. The correlation coefficient was 0.90 for longitudinal velocity and 0.93 for circumferential velocity. Plots of velocity vs. time showing both the true and measured velocity are shown in Figure 4.2. The true motion of the phantom is shown in black, and velocity curves from the four regions of interest within the myocardial phantom are shown in red.

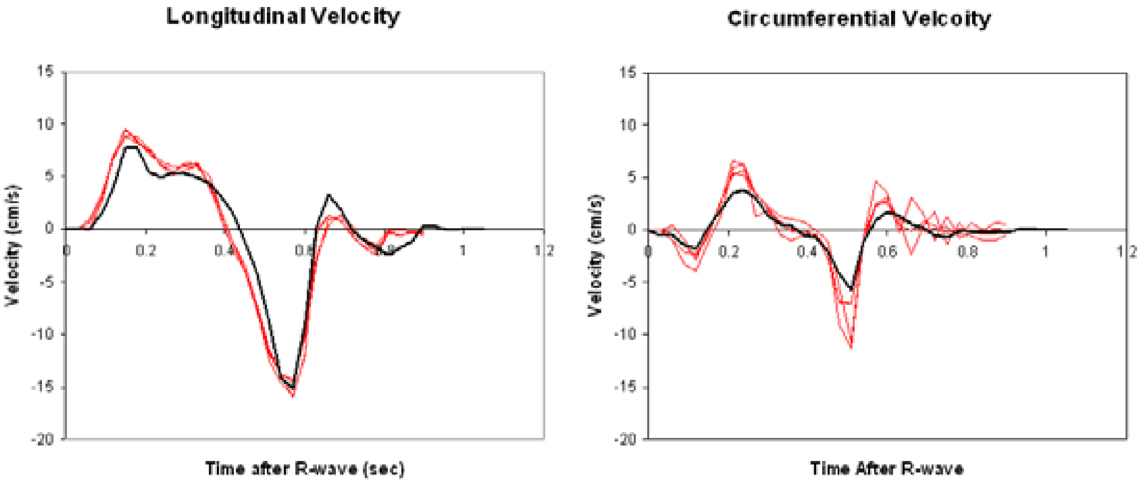

***Figure 4.2**: Velocity curves from the phantom experiments.*

MR PVM accurately detected velocities within the phantom: mean difference between the measured and true velocity throughout the cardiac cycle computed via Bland-Altman analysis was -0.15+/-2.8cm/s in the longitudinal direction and 0.06+/-1.38 cm/s in the circumferential direction.

Peak systolic and diastolic velocities measured by MR PVM were an average of 1.0+/- 0.9 cm/s greater in magnitude than true velocities in the longitudinal direction and an average of 3.2+/-1.9 cm/s larger in the circumferential direction.

MR PVM was accurate in determining the timing of peak velocities: mean difference between measured and input was 9.4+/-24.4 msec in the longitudinal direction and 1.0+/-20.3 msec in the circumferential direction. The temporal resolution of the scan was approximately 30msec, so the observed differences are less than one time frame. Table 4.1 gives the actual measured and true values for peak velocities and time-to-peak velocities within the motion phantom.

Table 4.1: Peak and Time-to-Peak Velocity Measurements in the phantom

	Longitudinal		**Circumferential**	
	True	**Measured**	**True**	**Measured**
Peak Systolic Velocity (cm/s)	7.8	9.3+/-0.4	3.8	7.0+/-1.0
Peak Diastolic Velocity (cm/s)	15.1	15.8+/-1.1	5.8	10.0+/-1.7
Time-to-Peak Systolic Velocity (msec)	180.0	185.5+/-9.0	240.0	240.0+/-1.0
Time-to-Peak Diastolic Velocity (msec)	570.0	604.0+/-10.4	510.0	517.5+/-9.0

Tissue Tracking within the Motion Phantom

Average path length within the myocardial phantom was 38.6mm. Computed trajectories within the phantom correctly followed the motion prescribed by the motors. Trajectories computed for individual pixels did not intersect and exhibited the parallel trajectories expected for the rigid body phantom. The three-dimensional trajectories showed circumferential and longitudinal displacement, with the greatest amount of displacement along the longitudinal (z) direction. Figure 4.3 illustrates three-dimensional trajectories computed within the phantom. For clarity, only the trajectory of every third pixel is shown. Note that, as expected, the trajectories of all pixels within the rigid body phantom are identical. Also note that none of the trajectories lose their course throughout the cardiac cycle and deviate from the expected path.

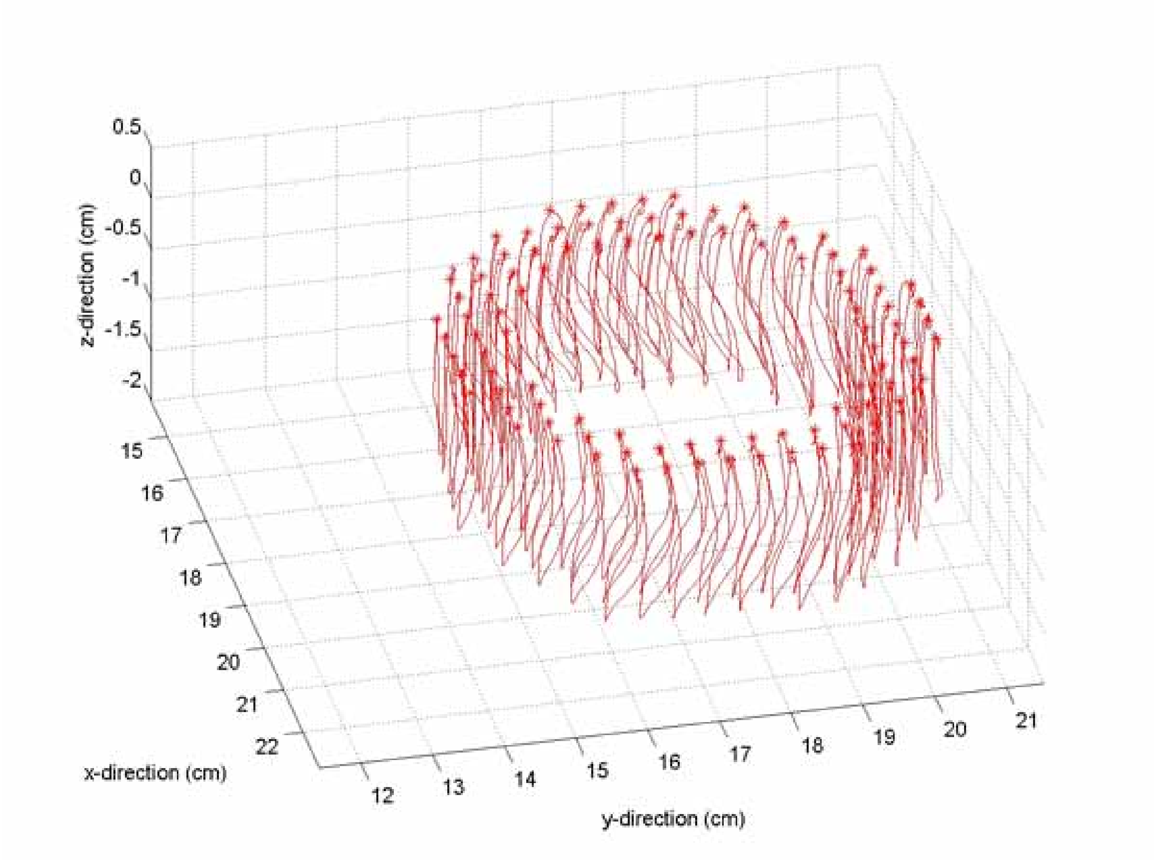

***Figure 4.3**: Computed 3D motion trajectory within the LV phantom.*

The maximum expected displacement of the phantom in the longitudinal direction was 16.3mm; an average maximum displacement of 15.1+/-0.45mm was observed in the path calculated by the motion tracking algorithm. In the in-plane direction, an average maximum displacement of 3.0+/-0.31mm was expected and an average maximum displacement of 3.2+/-0.57mm was observed.

Temporal Resolution

A strong relationship was observed between tracking accuracy and temporal resolution, with higher temporal resolution resulting in lower error values. As is clearly illustrated in Figure 4.4, the relationship between temporal resolution and tracking accuracy was approximately linear: RMSE= 0.04*temp res + 0.32, (R^2=0.91). Table 4.2 lists the effective temporal resolution, computed RMSE error, and % error for each of the six different scans. Recall that each scan was repeated three separate times, so the values given are an average of the three trials.

Table 4.2: *Effects of temporal resolution on tracking accuracy*

# k-space lines	Temp res (msec)	RMSE (mm)	% error (%)
3	18.0	1.3+/-0.2	3.3+/-0.5
5	30.0	1.7+/-0.7	4.5+/-1.7
7	42.9	1.8+/-0.7	4.8+/-1.9
9	52.9	2.1+/-0.6	5.5+/-1.6
11	64.3	2.7+/-1.1	7.1+/-2.8
13	81.8	4.1+/-1.5	10.6+/-3.8

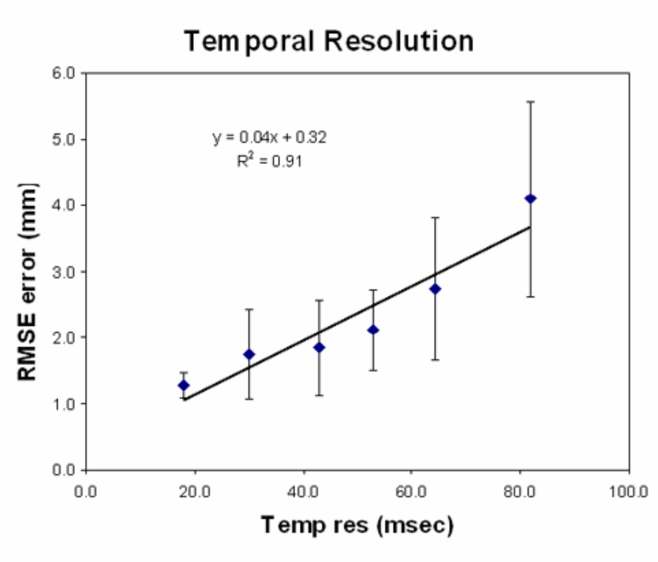

***Figure 4.4**: Effect of temporal resolution on tracking accuracy.*

Figure 4.5 shows the effect of temporal resolution on tracking accuracy. Figure 4.5A shows the true motion of the phantom. Because the phantom did not have any radial thickening, the trajectories of individual pixels remain in the same radial position throughout the cardiac cycle. Note that the tracking algorithm computed a three-dimensional trajectory, and that the paths shown in Figure 4.5 are projections of that three-dimensional motion onto a two-dimensional plane; there is also significant through-plane motion which is not shown. Figure 4.5B shows the a 2D projection of the trajectories computed by the motion tracking algorithm from MR PVM velocity data acquired at a temporal resolution of 18msec; figure 4.5C shows the same for a temporal resolution of 82msec. It is clearly visible that the error in the computed path increased as the frame-to-frame interval increased.

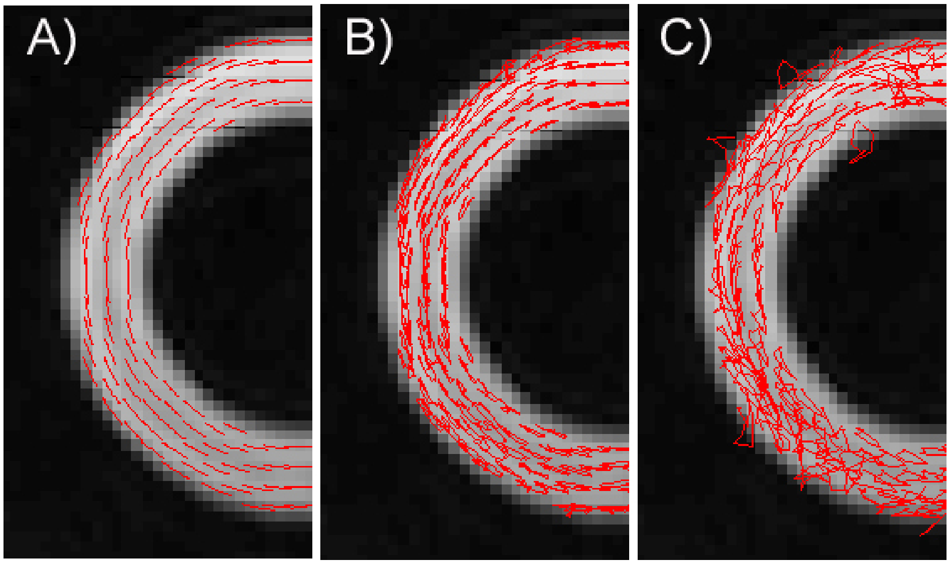

Figure 4.5*: Computed trajectories with varying temporal resolutions.*

Spatial Resolution

A weak relationship was observed between the spatial resolution of the MR PVM scan and tracking accuracy. A linear regression approximated the relationship as: RMSE=-0.08*spatial resolution+1.66 (R^2=0.18), Figure 4.6. Table 4.3 lists the effective spatial resolution, computed RMSE error, and % error for each of the seven different scans. Recall that each scan was repeated three separate times, so the values given are an average of the three trials.

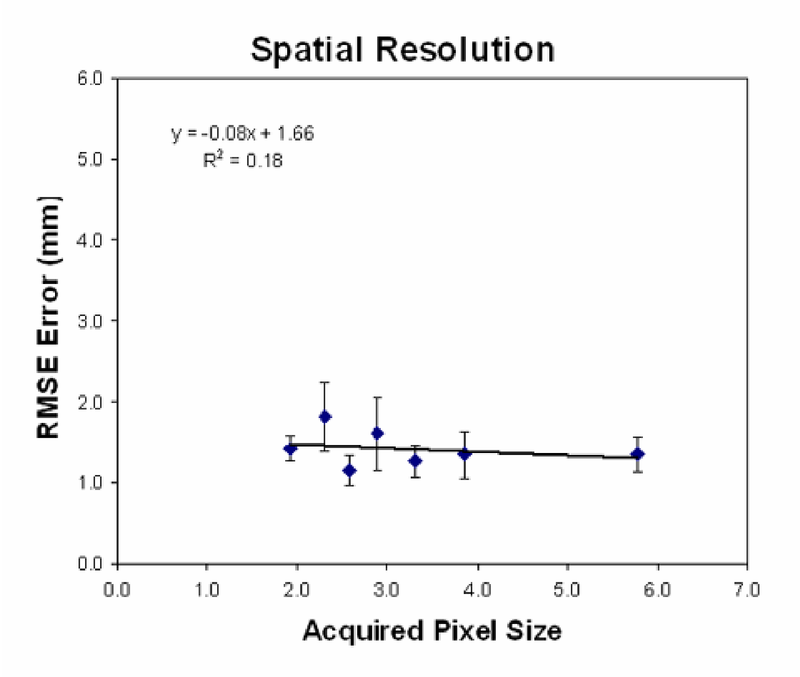

***Figure 4.6**: Effect of spatial resolution on tracking accuracy.*

***Table 4.3**- Effects of spatial resolution on tracking accuracy*

Scan matrix	Acquired pixel size (mm)	RMSE (mm)	% error (%)
64	5.8	1.4+/-0.2	3.5+/-0.5
96	3.9	1.3+/-0.3	3.5+/-0.7
112	3.3	1.3+/-0.2	3.3+/-0.5
128	2.9	1.6+/-0.5	4.2+/-1.2
144	2.6	1.2+/-0.2	3.0+/-0.5
160	2.3	1.8+/-0.4	4.7+/-1.1
192	1.9	1.4+/-0.2	3.7+/-0.4

Discussion

An MRI-compatible motion phantom was built and used to verify the accuracy of MR PVM for measuring myocardial tissue velocities. MR PVM measurements of peak velocities and time-to-peak velocities within the phantom were accurate and correlated well with the known true motion of the phantom. A set of experiments investigating the effects of spatial and temporal resolution in MR PVM velocity data used for motion tracking suggested that high temporal resolution is much more crucial to generating accurate tracking trajectories than high spatial resolution.

Previous Validations of MR PVM

The ability of MR PVM to correctly measure blood flow velocity has previously been demonstrated, both in-vivo and in-vitro[138-143]. Although tissue velocity imaging employs the same MR pulse-sequence as blood flow imaging, the lower velocities of myocardial tissue present some unique problems. Background phase offset correction is especially important when measuring the lower velocities of myocardial tissue, as the background phase errors are the same order of magnitude as the desired signal from myocardial tissue. Lower velocities require higher gradients, which require longer echo times and higher bandwidths. Therefore, it is important that the accuracy of the MR PVM technique for imaging myocardial tissue motion be verified in a motion phantom before being applied in-vivo.

This study verified the ability of MR PVM to measure the lower velocities of the myocardium: mean difference between measured and true velocities was -0.15+/-2.8cm/s in the longitudinal direction and 0.06+/-1.38 cm/s in the circumferential direction. Given that a Venc of 20cm/s was employed, these errors are less than 1% of the dynamic range.

Motion Tracking Techniques

Although MR PVM images can accurately capture myocardial velocity information, motion can be difficult to interpret from the acquired velocity images. Tissue tracking techniques allow the measured velocity information to be transformed into displacement, making the information easier to interpret.

The accuracy of the path generated by the tissue tracking algorithm is a function of the accuracy of the underlying velocity data. Residual phase from eddy currents or Maxwell effects can introduce errors into the velocity images. Therefore, it is necessary that background phase correction be carried out prior to tracking. Instead of relying on the local phase correction filters in the Intera software, we opted to carry out background phase correction manually using an algorithm based on a least-squares fit to the residual phase errors[130]. While this added an extra step to the data processing, it allowed for greater control of the data and ensured that residual phase errors were correctly removed.

The motion tracking algorithm applied in this study has previously been implemented both in-vivo and in-vitro, and has been verified to be accurate in both a phantom model and in vivo[100,131,132]. However, in previous studies, the motion tracking algorithm was only evaluated using velocity data acquired at a single temporal resolution. While it has previously been reported that a "substantial improvement" in tracking accuracy was observed when the number of reconstructed velocity frames was increased[132], this is the first study to systematically and quantitatively investigate the effects of temporal resolution in the underlying velocity data on tracking accuracy. Our findings are in accordance with previous observations that temporal resolution of the underlying velocity data is a critical factor for generating accurate tracking results; we extend those findings quantitatively to demonstrate that a temporal resolution of at least 40msec is necessary to keep error values within the computed trajectories to under 5% (Table 4.2).

Motion tracking from MR PVM velocity data can be performed using other methods than the one employed in this paper. Methods in which cardiac motion is modeled as a series of Fourier harmonics and tissue tracking is carried out in the Fourier domain have been previously introduced[133,144,145]. These methods have the advantage that eddy currents and other sources of phase error, which affect only the DC component of velocity, can easily be removed from the velocity data. However, Fourier-based tracking methods are computationally intensive and more sensitive to noise. Since we were able to demonstrate sufficient tracking accuracy when the simple forward-backward tissue tracking algorithm was employed with high-temporal resolution velocity data, we did not feel the need to explore the Fourier tracking methods at this time.

Study Limitations

The ideal myocardial motion phantom would be able to correctly replicate all of the complex motions of the myocardium: displacement, thickening, torsion, and shear. Several MR-compatible phantoms have previously been designed to simulate some aspect of this complex myocardial motion[146-149]. These have ranged from simple rotating disk phantoms[147] to a complex re-creations of myocardial displacement and shear[148,149]. Each of these designs has both some attractive features and some drawbacks. The simple bulk-motion phantoms are easy to construct and the exact motion at every point within the phantom is easily determined. The drawback of a rigid body design, however, is that the motion of the phantom is an incomplete representation of myocardial motion. The more complex phantoms which incorporate twisting, bulk motion, and shear are attractive because they more closely mimic the true motion of the myocardium. The drawbacks of these complex designs are that the phantoms are difficult to construct and the motion of individual points within the phantom are difficult to determine. Therefore, these phantoms rely on either an analytical solution to solve for the motion of points within the phantom[149], or some independent verification of motion, such as placing optical markers within the phantom and using digitized video to track the motion of individual points[148]. However, these techniques are less than ideal, as many simplifying assumptions need to be made to derive an analytical solution, and optical markers cannot be placed at every point within the phantom.

In light of these limitations, we elected to construct a rigid body phantom capable of three-directional movement. Although the phantom was a greatly simplified model of the myocardium, the motion of every point within the phantom was known, and thus, the phantom was sufficient for validating the accuracy of the MR PVM imaging technique. Furthermore, the phantom made it possible to optimize the scan parameters for imaging myocardial motion with the MR PVM protocol.

Results from the phantom study suggest that the spatial resolution of the MR PVM velocity data has minimal impact on tracking accuracy. Although this conclusion is true in the rigid body phantom, it needs to be noted that this finding may not hold in-vivo. In the rigid body phantom, all regions of the LV moved as a single piece. This means that there was no velocity gradient along the phantom, aside from a small difference in circumferential velocity between the inner and outer edges of the LV phantom. Therefore, averaging velocity from larger myocardial regions into single pixels would have had minimal affect on the velocity within that pixel. In an in-vivo situation where myocardial velocities show regional variability—as might be the case for a failing or infarcted heart—spatial resolution may have a much greater impact on tracking accuracy. A deformable phantom with a radial velocity gradient is needed to further investigate this claim.

Nevertheless, the MR PVM velocity scan protocol was too long to be implemented with both high spatial and temporal resolution in a clinical setting. Therefore, we needed to reduce the imaging time by sacrificing either spatial or temporal resolution. Since the results of this study highlighted the importance of good temporal resolution, in the final protocol we elected to keep the highest possible temporal resolution (3 lines of k-space/phase), and decrease the spatial resolution to reduce the total imaging time. In the final three-slice imaging protocol, the scan matrix was 144 with at FOV of 370mm.

Conclusions

A motion phantom simulating the movement of the left ventricle was constructed. The accuracy of MR PVM for measuring myocardial tissue velocities was verified using the motion phantom. The effects of spatial and temporal resolution on MR PVM scan accuracy were investigated, and temporal resolution was found to have a much greater influence on tracking accuracy than spatial resolution. Based on these results, the optimal scan for use in-vivo was determined to need high temporal, but not necessarily high spatial, resolution.

CHAPTER 5

COMPARISON OF MR PVM AND TDI MYOCARDIAL TISSUE VELOCITIES

Introduction

Tissue Doppler Imaging (TDI) has been used to measure myocardial contraction and relaxation velocities and to identify the presence of mechanical delays in dyssynchrony patients[29,72-74]. TDI measurements such as septal-to-posterior wall motion delay, time-to-peak systolic velocity, and the standard deviation of the time-to-peak velocity across the LV may predict response to CRT[29]. Limitations of TDI include its ability to retrieve velocity information only for objects moving directly toward or away from the transducer and the imaging constraints imposed by limited echocardiographic windows across the chest.

MR phase velocity mapping (MR PVM) has been used extensively to measure blood flow velocity. As has been shown in chapters 3 and 4, MR PVM can be adapted to measure the lower velocities of myocardial wall motion. Therefore, MR PVM can obtain data similar to TDI without the limitations imposed by acoustical windows. Furthermore, MR PVM can acquire *multidirectional* velocity information at any location within the left ventricle and can acquire velocity information for each voxel within the myocardium, thus providing a detailed three-dimensional description of motion for the entire myocardium[53,94,95,138,150]. However, MR PVM has not been evaluated in patients with dyssynchrony, has not been rigorously compared to TDI, and the repeatability of both velocity measurement techniques has not been evaluated in the same set of subjects.

The purpose of this study was 1) to compare longitudinal myocardial velocity and time-to-peak longitudinal velocity obtained with MR PVM and TDI in normal subjects and patients with LV dyssynchrony and 2) to assess the reproducibility of both MR PVM and TDI by performing repeated measurements in normal subjects.

Methods

Study Population

Ten normal volunteers (age=27.5+/-6.9 yrs, 5 male) and ten consecutive patients (age=64.9+/-16.1 yrs, 5 male) scheduled for CRT participated in this prospective evaluation of the two imaging techniques. The CRT patients had heart failure with NYHA functional class III (range II/III-III/IV), ECG evidence of dyssynchrony (QRS>120msec) and LVEF < 35%. Medications included ß-blockers, Ace inhibitors/angiotensinogen receptor blockers, diuretics, aldosterone antagonists, and Digoxin. The imaging protocol was the same for both patients and normal subjects, with the MRI exam preceding the echocardiographic-TDI examination. Normal subjects completed the protocol twice (most on consecutive days) to test reproducibility. The Institutional Review Board approved the study protocol, and all participants gave written informed consent before participation.

MR PVM Imaging

MRI exams were acquired using the final velocity imaging protocol described in Chapter 3, but with velocity only being acquired in a single, basal short axis slice. Scout images preceded acquisition of 2-chamber, four chamber, and short axis steady-state free procession (SSFP) cine images. The length of the left ventricle (from apex to the mitral valve plane) was measured on the end-diastolic 2-chamber image, and a short axis orientation located 70% of the distance from the apex to base was chosen for the MR PVM scan. (70% of the LV length was chosen for slice placement to capture maximal myocardial motion without having myocardial tissue leave the imaging slice during the cardiac cycle.)

Background phase errors were removed from the MR PVM data as described previously. Only longitudinal (thru-plane) myocardial tissue velocities were considered in this study, as this was the only velocity direction that could be measured with TDI. Longitudinal velocity toward the apex was defined as positive. Velocity was averaged in 8x8mm regions of interest in the septal and lateral walls, yielding velocity versus time data for each ROI. Curves were exported to a spreadsheet for analysis.

TDI Imaging

Tissue Doppler Imaging (TDI) was performed using a General Electric Vivid 7 system (GE Medical Systems, Waukesha, WI) immediately following the MR scan. Longitudinal (apex-to-base) velocities in the septal and lateral myocardial walls were obtained in the 4-chamber view by digital color-coded TDI at a frame rate of 147frames/sec. TDI velocities were corrected for the angle between longitudinal orientation of the ventricular walls and the Doppler beam. (Corrected Velocity =Measured Velocity/cos Θ, where Θ is the angle between the Doppler beam and the motion of the myocardial wall). Regions of interest (8x8 mm) were placed in the myocardial wall at 70% of the distance from apex to base (to correspond to the location examined by MR). Values of longitudinal velocity versus time were exported to a spreadsheet for analysis.

Data Analysis

Agreement between MR and TDI velocity measurements was computed using linear regression analysis. MR velocity values were interpolated to yield MR-TDI data pairs at each time point. MR and TDI velocities were compared at each time point in both the septal and the lateral ROIs. Curves were registered using the R-wave from the EKG signals. A regression line and correlation coefficient were calculated based on all pairs of MR-TDI data points. In addition, the data was subdivided into normal volunteers, patients, lateral and septal walls, and separate correlation coefficients were calculated for each subgroup.

Peak velocities during both systole and diastole, and the time-to-peak velocities were compared between MR and TDI using a paired, two-tailed Student's t-test. P-values <0.05 were considered to be statistically significant. The coefficient of variation was computed as the standard deviation of repeated measurements divided by their mean.

A Bland-Altman analysis was conducted to analyze the agreement between the two velocity measurement techniques[137]. Dyssynchrony was assessed as the absolute difference between time-to-peak systolic velocity in the septal and lateral walls[24,29,151,152]. Repeatability of both MR and TDI data was assessed by comparing the peak velocity (both systolic and diastolic) and the time-to-peak velocity between repeated scans using a Bland-Altman analysis[137].

Results

Comparison of peak velocity measurements

Velocities measured with MR PVM correlated well with velocities measured by TDI in both normal subjects and dyssynchrony patients (r=0.86). The correlation coefficient was greater for normal subjects (0.88 in the septal wall, 0.88 in the lateral wall) than for dyssynchrony patients (0.78 in the septal wall, 0.72 in the lateral wall). Example of TDI (triangles) and MR PVM (squares) velocities measured in the septal ROI for a normal volunteer (left) and a dyssynchrony patient (right) are shown in Figure 5.1. Note the high correlation between the curves (r=0.926 for the normal volunteer, r=0.910 for the dyssynchrony patient), but that peak systolic and diastolic velocities are higher in magnitude when measured by MR. .

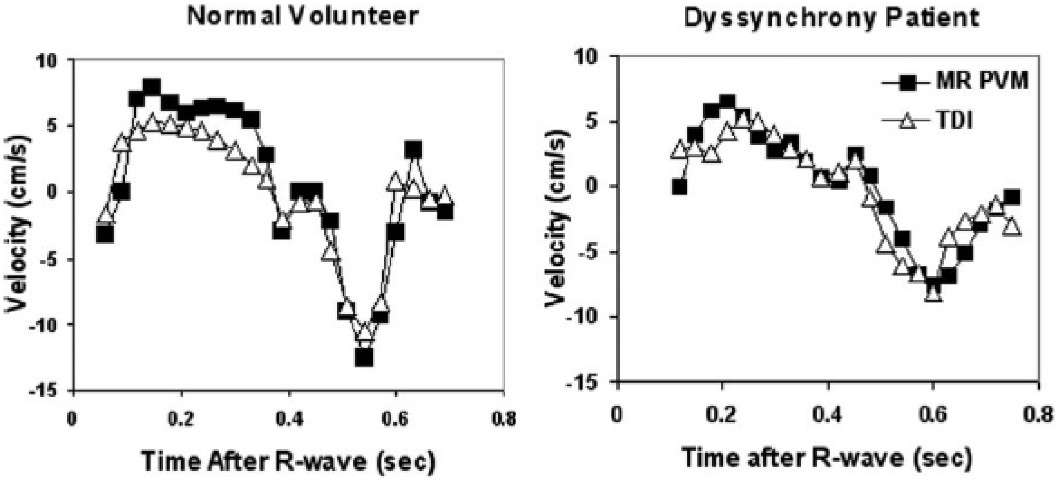

Figure 5.1: Example MR PVM and TDI velocity curves

Velocities measured by MR consistently exceeded velocities measured by TDI in both patients and volunteers, with the regression line for all data points being TDI=0.60*MR-0.8. Figure 5.2 shows the peak systolic and peak diastolic velocity values measured by MR and TDI in a regression plot. The dotted line represents the identity line and the solid line is the line fitted to the correlation. (For clarity, the figure shows only the peak velocity values, not all measured velocity values). The regression line for peak velocities is TDI=0.59*MR+0.3 (r=0.96).

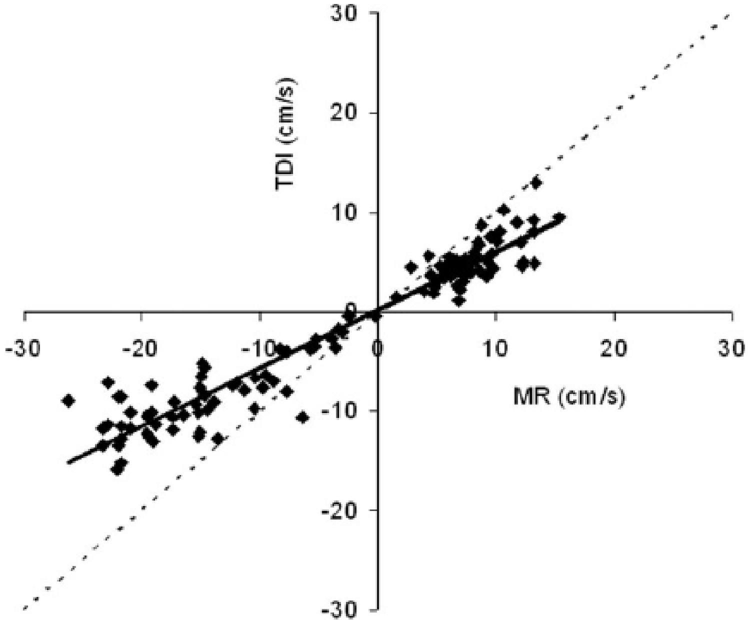

Figure 5.2*: Peak velocities measured by MR and TDI*

Table 5.1 lists the values of peak velocities measured in the normal volunteers and the dyssynchrony patients during systole and diastole. The average peak systolic velocity in normal subjects measured by MR exceeded the TDI velocity, both in the septum and lateral wall. The MR peak diastolic velocities also exceeded the TDI velocities, both in the septum and lateral wall.

Velocity measurements in the dyssynchrony patients showed similar results. MR peak systolic velocities were significantly greater than TDI velocities in the lateral wall, but not in the septum. Diastolic peak diastolic velocities measured by MR were significantly greater than TDI velocities in the septum, but not in the lateral wall.

***Table 5.1**: Peak Velocities Measured by MR PVM and TDI*

	Systolic Velocity (cm/s)				**Peak Diastolic Velocity (cm/s)**			
	Septal Wall		Lateral Wall		Septal Wall		Lateral Wall	
	Normals	Patients	Normals	Patients	Normals	Patients	Normals	Patients
MR	7.3+/-1.4	5.3+/-1.4	10.7+/-2.4	5.7+/-1.9	-16.3+/-4.1	-6.4+/-3.1	-19.5+/-3.7	-7.1+/-4.7
TDI	5.0+/-1.1	3.8+/-1.4	6.9+/-2.5	3.0+/-1.3	-8.5+/-1.6	-4.3+/-2.6	-11.7+/-2.2	-5.4+/-4.1
	p<0.001	P=NS	p<0.001	p<0.005	p<0.001	p<0.005	p<0.001	P=NS

Figure 5.3 shows the peak systolic (left) and peak diastolic (right) velocities measured by MR PVM and TDI. Velocities measured by MR were consistently higher than velocities measured by TDI, with the difference being significant everywhere except the septal wall during systole and the lateral wall during diastole in patients. In the figure, * denotes p<0.001, and + denotes p<0.005.

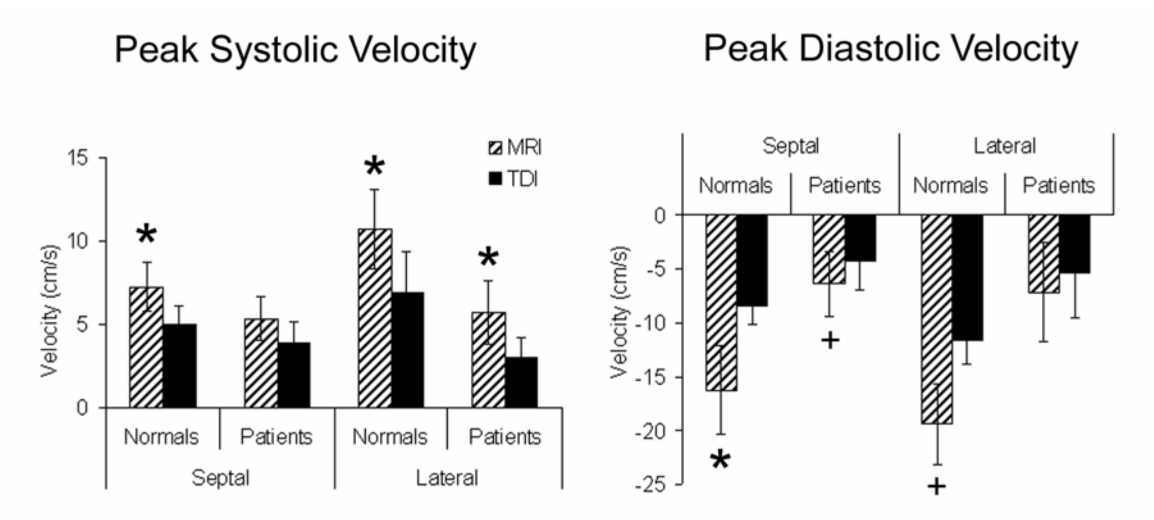

***Figure 5.3**: Peak velocities measured by MR PVM and TDI.*

Bland-Altman analysis found a large bias in the value of peak velocity measured by MR and TDI: MR peak velocity measured an average of 4.35 +/- 3.7 cm/s larger in magnitude than peak velocity measured by TDI. Figure 5.4 shows the Bland-Altman plot of the absolute value of peak velocities and clearly illustrates that peak velocities were consistently higher when measured by MR. The solid line denotes the average difference between MR and TDI, and the dashed lines denote +/- 2 standard deviations.

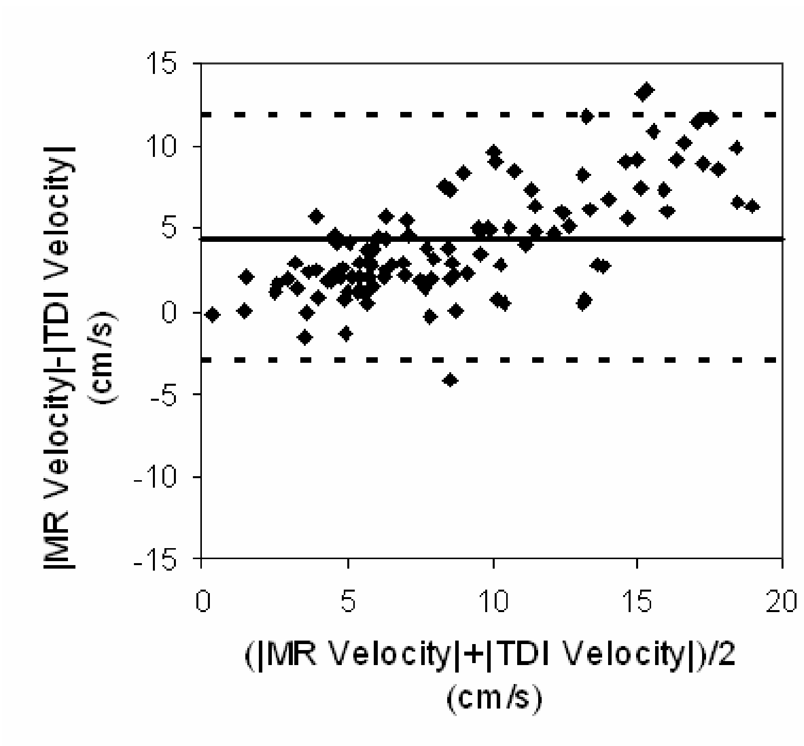

Figure 5.4: *Bland-Altman plot showing the bias in peak velocity measurements*

Comparison of time-to-peak velocity measurements

Time-to-peak systolic and diastolic velocities measured by MR and TDI correlated strongly. The correlation coefficient for time-to-peak velocity was 0.97, with the equation of the linear regression line being TDI=0.96*MR+0.02. Although the magnitude of peak velocity measurements by MR PVM exceeded the TDI measure of velocity, no such bias was observed in measurements of time-to-peak velocity by MR or TDI in either normal subjects or dyssynchrony patients. Figure 5.5 show the time-to-peak systolic (left) and diastolic velocity (right) measured by MR PVM and TDI. Note that there were no significant differences in time-to-peak velocities measured by MR PVM and TDI. Table 5.2 gives the numerical values.

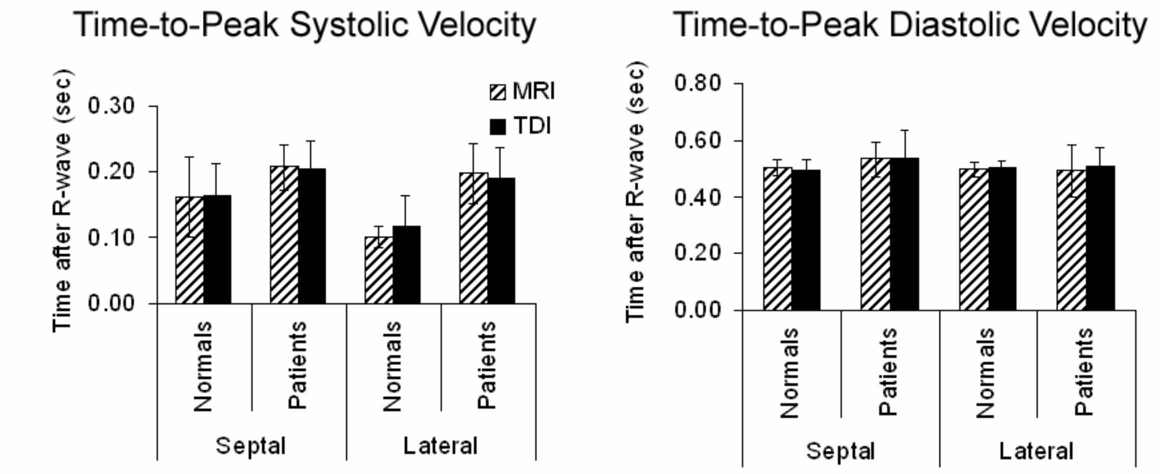

***Figure 5.5**: Time-to-peak velocities measured by MR PVM & TDI.*

Table 5.2: Time- to-Peak Velocities Measured by MR PVM and TDI

	Time-to-peak Systolic Velocity (sec)				**Time-to-peak Diastolic Velocity (sec)**			
	Septal Wall		Lateral Wall		Septal Wall		Lateral Wall	
	Normals	Patients	Normals	Patients	Normals	Patients	Normals	Patients
MR	0.16+/-0.06	0.20 +/-0.04	0.10+/-0.02	0.18+/-0.05	0.50 +/-.03	0.53+/-0.06	0.50+/-0.03	0.49+/-0.09
TDI	0.16+/-0.05	0.21+/-0.05	0.12+/-0.04	0.18+/-0.04	0.50+/-0.03	0.54+/-0.10	0.51+/-0.02	0.51+/-0.07
	P=NS	P=NS	P=NS	P=NS	P=NS	P=NS	P=NS	P=NS

A Bland-Altman analysis of the time-to-peak velocity showed good agreement between the time-to-peak velocity measured by MR and TDI. The measurement contains little bias, with a mean difference between the two techniques of 5 msec (+/- 44msec). The Bland-Altman plot is shown in Figure 5.6. The solid line denotes the average difference, and the dashed lines denote +/- 2 standard deviations.

Excellent correlation was observed between dyssynchrony measured by MR and TDI. The equation of linear regression was TDI=0.949*MR, with a correlation coefficient of 0.91. Table 5.3 lists the value of dyssynchrony measured by MR and TDI for each of the ten heart failure patients who participated in this study. Average dyssynchrony measured by MR was 56+/-24msec, while average dyssynchrony measured by TDI was 54+/-34msec. The average difference between dyssynchrony measured by MR and TDI was 24+/-13msec.

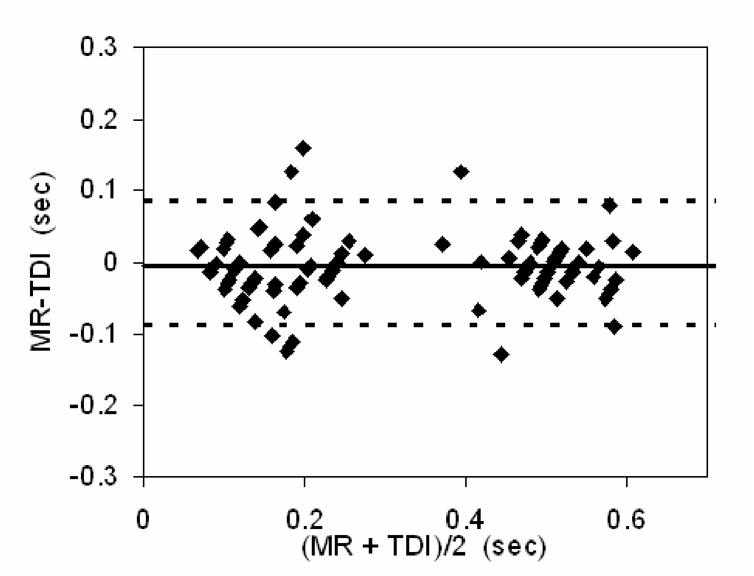

Figure 5.6*: Bland-Altman plot of time-to-peak velocity.*

Table 5.3*: Dyssynchrony Values by MR and TDI for Individual Patients*

Patient #	**NYHA class**	**Dyssynchrony by MR**	**Dyssynchrony by TDI**	**Absolute Difference |MR-TDI|**
1	III	40	60	20
2	III	40	30	10
3	II-III	105	120	15
4	III	72	60	12
5	III	72	30	42
6	III	36	60	24
7	III	74	60	14
8	III	30	0	30
9	III	40	90	50
10	III-IV	52	30	22
Mean+/-Std	**III**	**56+/-24**	**54+/-34**	**24+/-13**

Reproducibility

The coefficient of variability between repeated measurements of peak velocity was 11.0 % for MR and 13.1 % for TDI, p=NS. A Bland-Altman analysis showed a mean difference in peak velocity between repeated TDI measurements of 0.12+/-1.9 cm/s and a mean difference in peak velocity for repeated MR measurements of -0.51+/-2.1 cm/s. No repeated MR measurements fell outside two standard deviations (95% confidence interval) of the mean difference, while only one TDI measurement fell outside two standard deviations of the mean difference. Figure 5.7 shows the Bland-Altman plots illustrating the reproducibility of peak velocity measurements for MR (left) and TDI (right). The solid line denotes the average difference, and the dashed lines denote +/- 2 standard deviations.

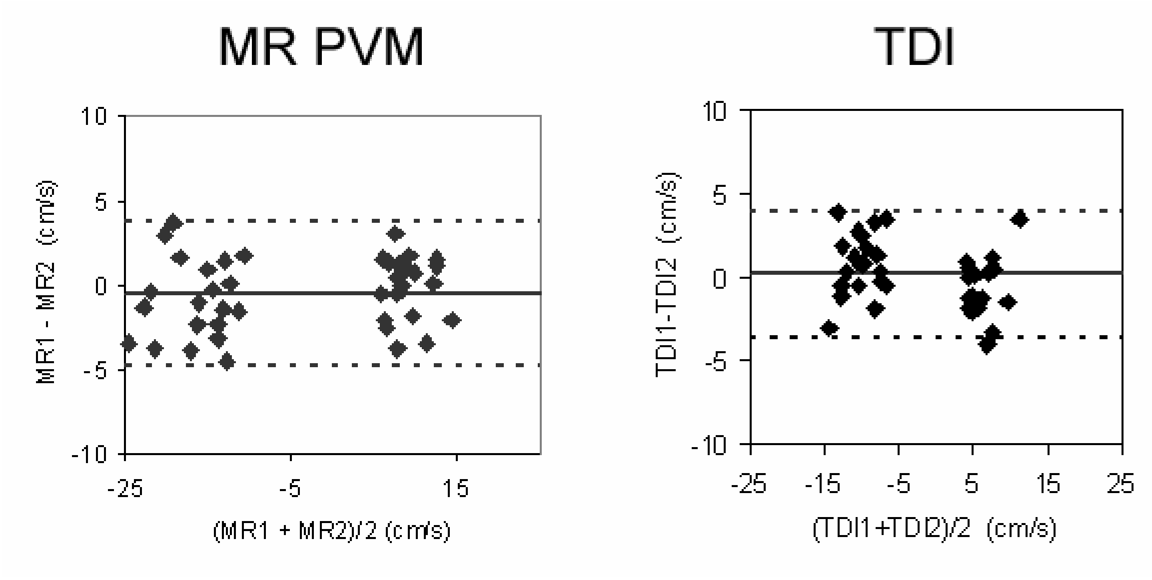

Figure 5.7: *Reproducibility of peak velocity measurements*

The coefficient of variation for repeated time-to-peak velocity measurements was 5.7% by MR and 9.1% by TDI, p=NS. A Bland-Altman analysis of repeated MR measurements of time-to-peak velocity showed a mean difference closer to zero than did the mean difference of repeated TDI measurements of time-to-peak velocity (-3.3msec for MR vs. 6.7 msec for TDI). Figure 5.8 shows the Bland-Altman plots illustrating the reproducibility for measuring the time-to-peak velocities by MR (left) and TDI (right). The solid line denotes the average difference, and the dashed lines denote +/- 2 standard deviations. The standard deviation was lower for repeated MR measurements than for repeated TDI measurements (27.1 msec for MR vs. 37.5 msec for TDI). Two repeated MR measurements fell outside two standard deviations (95% confidence interval) of the mean difference, while three TDI measurements fell outside two standard deviations of the mean difference. Average percent difference in heart rate between repeated examinations was 4.6% for TDI and 5.1% for MR.

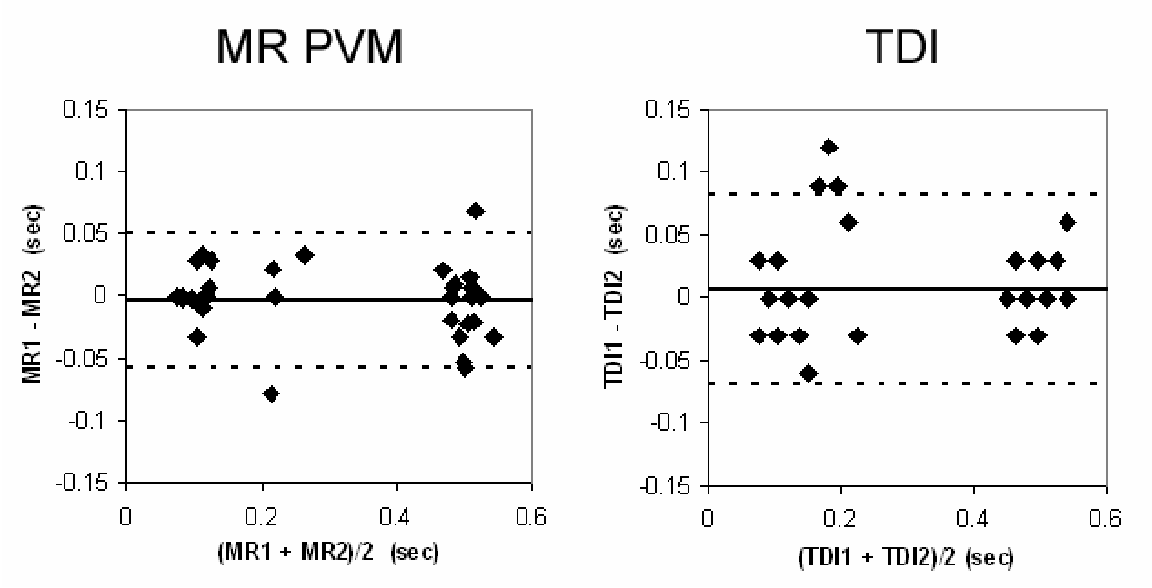

Figure 5.8: *Reproducibility of time-to-peak velocity measurements*

Discussion

This study presents an *in vivo* comparison of MR and TDI in normal subjects and patients with left ventricular dysfunction and dyssynchrony. The ability to measure tissue velocity and time-to-peak velocity with MR provides an opportunity to validate measurements made by TDI, as well as an alternative technique to measure dyssynchrony.

Measurements of peak velocities by MR and TDI correlated strongly, although the magnitude of peak velocities measured by MR consistently exceeded those measured by TDI. Possible explanations for this discrepancy include foreshortening during acquisition of the TDI data or phase errors in the MR data, although we attempted to correct for both sources of such errors. The slightly lower values of the correlation coefficient observed in the dyssynchrony patients can be attributed to the lower tissue velocities observed in these patients, as lower velocity values will produce lower r-values when a correlation is computed.

Excellent correlation was observed between MR PVM and TDI in measuring the time-to-peak velocity in both normal volunteers and dyssynchrony patients. Furthermore, MR PVM and TDI agreed in measuring the time-to-peak velocity without bias. This important finding supports the use of velocity measurements to identify dyssynchrony and predict response to CRT[29,85]. Both MR and TDI showed good reproducibility for measuring the time-to-peak systolic and diastolic velocity, with the coefficient of variation slightly lower for MR than TDI (5.7 vs. 9.1%, p=NS). The Bland-Altman analysis showed a slightly lower mean difference and standard deviation for MR PVM than TDI, suggesting that reproducibility of MR in measuring time-to-peak velocity slightly exceeds that of TDI, but the difference was not statistically significant. Time-to-peak systolic velocity is a highly reproducible TDI parameter, and our observations suggest that the reproducibility of MRI in measuring the time-to-peak velocity at least equals that of TDI.

Previous Validations of MR PVM and TDI

Although each technique has previously undergone *in vitro* validation or limited comparison to other imaging modalities, little data exists to support the validity of each measurement in patients with left ventricular conduction abnormalities and controls. Motion phantoms have previously verified the accuracy of TDI with a strong correlation (r=0.99) between measured and true velocity[153,154]. However, the validity of TDI for measuring velocity and time-to-peak velocity in patients with conduction system disease has gained wide acceptance without validation by other velocity imaging techniques. MR PVM has been shown to accurately and reproducibly measure blood velocity in imaging phantoms (errors <1.6% from true)[138-140]. Coronary flow velocity by Doppler flow wire correlates well with MR measurements of blood velocity (r=0.913), and cine MR and MR PVM agree in the determination of regurgitant fraction and volume in patients with mitral regurgitation[139].

Measurements of Dyssynchrony

Initial clinical data have highlighted the potential for using time-to-peak velocity as a measure of cardiac dyssynchrony. A standard deviation of time-to-peak systolic velocity >34 msec across 12 regions in the left ventricle (the "dyssynchrony index") predicted response to CRT with a sensitivity of 82% and specificity of 87%[85]. Our prospective evaluation of time-to-peak velocity across the left ventricle by TDI supports its role as a predictor of clinical and echocardiographic response to CRT[76]. The limitations imposed by anatomic imaging windows, dependence on sonographer skill, and interpreter experience on TDI underscores the need for another imaging technique to provide tissue velocity information. Cardiac MR eliminates the limitations imposed by imaging windows and reduces dependence on sonographer skill. The correlation between MR ant TDI techniques reinforces the value of each method.

Comparison to previously published data

Our results are consistent with the two previous studies which have compared myocardial tissue velocities measured by MR PVM and TDI *in vivo*. Jung et al., 2004 compared *radial* myocardial velocity measured by MR PVM and TDI in a single region of interest in the posterior wall of 29 healthy subjects, and reported a correlation coefficient of R=0.97 between MR and TDI[155]. Paelinck et al., 2005 compared tissue velocity between MR and TDI at a single location in the septal wall of patients with hypertensive heart disease and reported a correlation coefficient of R=0.89[156]. We report a correlation coefficient of R=0.86 between MR and TDI for values acquired in both normal controls and dyssynchrony patients. This value is comparable to Paelinck et al, but slightly lower than Jung et al., possibly because Jung et al. only looked at normal controls.

Improvements in MR Technique

The MR technique employed in this study presents several improvements over the previous MR methods used to map velocity of wall motion[48,53,147,155,157]. Previous PVM studies exclusively used breath-holding to compensate for respiratory motion, resulting in scans with relatively low spatial and temporal resolution. Furthermore, the breathhold technique requires acquisition of velocity data for each direction in separate breathholds, producing image registration errors if the patient fails to hold breathing in the same anatomic point. The breath-hold technique creates problems during imaging of many heart failure patients who cannot hold breathing for prolonged periods of time. Other studies have no respiratory compensation which can result in artifacts from breathing motion. The technique used in this study included navigator-echo gating to compensate for respiratory motion. Navigator-echo gating produces scans with high spatial and temporal resolution and velocity images with proper registration for each velocity direction.

Study Limitations

This analysis has certain limitations. The small sample size may be responsible for failure of the difference in MR PVM and TDI reproducibility values to reach statistical significance. The true velocity of the myocardial wall is not known, and therefore it cannot be concluded whether MR or TDI accurately measured myocardial wall velocity. TDI depends highly on the angle of the transducer, with the chance that foreshortening of the image may underestimate the observed velocities. Phase errors during acquisition can affect MR PVM and overestimate true velocity. Performing the MR and TDI examinations at different times opens the possibility of physiological changes between the two examinations. We attempted to minimize such differences by performing the TDI immediately after the MR. MR acquires velocity data much slower than TDI and averages velocity data over many cardiac cycles. Both MR and TDI have inherent limitations to imaging the mechanical delay of the myocardial wall in dyssynchrony and assessing the effect of therapy. TDI cannot measure 3-dimensional velocities, and currently the safety of MR on patients with implanted devices remains undetermined. Also, neither MR nor TDI perform true tissue tracking, and since the location of the ROI for velocity measurement remains fixed, the region of myocardial tissue sampled varies throughout the cardiac cycle.

Conclusions

MR PVM can measure time-to-peak myocardial tissue velocity in patients with left ventricular dysfunction and cardiac conduction system disease. The first *in vivo* comparison of MR PVM and TDI myocardial tissue velocities in normal subjects and dyssynchrony patients demonstrates that MR and TDI correlate strongly in measuring myocardial tissue velocity and time-to-peak velocity in both normal subjects and patients with dyssynchrony. MR PVM and TDI have comparable reproducibility for measuring both peak velocity and time-to-peak velocity. MR may provide an alternative method for detecting cardiac dyssynchrony.

CHAPTER 6

AIM 4: DEVELOPMENT OF DATABASES DESCRIBING THE NORMAL MYOCARDIAL CONTRACTION PATTERN

Introduction

Myocardial contraction is a complex, three-dimensional movement involving longitudinal and radial shortening, torsion and shear. Understanding myocardial motion is important because the myocardial contraction and relaxation pattern is a direct measure of the function and viability of the heart[138]. Multiple studies have shown that alterations of this contraction pattern are predictive of cardiac disease and transplant rejection[49,158,159]. However, before changes to this motion pattern can be identified, normal myocardial motion needs to be quantitatively described.

The purpose of this study was 1) to develop a database describing the normal myocardial contraction and relaxation patterns (including velocity and time-to-peak velocity) and 2) to compare the contraction patterns in heart failure patients to the normal database to determine how myocardial motion is altered by dyssynchrony.

Methods

Myocardial Tissue Velocity Data and Tracking In-vivo

Myocardial velocity data was acquired and processed as described in Chapter 3. Briefly, three-directional myocardial tissue velocities were acquired at three myocardial slices (apex, mid, base) using the finalized MR PVM protocol, which consisted of a segmented, ECG and navigator echo gated, phase contrast sequence. Background phase errors were removed after image acquisition using a custom-developed Matlab program.

Myocardial tissue tracking was performed in all acquired datasets using the tissue tracking algorithm also described in Chapter 3. Although velocity data for each study participant was acquired at three myocardial locations (basal, mid, and apical slices), the slices were separated by 10mm gaps. Therefore, tissue tracking was performed independently for each slice, and longitudinal motion was dictated by velocity within the acquired slice, regardless of how far the particle moved in the thru-plane direction.

Velocity Database from Tracked Myocardial Data

10 normal volunteers without any history or evidence of cardiovascular disease were included in the database. Mean age of the volunteers was 27.2+/-4.9 years, and 8 were male.

A normal database describing several different myocardial motion parameters was developed. Because the goal of this project was to follow individual myocardial segments throughout the cardiac cycle, the database was constructed using velocity computed by the tracking algorithm, not the velocity data as acquired directly with the MR PVM scan.

Velocity values within the myocardium were averaged into the 16 AHA standard segments; averaging condensed the velocity data into three velocity curves (Vr, Vc, and Vz) in each of the 16 AHA myocardial segments. In each segment, peak systolic velocity, peak diastolic velocity, time-to-peak systolic velocity, and time-to-peak diastolic velocity were measured. A database giving the mean +/- two standard deviations of the normal value was constructed for each of these parameters.

The process of searching for peak systolic and diastolic velocities was automated in Matlab. Systole was defined as the period of the cardiac cycle between aortic valve opening and closing, while diastole was considered to be the portion of the cardiac cycle after aortic valve closing. Aortic valve opening and closing times were determined from cine LV outflow tract images. Within the systolic and diastolic portions of the myocardial velocity curve, the algorithm searched for the largest positive and negative peak values, respectively. Furthermore, the restriction was imposed that peak systolic velocities had to be positive, while peak diastolic velocities had to be negative (for circumferential velocity within the apical slice, this requirement was reversed, and systolic velocity needed to be negative and diastolic velocities positive). Segments in which the automatically-detected peak velocity values did not meet these criteria were excluded from the analysis.

Magnitudes and timing of peak velocities between velocity directions, systolic and diastolic peaks, and the three myocardial slices were compared using a Student's t-test with p-values <0.05 considered statistically significant.

Dyssynchrony Measurements

To assess intra-ventricular dyssynchrony, the magnitudes of peak velocities and the timing of peak velocities in the septal and lateral wall were compared. The septal wall was defined as the average of AHA segments 2 and 3 in the basal slice, segments 8 and 9 in the mid slice, and segment 14 in the apical slice. The lateral wall was defined as the average of AHA segments 5 and 6 in the basal slice, segments 11 and 12 in the mid slice, and segment 16 in the apical slice. Septal and lateral value were compared using a Student's t-test with p-values <0.05 considered statistically significant.

Dyssynchrony was measured using the septal-to-lateral wall motion delay (SLD) and the standard deviation of time-to-peak systolic velocity between the 12 mid and basal segments (T_{SD-12}). The septal-to-lateral wall motion delay (SLD) was computed as the absolute value of the difference between time-to-peak systolic velocity in the septal and lateral walls[151]. The standard deviation of time to peak systolic velocity within the 12 basal and mid segments (T_{SD-12}) was also computed for each normal volunteer[160].

Both SLD and T_{SD-12} were computed for each normal volunteer and each dyssynchrony patient. The averages of the normal and patient values were compared using a two-tailed un-paired Student's t-test with p-value <0.05 considered statistically significant.

Comparison of Tracked and Non-tracked Databases

The effect of using tracked and non-tracked velocity data in the construction of the normal databases was examined. Databases constructed using velocity data that had been output from the tracking algorithm (tracked data) were compared to databases constructed using velocity data directly acquired by the MR PVM velocity scan (non-tracked data).

Values of each of the original measured motion parameters (peak systolic velocity, peak diastolic velocity, time-to-peak systolic velocity, and time-to-peak diastolic velocity) from the tracked and the non-tracked databases were compared using Bland-Altman analysis.

Comparison of Dyssynchrony Patients to the Normal Database

Eight patients that had been referred to Emory University Hospital for cardiac resynchronization therapy underwent a cardiac MRI examination that included a MR PVM scan of myocardial tissue velocity prior to CRT device implantation. Patients had ECG evidence of an intra-ventricular conduction delay (QRS > 120 msec), reduced cardiac function (LVEF< 40%), and all were in NYHA class III heart failure.

Images from the MR PVM scans were processed as in the same way as images for the normal database. Background phase correction was performed, velocities were converted into radial, longitudinal, and circumferential velocities, motion tracking was performed, and the myocardium was registered to the standardized template as described in Chapter 3.

Motion parameters (peak systolic velocity, peak diastolic velocity, time-to-peak systolic velocity and time-to-peak diastolic velocity) were computed for each of the 16 myocardial segments, and patient values were compared to the values in the normal database. Values more than two standard deviations from the normal mean were considered "abnormal" and were designated as potential markers of cardiac dyssynchrony.

Individual Patient Data

One overall goal of creating a normal database that quantitatively describes the myocardial contraction pattern was to allow individual patients to be compared to the statistical mean value. Ideally, the normal database could be used to identify the location of regional dyssynchrony within the myocardium.

To illustrate the feasibility of this approach, the timing of systolic contraction in two heart failures patients prior to CRT was compared to the normal database. Both patients were in class III NYHA heart failure, had LBBB and QRS duration >150msec;

these criteria make the likelihood of dyssynchrony in these patients very high. Therefore, these patients can be considered a "positive control" for the presence of dyssynchrony.

The patient value in each of the 16 AHA myocardial segments was compared to the normal database value in that segment. Patient values in each segment were labeled as normal (for values within two standard deviations of the mean), early (time-to-peak velocity earlier than two standard deviations before the normal mean), or late (time-to-peak velocity later than two standard deviations before the normal mean).

Different Patient Outcomes with Tracked or Non-tracked Databases

To test whether the choice of database (tracked or non-tracked) had an affect on characterization of patient data, patient values were compared to both the tracked and the non-tracked databases. (Tracked patient data was compared to the normal tracked database, and non-tracked patient data was compared to the normal non-tracked database). Segments were labeled as normal (for values within two standard deviations of the mean), low/early (velocity values below two standard deviations of the mean or time-to-peak velocity earlier than two standard deviations before the normal mean), or high/late (velocity values above two standard deviations of the mean or time-to-peak velocity later than two standard deviations before the normal mean). Segments that were characterized differently by the tracked and non-tracked databases were flagged.

Results

Myocardial Tissue Velocity Data and Tracking In-vivo

Velocity acquisition and tissue tracking was successfully carried out in all normal volunteers and heart failure patients. Figure 6.1 shows an example of tissue tracking results from one of the normal volunteers. Trajectories from adjacent pixels follow similar trajectories, and the trajectories of individual pixels do not leave the myocardium.

Longitudinal displacement was a function of the imaging slice, decreasing with distance toward the apex (average longitudinal displacement =7.4+/-2.8mm in basal slice, 5.8=/-2.8mm in mid slice, and 3.13+/-1.6mm in apical slice).

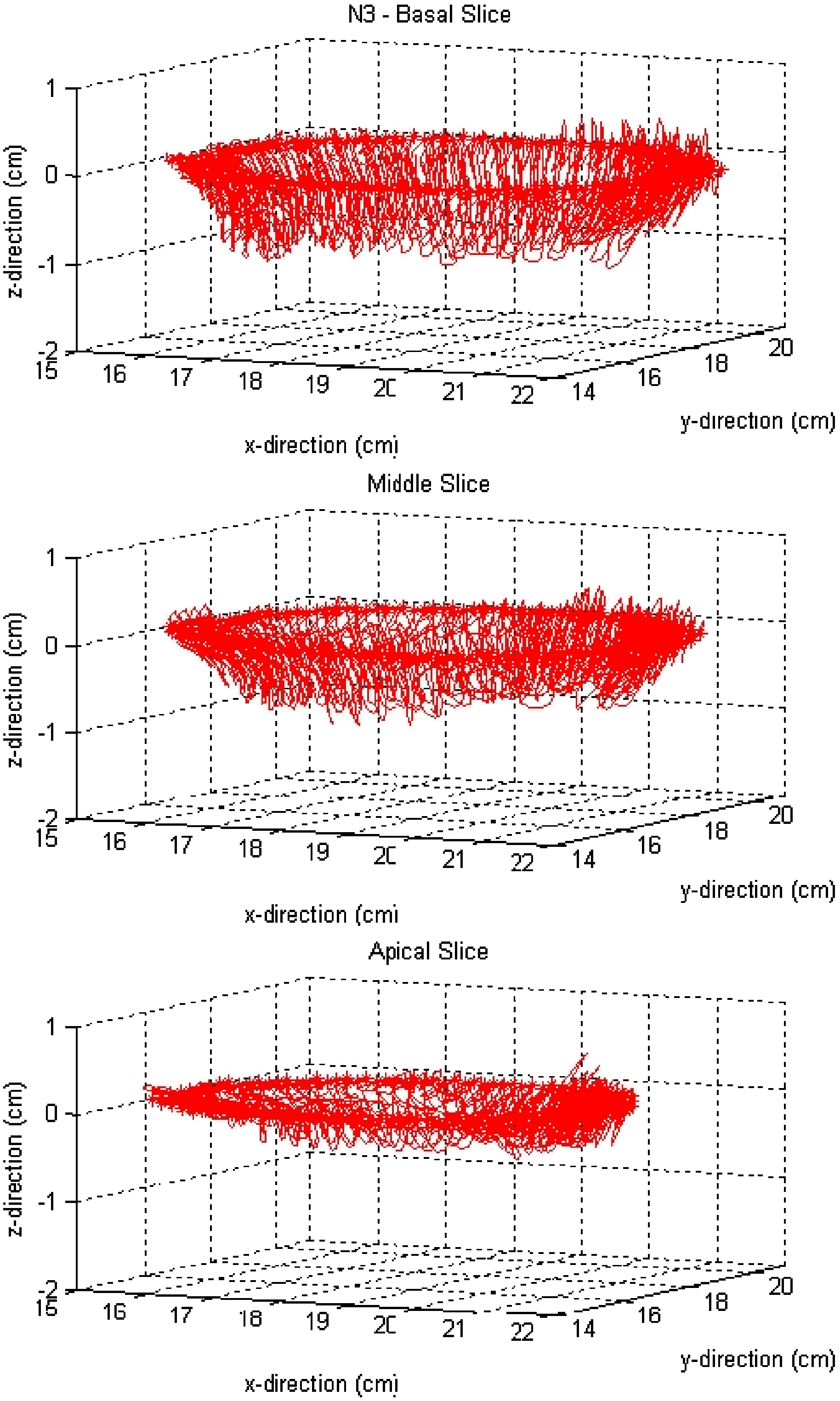

***Figure 6.1**: In-vivo tissue tracking example*

Velocity Database from Tracked Myocardial Data

The database for each of the four motion parameters (peak systolic velocity, peak diastolic velocity, time-to-peak systolic velocity and time-to-peak diastolic velocity) was composed of 160 myocardial segments (16 segments from each of 10 normal volunteers).

In three myocardial regions, the measurements of peak systolic circumferential velocity did not meet the pre-determined criteria (positive peak values during systole, negative peak values during diastole, peak systolic time between AVo and AVc, peak diastolic time after AVc) and were not included in the database. These segments were from two different normal volunteers and all three were located in the lateral wall of the mid ventricular slice. In the longitudinal direction, one apical septal segment did not meet criteria for peak systolic velocity and was not included in the database. It is possible that the velocity measurements in these segments were corrupted by a noise susceptibility artifact often that is often observed within the lateral myocardial wall.

Peak Velocities

For the radial and longitudinal direction, peak velocities were positive during systole and negative during diastole. In the circumferential direction, however, the sign of the velocity peak depended on location within the myocardium. Peak circumferential velocities during systole were positive (clockwise rotation) in the basal slice and negative (counter-clockwise rotation) in the apical slice. During diastole, negative (counterclockwise) motion was observed in the basal slice and positive (clockwise) motion was observed in the apical slice.

Table 6.1 lists the mean and standard deviation of the peak velocity measured during systole and diastole in each of the 16 AHA myocardial segments. Segments 1-6 are located in the basal slice, segments 7-12 are in the mid slice, and segments 13-16 are located in the apical slice. (The convention was to define radial velocity as positive for motion toward the center of the LV blood pool, circumferential velocity as positive for clockwise rotation when viewed from the apex, and longitudinal velocity as positive for motion toward the apex).

Table 6.1: Peak velocity database from tracked data

AHA **Segment #**		**Peak Systolic Velocity (cm/s)**			**Peak Diastolic Velocity (cm/s)**		
		Vr	**Vc**	**Vz**	**Vr**	**Vc**	**Vz**
Basal Slice	1	4.2+/-1.1	1.5+/-0.7	3.2+/-1.5	-5.1+/-1.5	-1.7+/-0.9	-7.7+/-2.1
	2	2.6+/-1.2	1.9+/-0.8	3.2+/-0.5	-3.0+/-1.3	-1.7+/-1.2	-6.7+/-2.0
	3	2.1+/-0.7	2.9+/-1.0	3.8+/-0.7	-4.1+/-1.5	-2.2+/-1.0	-7.0+/-2.0
	4	2.9+/-1.3	2.7+/-1.0	5.6+/-2.2	-4.6+/-1.3	-2.7+/-1.0	-7.9+/-2.7
	5	3.3+/-1.3	2.3+/-1.1	6.7+/-2.2	-4.9+/-2.0	-2.1+/-0.8	-10.5+/-3.5
	6	3.5+/-0.8	2.2+/-0.9	6.2+/-1.7	-5.9+/-1.5	-2.6+/-0.8	-10.5+/-2.4
Middle Slice	7	2.9+/-0.7	1.3+/-0.6	3.2+/-1.6	-5.1+/-1.3	-1.9+/-0.9	-5.2+/-1.6
	8	2.2+/-0.6	2.0+/-0.6	2.7+/-1.4	-4.6+/-1.6	-1.4+/-0.7	-5.0+/-1.6
	9	2.4+/-0.7	1.9+/-0.9	3.3+/-1.4	-4.3+/-1.4	-1.6+/-0.4	-4.2+/-2.2
	10	3.1+/-0.8	1.2+/-0.5	5.2+/-1.6	-4.9+/-1.2	-1.9+/-1.0	-6.6+/-2.2
	11	2.9+/-1.2	1.1+/-0.4	6.1+/-1.4	-5.9+/-1.5	-1.8+/-1.0	-8.6+/-2.3
	12	3.8+/-1.2	1.1+/-0.8	4.9+/-1.6	-5.8+/-2.1	-2.0+/-1.1	-7.1+/-1.8
Apical Slice	13	2.0+/-1.0	-4.5+/-1.2	2.4+/-0.8	-4.5+/-1.0	3.1+/-0.6	-3.0+/-1.6
	14	2.1+/-0.9	-2.7+/-1.3	1.4+/-0.8	-3.1+/-1.4	1.4+/-0.4	-1.9+/-1.3
	15	3.4+/-1.2	-1.7+/-1.5	3.2+/-1.1	-3.7+/-1.2	2.6+/-1.0	-2.0+/-1.1
	16	3.7+/-1.6	-2.8+/-1.2	4.6+/-1.1	-5.2+/-1.6	3.1+/-1.3	-4.4+/-1.5

Throughout the entire LV, the magnitude of peak longitudinal velocities was significantly ($p<0.05$) larger than the magnitude of either peak radial or circumferential velocities, both during systole and diastole, Table 6.2. Peak radial velocities were significantly larger in magnitude than peak circumferential velocities ($p<0.05$), both during systole and diastole.

Within a given slice, the magnitudes of peak radial, circumferential, and longitudinal velocities were all significantly different ($p<0.05$), with the exception of peak radial and longitudinal velocities in the apical slice during systole.

In general, peak diastolic velocities were greater in magnitude than peak systolic velocities. This difference was significant ($p<0.05$) in the radial direction for all three myocardial slices, in the longitudinal direction for the basal and mid slices, and in the circumferential direction for the mid slice. No significant difference was observed between the magnitudes of peak systolic and diastolic velocities in the circumferential direction in either the basal ($p=0.51$) or apical ($p=0.68$) slices, or in the longitudinal direction in the apical slice ($p=0.68$).

The magnitudes of peak radial velocities were not significantly different between the basal, mid, and apical slices. The magnitude of peak circumferential velocity was greatest in the apical slice and smallest in the mid slice. The magnitude of peak longitudinal velocity decreased with distance toward the apex, with the largest velocities observed in the basal slice and the smallest in the apical slice. In the longitudinal direction, the difference in peak velocity magnitudes was significant ($p<0.05$) between all slices, both during systole and diastole. In the circumferential direction, the magnitude of peak velocity was significantly different between all slices during systole ($p<0.05$), but during diastole the apical and basal slices were not significantly different.

***Table 6.2**: Magnitudes of Peak Velocities by imaging slice*

Peak Systolic Velocity (cm/s)			
	|Vr|	**|Vc|**	**|Vz|**
Basal	3.1+/-1.2	2.3+/-1.0	4.8+/-2.1
Mid	2.9+/-1.0	1.5+/-0.7	4.2+/-2.1
Apical	2.8+/-1.4	2.9+/-1.6	2.9+/-1.5
Entire LV	2.9+/-1.2	2.1+/-1.3	4.1+/-2.0
Peak Diastolic Velocity (cm/s)			
Basal	4.6+/-1.7	2.2+/-1.0	8.4+/-2.9
Mid	5.1+/-1.6	1.8+/-0.9	6.1+/-2.4
Apical	4.1+/-1.5	2.6+/-1.1	2.8+/-1.7
Entire LV	4.7+/-1.6	2.1+/-1.0	6.2+/-3.3

Differences between the septal and lateral walls

Throughout the entire LV, the magnitude of peak velocities observed in the septal wall was lower than the magnitude of peak velocities observed in the lateral wall, Table 6.3. The difference between septal and lateral wall peaks was significant ($p<0.05$) for all slices in the radial and longitudinal directions, both during systole and diastole. Peak circumferential velocities remained fairly constant throughout the entire LV, although a difference between septal and lateral wall velocities was detected in the middle slice during systole and the apical slice during diastole.

Table 6.3: *Magnitudes of Peak Velocities in the Septal and Lateral Walls*

Peak Systolic Velocity (cm/s)				
		Basal	**Mid**	**Apical**
Vr	Septal	2.3+/-1.0	2.3+/-0.6	2.1+/-0.9
	Lateral	3.4+/-1.1	3.3+/-1.3	3.7+/-1.6
	p-value	*p<0.05*	*p<0.05*	*p<0.05*
Vc	Septal	2.4+/-1.0	1.9+/-0.7	2.7+/-1.3
	Lateral	2.2+/-0.9	1.1+/-0.6	2.8+/-1.2
	p-value	*p=0.54*	*p<0.05*	*p=0.84*
Vz	Septal	3.5+/-0.7	3.0+/-1.4	1.4+/-0.8
	Lateral	6.4+/-2.0	5.5+/-1.6	4.6+/-1.1
	p-value	*p<0.05*	*p<0.05*	*p<0.05*
Peak Diastolic Velocity (cm/s)				
Vr	Septal	3.6+/-1.5	4.4+/-1.4	3.1+/-1.4
	Lateral	5.4+/-1.8	5.9+/-1.7	5.2+/-1.6
	p-value	*p<0.05*	*p<0.05*	*p<0.05*
Vc	Septal	1.9+/-1.1	1.5+/-0.6	1.4+/-0.4
	Lateral	2.3+/-0.8	1.9+/-1.0	3.1+/-1.3
	p-value	*p=0.19*	*p=0.14*	*p<0.05*
Vz	Septal	6.9+/-1.9	4.6+/-1.9	1.9+/-1.3
	Lateral	10.5+/-2.9	7.9+/-2.2	4.4+/-1.5
	p-value	*p<0.05*	*p<0.05*	*p<0.05*

Figure 6.2 displays Bulls-Eye plots of peak velocities in each of the 16 myocardial segments, both during systole and diastole. The longitudinal apex-to-base gradient and the difference in the magnitude of peak velocity between the septal and lateral walls are clearly visible. Also easy to identify is the opposite direction of rotation between the basal and apical slices.

Figure 6.3 displays the information presented in Figure 6.2 a slightly different way. Peak velocity is plotted versus myocardial segment, allowing width of the mean +/- 2 standard deviations of the normal value to be shown. This figure shows that the variability in the magnitude of peak velocities within the normal volunteers was fairly small. The largest inter-normal variation was observed for peak longitudinal velocity during diastole, the parameter with the largest velocity magnitude.

In Figure 6.3 it is also possible to observe the different rotation directions between the apical and basal slices in the circumferential velocity direction as the sharp change of the circumferential velocity curves at segment 13. Also in Figure 6.3, the difference in peak longitudinal velocity magnitude between the septal and lateral walls can be observed as an undulation in the longitudinal velocity values, with peak values being lower in myocardial segments 2 and 3 (septal wall, basal slice), higher in segments 5 and 6 (lateral wall, basal slice), lower in segments 8 and 9 (septal wall, middle slice), higher in segments 11 and 12 (lateral wall, middle slice), lower in segment 14 (septal wall, apical slice), and higher in segment 16 (lateral wall, apical slice).

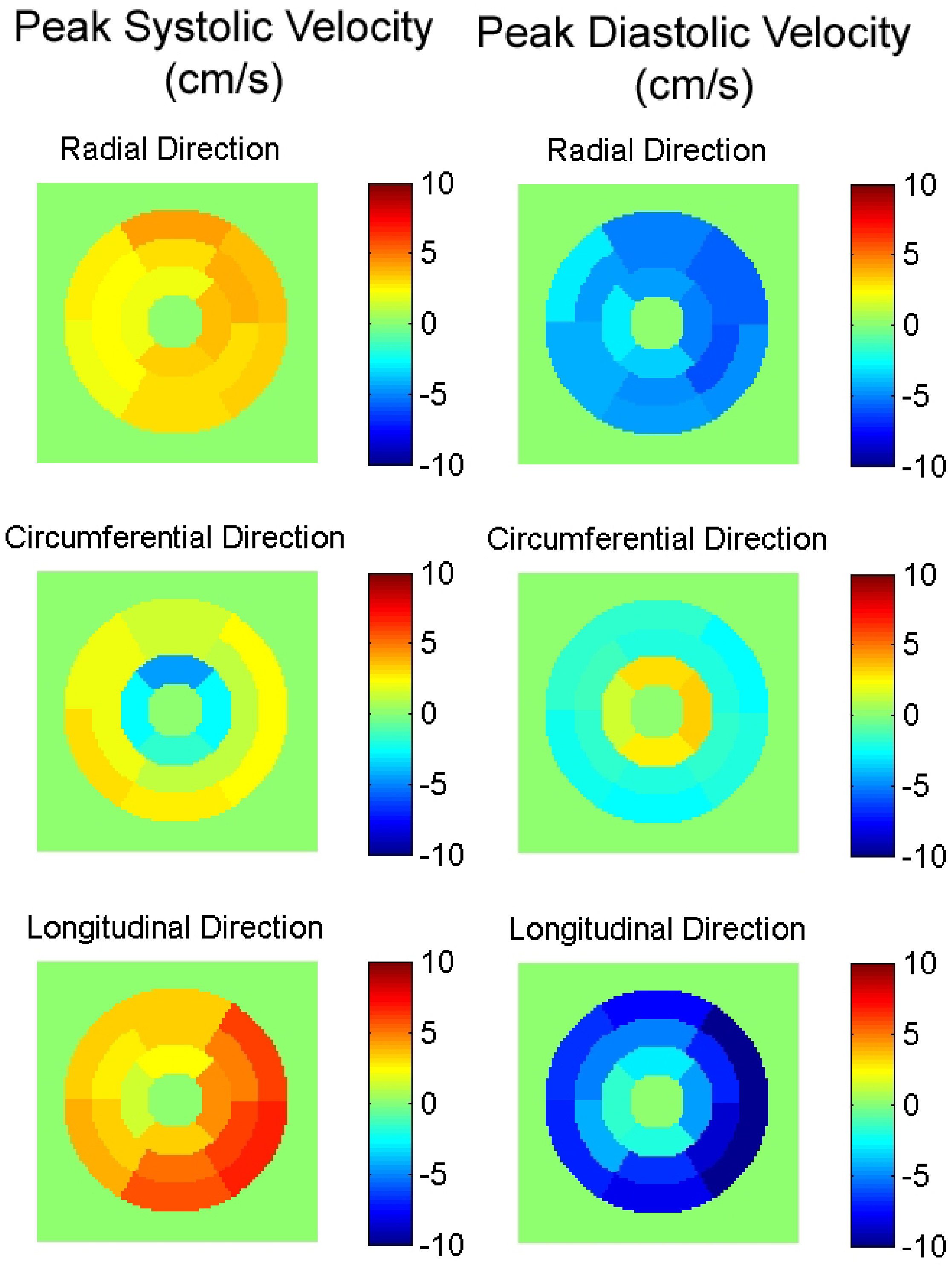

Figure 6.2: Bulls-eye plot of peak velocities during systole and diastole

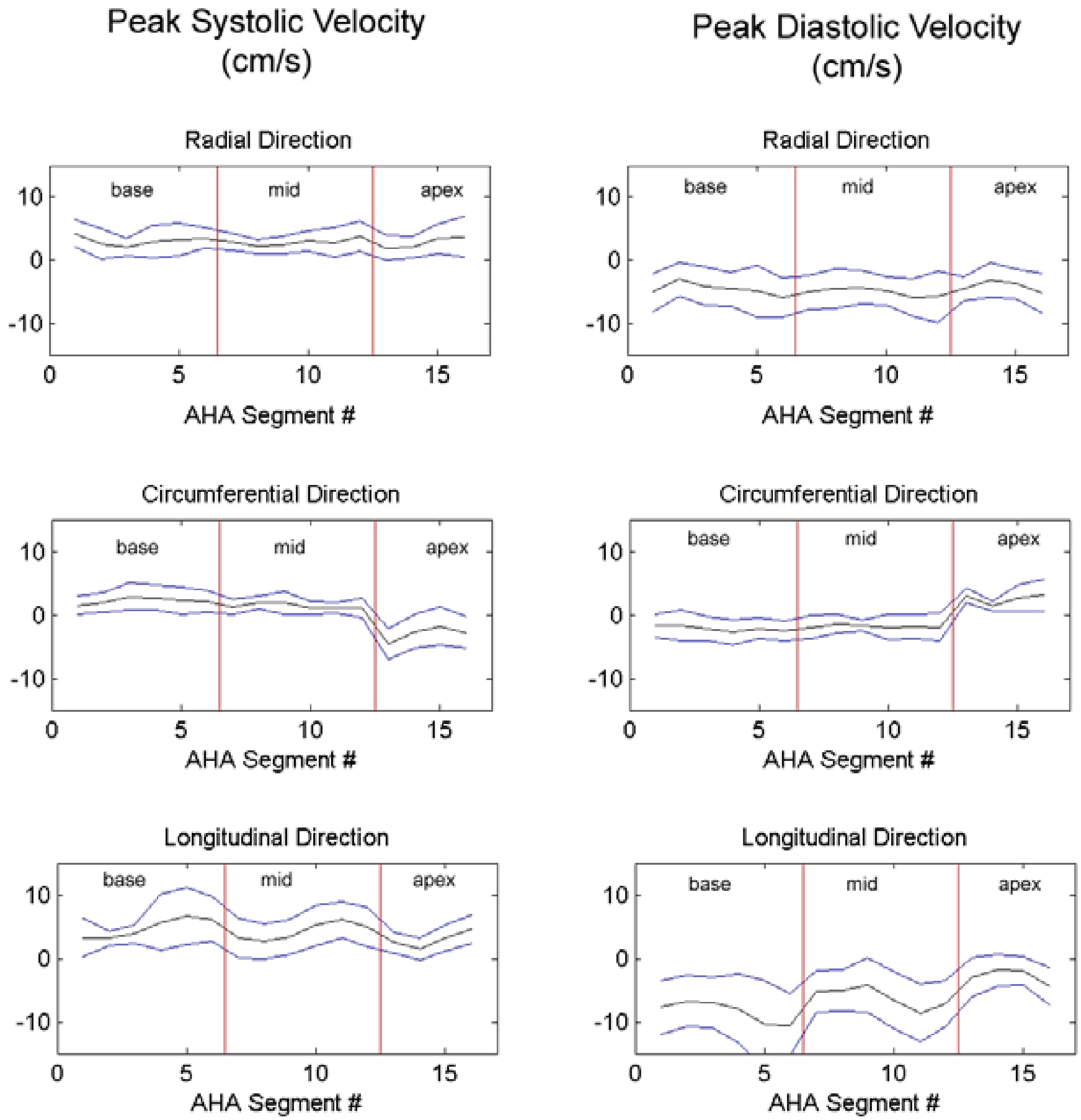

Figure 6.3: Mean +/-2std of peak velocity in tracked database

Time-to-Peak Velocities

Table 6.4 lists the measured values of time-to-peak for systolic and diastolic velocities in each of the 16 AHA myocardial segments. The mean and standard deviation of time-to-peak radial, circumferential, and longitudinal velocity in each AHA myocardial segment is given. Recall that measurements of time are given as msec from the detection of the R-wave in the QRS complex.

During systole, small differences in the timing of peak velocities were observed between the three velocity directions, Table 6.5. In general, peak longitudinal velocity was detected first, followed by peak radial velocity and then peak circumferential velocity. This pattern was observed in both the basal and mid slices, with the timing difference between all velocity directions being significant ($p<0.05$). In the apical slice, peak systolic longitudinal velocity was also detected first, but the order of radial and circumferential velocities was reversed with peak circumferential velocity detected before peak radial velocity. In the apical slice, the difference in timing between the longitudinal and circumferential velocity directions was not significant ($p=0.21$).

During diastole, no significant differences in the values of *time-to-peak* velocities were detected between radial, circumferential, or longitudinal velocities in any of the three myocardial slices examined. In other words, peak diastolic relaxation velocities were detected as occurring uniformly throughout the entire LV for all three directions of velocity.

Table 6.4: Peak velocity database from tracked data

AHA Segment #		**Time-to-Peak Systolic Velocity (msec after R-wave detection)**			**Time-to-Peak Diastolic Velocity (msec after R-wave detection)**		
		Vr	**Vc**	**Vz**	**Vr**	**Vc**	**Vz**
Basal Slice	1	105.3+/- 17.7	169.6+/- 43.0	143.9+/- 57.6	505.8+/- 47.4	534.5+/- 106.5	511.1+/- 29.6
	2	105.4+/- 35.1	189.8+/- 61.8	146.6+/- 51.9	511.2+/- 97.9	562.4+/- 91.1	516.2+/- 37.2
	3	176.9+/- 49.3	187.5+/- 29.9	138.8+/- 51.4	554.9+/- 37.8	495.9+/- 80.1	503.3+/- 34.1
	4	169.3+/- 43.1	200.3+/- 35.0	97.6+/- 17.8	493.2+/- 36.2	482.6+/- 119.5	513.6+/- 44.6
	5	141.2+/- 29.0	187.5+/- 60.6	95.0+/- 20.8	475.1+/- 34.2	485.9+/- 75.1	503.4+/- 35.0
	6	136.0+/- 27.0	169.5+/- 46.5	97.5+/- 17.4	480.2+/- 35.4	521.1+/- 77.8	511.0+/- 32.8
Middle Slice	7	136.3+/- 41.5	174.8+/- 45.4	116.1+/- 57.0	510.6+/- 64.8	585.3+/- 134.1	518.9+/- 29.2
	8	153.8+/- 52.2	190.0+/- 39.1	125.8+/- 50.3	539.3+/- 43.5	595.5+/- 124.1	516.3+/- 34.1
	9	182.2+/- 30.6	195.2+/- 37.7	113.0+/- 33.6	539.4+/- 33.4	524.0+/- 106.4	508.6+/- 27.9
	10	174.4+/- 44.7	189.7+/- 48.7	95.0+/- 16.9	516.2+/- 39.5	503.4+/- 85.7	511.1+/- 24.6
	11	164.3+/- 53.7	198.1+/- 45.9	92.4+/- 15.9	503.3+/- 36.7	516.3+/- 100.6	518.8+/- 38.7
	12	120.6+/- 26.3	183.4+/- 65.1	95.0+/- 16.9	505.9+/- 37.7	505.9+/- 82.7	508.6+/- 35.8
Apical Slice	13	159.5+/- 65.9	94.9+/- 16.8	92.4+/- 10.6	526.6+/- 32.8	462.2+/- 132.1	495.7+/- 45.2
	14	195.1+/- 24.4	115.4+/- 62.2	147.0+/- 75.7	546.9+/- 46.7	508.4+/- 126.0	506.2+/- 66.6
	15	177.1+/- 31.4	171.6+/- 82.7	87.3+/- 12.1	510.8+/- 57.3	582.4+/- 77.5	526.5+/- 140.9
	16	143.6+/- 71.2	89.9+/- 14.7	89.9+/- 8.0	508.6+/- 37.8	480.1+/- 92.6	510.9+/- 52.8

Table 6.5*: Timing of Peak Velocities by myocardial slice and velocity direction*

Time-to-Peak Systolic Velocity (msec after detection of R-wave)			
	Vr	**Vc**	**Vz**
Basal	139+/-44	184+/-47	120+/-45
Mid	155+/-46	189+/-46	106+/-37
Apical	169+/-54	118+/-61	103+/-43
Entire LV	153+/-49	169+/-58	111+/-42
Time-to-Peak Diastolic Velocity (msec after detection of R-wave)			
Basal	503+/-57	514+/-94	510+/-35
Mid	519+/-45	538+/-109	514+/-31
Apical	523+/-46	508+/-115	510+/-83
Entire LV	514+/-50	522+/-105	511+/-50

Differences between the septal and lateral walls

Peak velocity in the lateral wall was detected slightly earlier than peak velocity in the septal wall in the longitudinal direction during systole and the radial direction during diastole. No other significant differences in timing between the septal and the lateral walls were observed, Table 6.6.

Table 6.6: *Time-to-peak Velocity in the Septal and Lateral Walls*

Time-to-Peak Systolic Velocity **(msec after detection of the R-wave)**				
		Basal Slice	**Mid Slice**	**Apical Slice**
Vr	Septal	141+/-55	168+/-44	195+/-24
	Lateral	139+/-27	142+/-47	144+/-71
	p-value	*p=0.86*	*p=.08*	*p=0.05*
Vc	Septal	189+/-47	193+/-37	115+/-62
	Lateral	178+/-53	191+/-54	90+/-15
	p-value	*p=0.53*	*p=0.93*	*p=0.24*
Vz	Septal	143+/-50	119+/-42	147+/-76
	Lateral	96+/-19	94+/-16	90+/-8
	p-value	*p<0.05*	*p<0.05*	*p=0.05*
Time-to-Peak Diastolic Velocity **(msec after detection of the R-wave)**				
Vr	Septal	533+/-76	539+/-38	547+/-47
	Lateral	478+/-34	505+/-36	509+/-38
	p-value	*p<0.05*	*p<0.05*	*p<0.05*
Vc	Septal	529+/-90	560+/-118	508+/-126
	Lateral	504+/-77	511+/-90	480+/-93
	p-value	*p=0.34*	*p=0.15*	*p=0.57*
Vz	Septal	510+/-35	512+/-31	506+/-67
	Lateral	507+/-33	514+/-37	511+/-53
	p-value	*p=0.82*	*p=0.91*	*p=0.86*

Figure 6.4 displays Bulls-Eye plots of the measured time-to-peak velocity during systole and diastole for the three directions of motion. Note that the measurements of time-to-peak velocity are uniform throughout the entire LV, both during systole and diastole. Also easy to appreciate is the larger variation within the LV for measurements of time-to-peak circumferential velocity.

Figure 6.5 shows the mean +/- 2 standard deviations of the normal value of *time-to-peak* velocity measurements during systole and diastole. The figure clearly illustrates that peak diastolic relaxation velocity was observed uniformly throughout the entire left ventricle, both in the radial and longitudinal directions. It is clearly visible from Figure 6.5 that the standard deviation of time-to-peak velocity measurements was greatest in the circumferential direction.

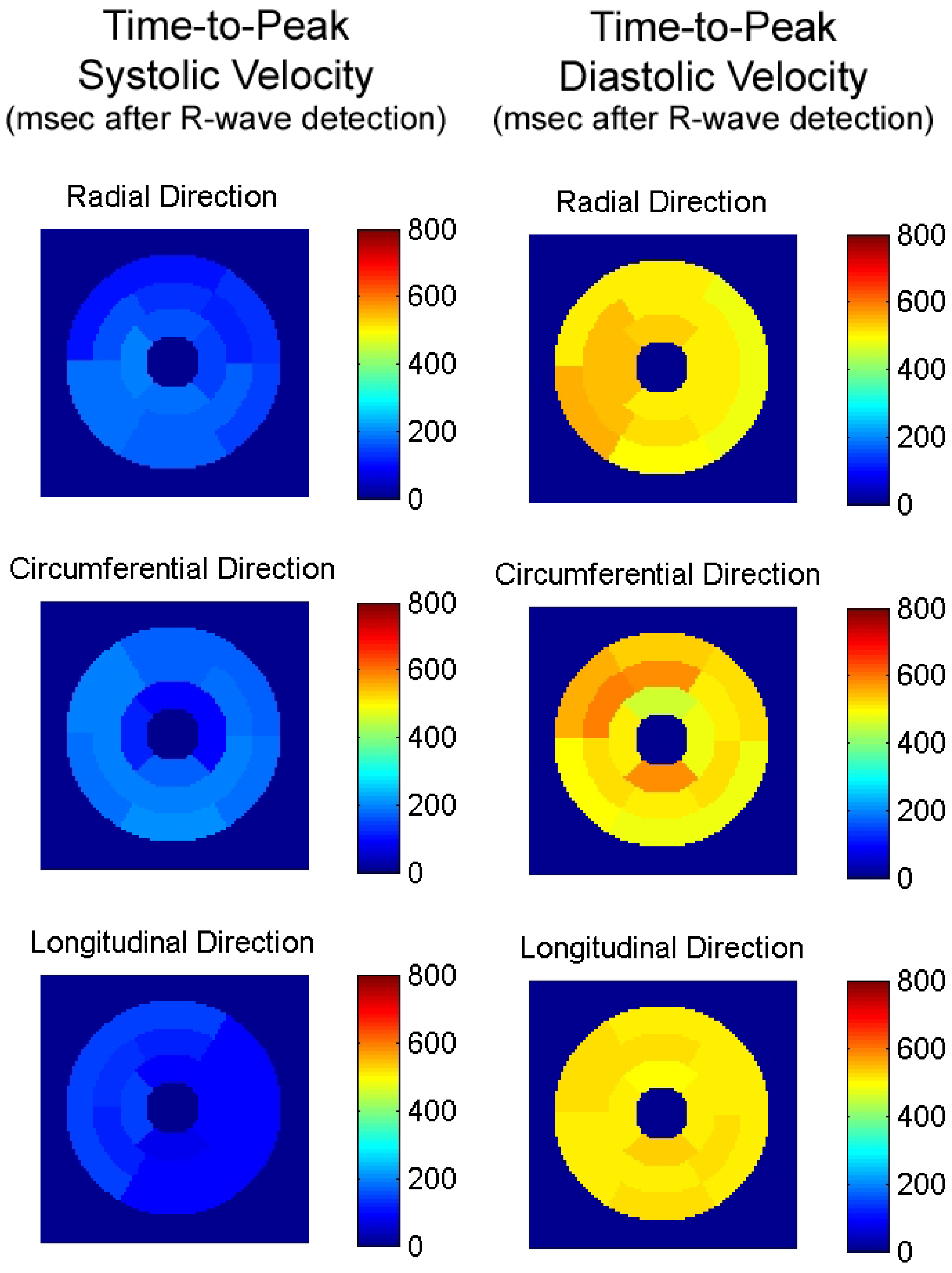

Time-to-Peak Systolic Velocity (msec after R-wave detection)

Time-to-Peak Diastolic Velocity (msec after R-wave detection)

Radial Direction

Circumferential Direction

Longitudinal Direction

Figure 6.4: Time-to-peak velocity database from tracked data

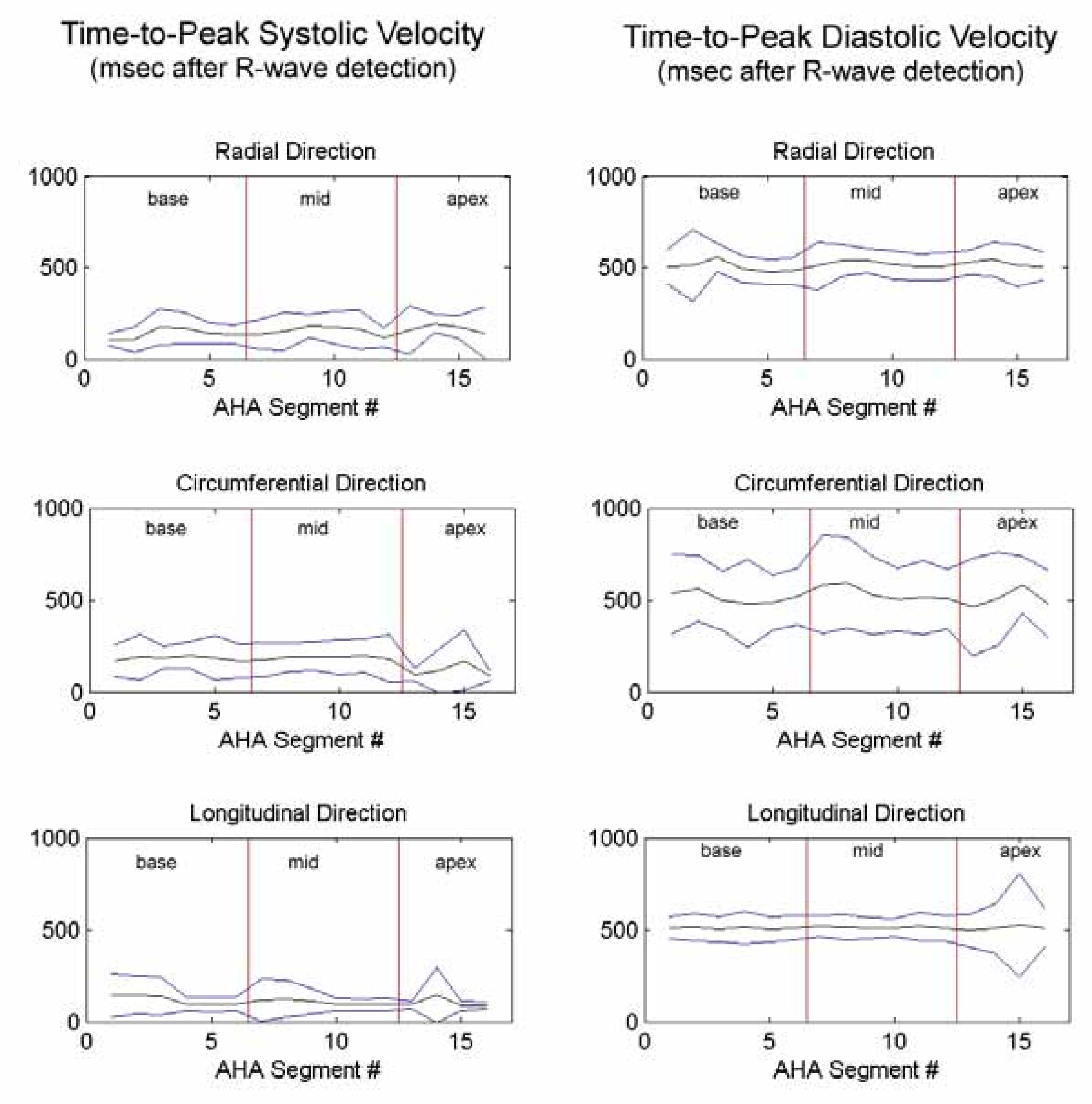

Figure 6.5: Mean +/-2std of time-to-peak velocity in tracked database

Dyssynchrony Measurements

Septal-to-Lateral Wall Motion Delay

For the normal volunteers, the average septal-to-lateral wall motion delay (SLD) throughout the mid and basal slices was 29.5+/-24.5msec in the radial direction, 37.2+/-44.4msec in the circumferential direction, and 35.2+/-44.7msec in the longitudinal direction. For the eight heart failure patients, average SLD was 48.2+/-54.5msec in the radial direction, 71.1+/-59.6msec in the circumferential direction, and 76.3+/-42.8msec in the longitudinal direction. Values of the SLD in the normal volunteers and the dyssynchrony patients are given in Table 6.7. (Note: SLD is given a NaN value if a segment in either the septal or the lateral wall did not meet the criteria for being considered a peak value).

Figure 6.6 illustrates the average SLD across the mid and basal slices in the normal volunteers and heart failure patients. Although patient values of SLD were consistently larger than normal values, the difference was only significant in the longitudinal direction ($p<0.05$), and not in the radial ($p=0.2$) or circumferential directions ($p=0.1$). p-values <0.05 are denoted by * in Figure 6.6.

Table 6.7: Septal-to-Lateral Wall Motion Delay (msec)

Velocity Direction	**Radial**		**Circumferential**		**Longitudinal**	
Slice	**Basal**	**Mid**	**Basal**	**Mid**	**Basal**	**Mid**
Normal Volunteers						
Normal 1	25	64	0	13	64	115
Normal 2	38	13	77	0	25	13
Normal 3	0	0	191	102	13	25
Normal 4	52	13	13	0	13	78
Normal 5	0	13	39	26	26	0
Normal 6	38	64	25	25	51	13
Normal 7	13	89	13	25	89	0
Normal 8	13	26	0	25	51	0
Normal 9	26	13	27	26	132	13
Normal 10	51	38	26	51	0	0
Average	***26***	***33***	***41***	***29***	***46***	***26***
stdev	***19***	***29***	***57***	***29***	***41***	***39***
Heart Failure Patients						
Patient 1	12.5	75.0	125.0	50.0	12.5	75.0
Patient 2	25.5	76.5	127.5	25.5	102.0	178.5
Patient 3	39.7	0.0	39.8	119.3	92.8	26.5
Patient 4	0.0	38.3	63.8	NaN	0.0	51.0
Patient 5	51.0	229.5	140.3	127.5	38.2	242.3
Patient 6	67.5	13.5	13.5	27.0	54.0	13.5
Patient 7	13.2	39.7	53.0	92.8	79.5	26.5
Patient 8	63.8	25.5	76.5	63.8	89.3	127.5
Average	***34.2***	***62.3***	***79.9***	***72.3***	***58.5***	***92.6***
stdev	***25.2***	***72.7***	***46.2***	***41.8***	***38.6***	***82.8***

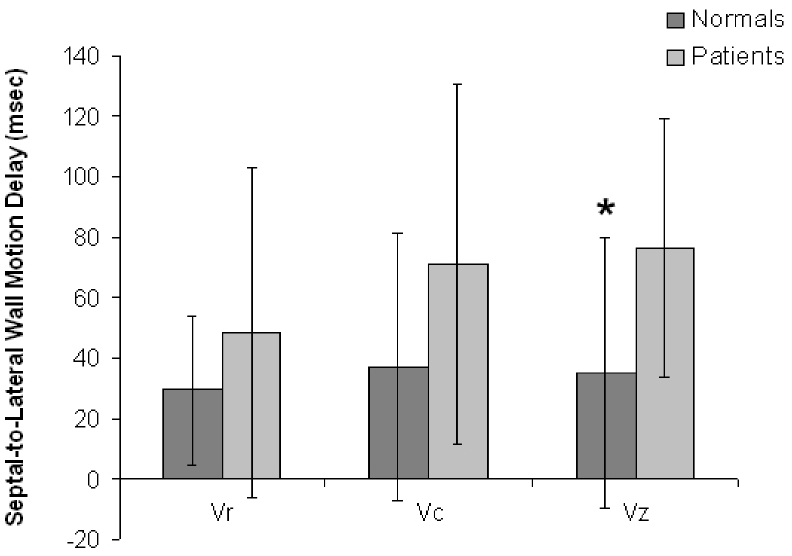

Figure 6.6: Septal-to-lateral Wall motion Delay

$\underline{T_{SD-12}}$

In the normal volunteers, T_{SD-12} values were lowest in the circumferential direction and largest in the radial direction. In the heart failure patients, T_{SD-12} values were smallest in the radial direction and largest in the circumferential direction. T_{SD-12} values for the normal volunteers and dyssynchrony patients are listed in Table 6.8.

For all the directions of motion, the average T_{SD-12} was lower in the normal volunteers than the heart failure patients. However, the difference was only significant in the circumferential and longitudinal, and not the radial (p=0.1) directions, Figure 6.7. * denotes p-values <0.05.

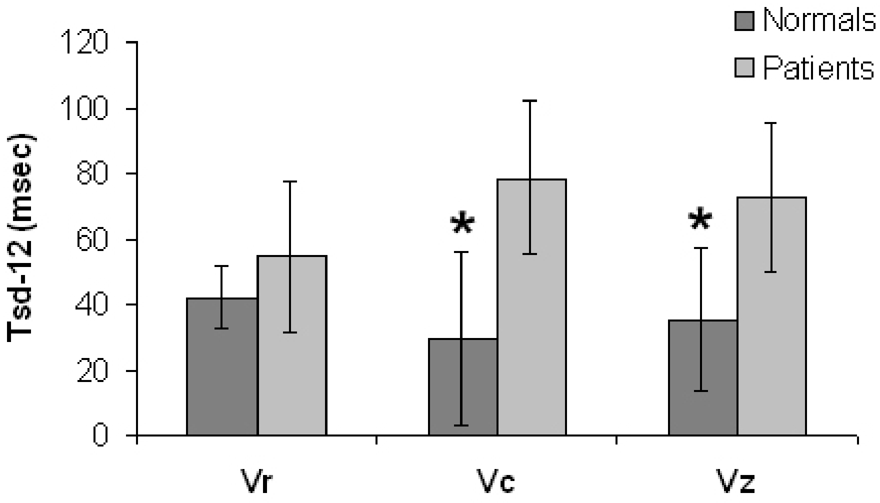

Figure 6.7: Standard deviation of time-to-peak in 12 basal and mid segments

Table 6.8: T_{SD-12} in Normal Volunteers and Heart Failure Patients

Standard Deviation of Time to Peak in 12 mid and basal segments (T_{SD-12}) in msec			
	Vr	**Vc**	**Vz**
Normal Volunteers			
Normal 1	38.2	17.2	48.0
Normal 2	36.1	45.0	13.1
Normal 3	29.8	98.5	14.7
Normal 4	35.6	23.4	36.5
Normal 5	33.9	16.9	13.4
Normal 6	45.9	17.0	49.8
Normal 7	55.9	13.1	43.9
Normal 8	58.9	11.9	49.2
Normal 9	37.5	21.1	72.8
Normal 10	46.3	27.6	7.4
Average	**41.8**	**29.2**	**34.9**
stdev	**9.7**	**26.2**	**21.6**
Heart Failure Patients			
Patient 1	38.9	69.5	51.6
Patient 2	72.5	93.2	100.7
Patient 3	75.3	83.4	83.7
Patient 4	32.3	62.5	34.1
Patient 5	93.7	126.5	98.4
Patient 6	43.1	72.2	63.6
Patient 7	48.5	47.2	73.5
Average	**54.4**	**78.5**	**72.1**
stdev	**23.2**	**23.7**	**22.6**
p-value (patients. vs. normals)	**$p=0.1$**	**$p<0.05$**	**$p<0.05$**

Comparison of Tracked and Non-Tracked Databases

The mean difference in peak systolic velocity between the tracked and non-tracked databases was less than 1cm/s in either the radial, circumferential, and longitudinal directions, Table 6.9. The largest difference in peak velocity between the two databases was observed for peak longitudinal velocity during diastole, in which the velocities magnitudes are greatest. Mean difference in peak longitudinal velocity during diastole was 2.4+/-1.1cm/s. The difference between tracked and non-tracked was smaller for radial (1.4+/10.6cm/s) and circumferential (-0.4+/-0.7cm/s) velocities.

Much less variability was observed in the measurement of time-to-peak velocities between the two databases, where the maximum difference between the tracked and the non-tracked database was 15msec. This difference is less than one frame-to-frame interval in the underlying MR PVM velocity data. Larger differences were observed in the measurement of time-to-peak systolic velocity than time-to-peak diastolic velocity, possibly because diastolic relaxation is a much more rapid process than systolic contraction. During systole, the difference between time-to-peak velocity was 15.0+/-18.8msec in the longitudinal direction, 1-3.8+/-20.8 msec in the circumferential direction, and 11.9+/-14.7msec in the radial direction. During diastole, differences between the tracked and non-tracked databases for measurements of time-to-peak velocity were -2.9+/-13.0msec for longitudinal velocity, 2.8 +/-37.4msec for circumferential velocity, and -2.3+/-10.8msec for radial velocity. Again, the measured difference is less than one frame-to-frame interval in the underlying MR PVM velocity data. The Bland-Altman plots for all four measured parameters in each of the three velocity directions are shown in Figures 6.8 and 6.9.

Table 6.9: Mean difference between tracked and not tracked databases

	Radial Direction	**Circumferential Direction**	**Longitudinal Direction**
Peak Systolic Velocity (cm/s)	-0.6+/-0.2	-0.3+/-0.5	-0.7+/-0.3
Peak Diastolic Velocity (cm/s)	1.4+/-0.6	0.4 +/-0.7	2.4+/-1.1
Time-to-peak systolic velocity (msec)	-11.9+/-14.7	-3.8+/-20.8	-15.0+/-18.8
Time-to-Peak diastolic velocity (msec)	-2.3+/-10.8	-2.8+/-37.4	2.9+/-13.0

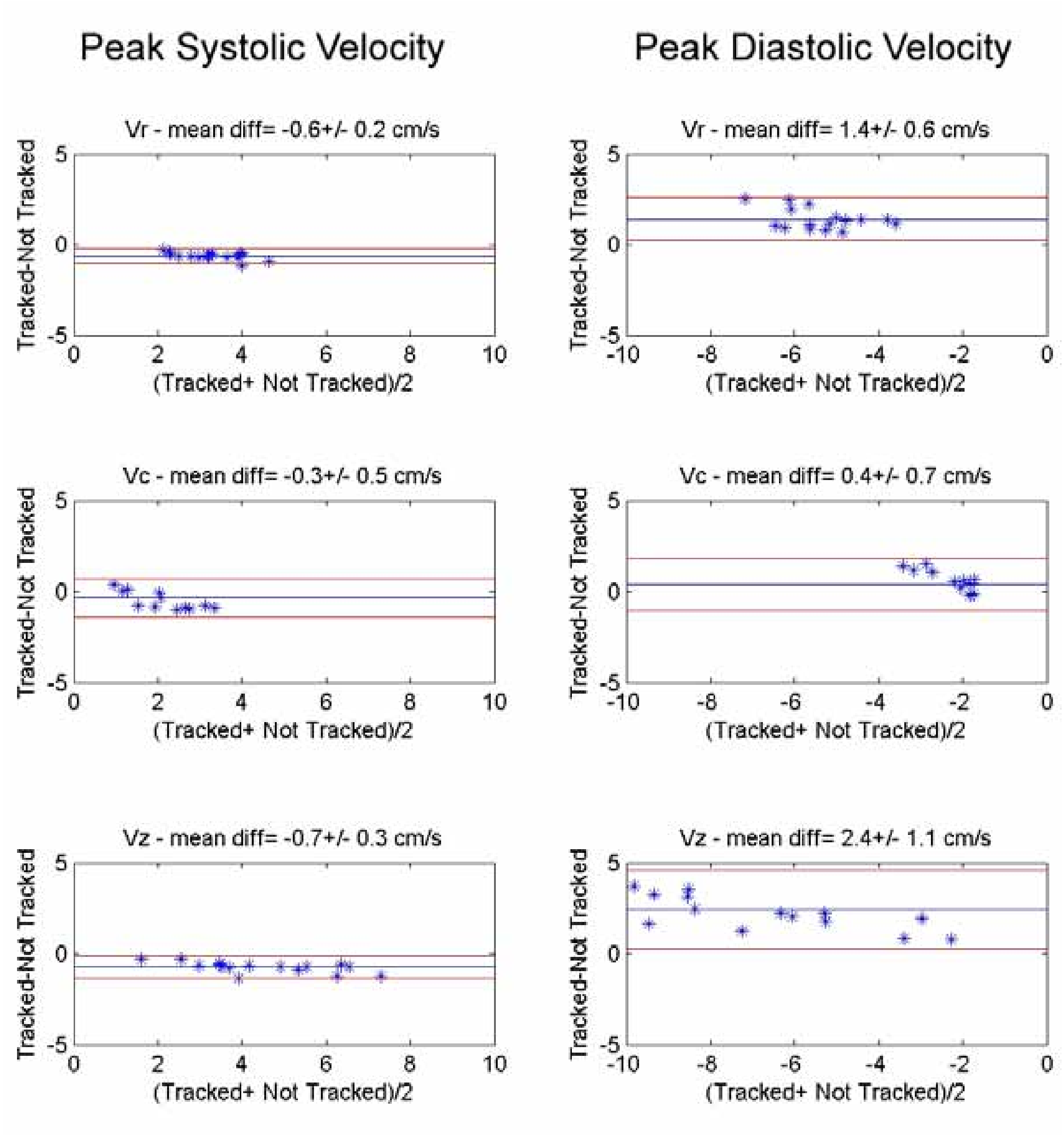

Figure 6.8: *Bland-Altman plots of peak velocities from tracked and non-tracked data*

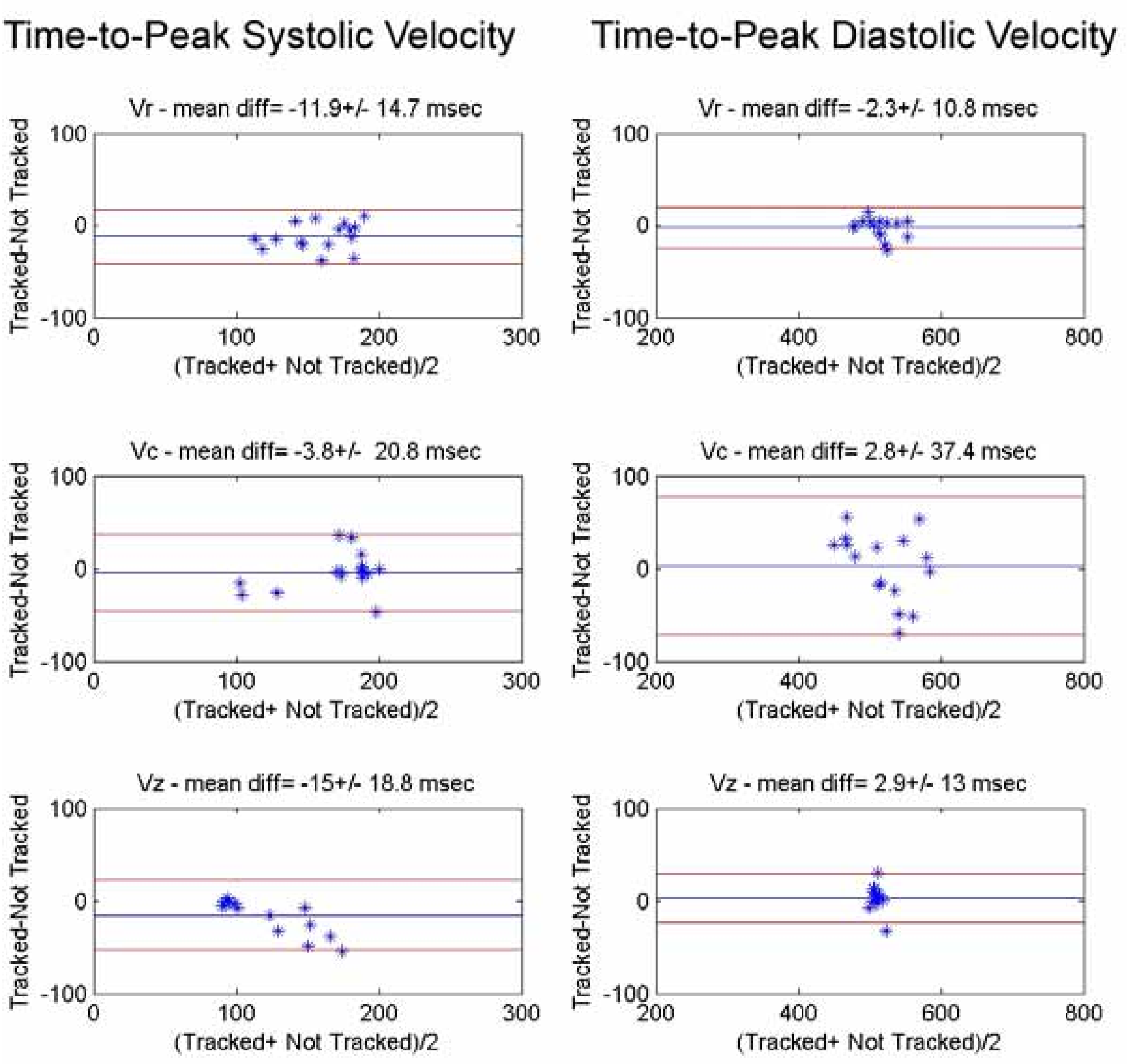

***Figure 6.9**: Bland-Altman plots of time-to- peak velocities from tracked and non-tracked data*

Comparison of Dyssynchrony Patients to the Normal Database

Individual Patient Data

Patient 4

Patient 4 is a 71 year old male with Left Bundle Branch Block (LBBB) and NYHA class III heart failure that is ischemic in origin. Pre-CRT QRS duration was 170msec. The clinical cardiac MR report revealed that assessment of myocardial thickness from cine SSFP images showed a wall thickening defect suggestive of infarct scar in the inferior wall.

Comparison of the timing of peak systolic velocity in the patient to the normal database revealed several delayed regions (segments in which the time-to-peak value for the patient occurred later than the mean value plus two standard deviations). No patient segments were labeled as contracting early (earlier than the normal mean minus two standard deviations). Delayed contraction was not detected in any radial segments. In the circumferential direction, delayed contraction was detected in the lateral wall of the apical and basal slices, and the anterior wall of the middle slice. In the longitudinal direction, a delay in time-to-peak systolic velocity was detected in the lateral wall of the mid and apical slices, and in the inferior wall of all three slices.

Figure 6.10 shows the Bulls-Eye maps of time-to-peak systolic velocity in the patient compared to the normal database. Segments shown in red were delayed when compared to the normal database, segments shown in blue contracted early, and segments shown in gray were within two standard deviations of the normal mean. Areas of the myocardium where a positive peak systolic value could not be detected between aortic valve opening and closing time are designated as "No Value."

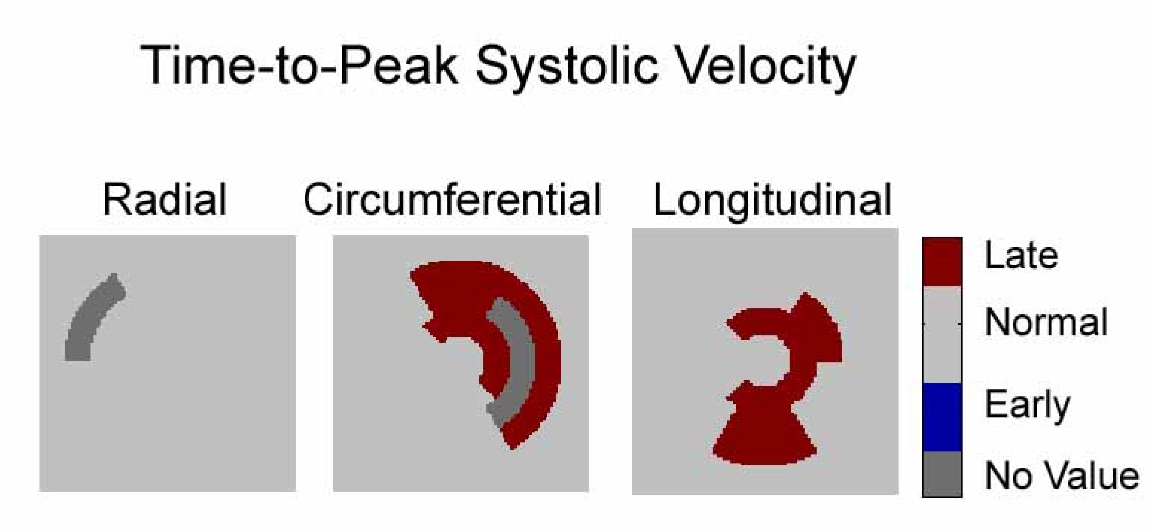

Figure 6.10: Bulls-eye plot of patient 4 compared to the normal database

In summary, a delay in time-to-peak systolic velocity was observed in the lateral wall for patient 4 in the circumferential and longitudinal directions. No delay in time-to-peak systolic velocity was seen in the radial direction. In the longitudinal direction, delayed systolic contraction was also observed in the inferior wall in the area corresponding to the location of the known infarct.

Patient 5

Patient 5 is a 66 year old male with LBBB and NYHA class III heart failure. Pre-CRT QRS duration was 194 msec. The patient's heart failure was listed as being nonischemic in origin, and the clinical cardiac MR report detected no areas of focal hyperenhancement, consistent with the absence of myocardial scarring or infarction. However, the perfusion report showed delayed perfusion in the mid to distal septum.

When the time-to-peak systolic velocity values for this patient were compared to the normal database, several areas of delayed contraction were identified. The radial direction showed delayed segments in the septal, anterior, and inferior walls. The circumferential direction showed a delay in time-to-peak within the lateral and anterior walls, and time-to-peak systolic velocity in the longitudinal direction was delayed in the entire lateral wall, as well as the mid and apical septum. Time-to-peak systolic velocity was not detected as occurring earlier than two standard deviations of the normal mean in any myocardial region, in either of the three velocity directions.

The Bulls-Eye plot showing the delayed segments for patient 5 is shown in Figure 6.11. As with the previous example, normal segments are shown in gray, delayed segments are shown in red, and early segments are shown in blue. Segments in which a positive peak systolic value could not be detected between aortic valve opening and closing time are designated as “No Value.”

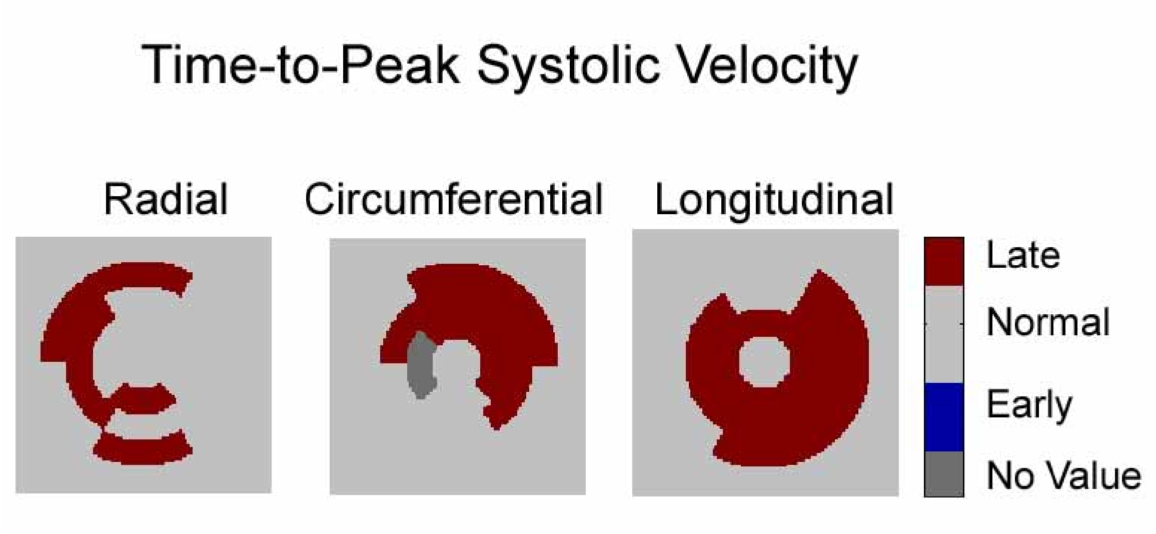

Figure 6.11: Bulls-eye plot of patient 5 compared to the normal database

In summary, a delay in time-to-peak systolic velocity in the lateral wall was observed in the circumferential and longitudinal directions for patient 5. Delayed contraction in the longitudinal and radial directions was also observed in the septum at a location corresponding to the area of delayed perfusion.

Different Classifications with the tracked or non-tracked databases

On average, 8.0+/-0.5% of segments in each patient received a different characterization depending on if the tracked or non-tracked databases were used. In no patient was the classification of more than 10% of segments different.

The location of the myocardial segment did not have a strong affect on whether segments were categorized differently. An average of 8.0+/-0.6% of the total segments at each AHA location received a different label when compared to the normal database using the tracked or non-tracked data. In no myocardial location did more than 10% of segments receive a different label when compared to the tracked or non-tracked databases.

A trend was observed between the direction of motion and segments receiving different outcomes when compared using the tracked or non-tracked databases. For peak velocity measurements, the number of segments with different outcomes was significantly larger in the circumferential direction than the radial or longitudinal directions, Figure 6.12. The largest difference was observed for peak circumferential velocity during systole, where 25% of segments were labeled differently (compared with 18% of segments in the radial direction and 18% of segments in the longitudinal direction). The same trend was observed during diastole, where 11% of segments in the circumferential direction, and 7% of segments in the radial and longitudinal directions were labeled differently depending on if the tracked or non-tracked databases were used.

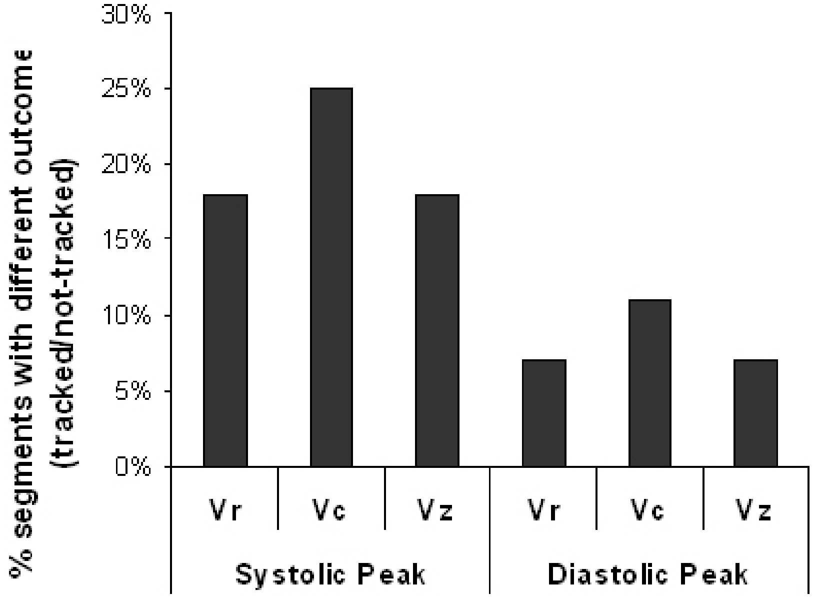

Figure 6.12: *Segments with different outcomes for peak velocity measurements*

A similar trend was observed for measurements of time-to-peak velocities, although the total number of segments with different outcomes was significantly smaller, Figure 6.13. In general, greater variability was observed in measurements of time-to-peak systolic velocity than measurements of time-to-peak diastolic velocity. The largest variability was observed for measurements of time-to-peak systolic circumferential velocity where 4% of segments were labeled differently, compared to 0% of segments in the radial direction and no segments in the longitudinal direction. During diastole, an even smaller number of segments received different labels when compared to the tracked or non-tracked databases: 2% of segments in the radial and circumferential directions, and no segments in the longitudinal direction.

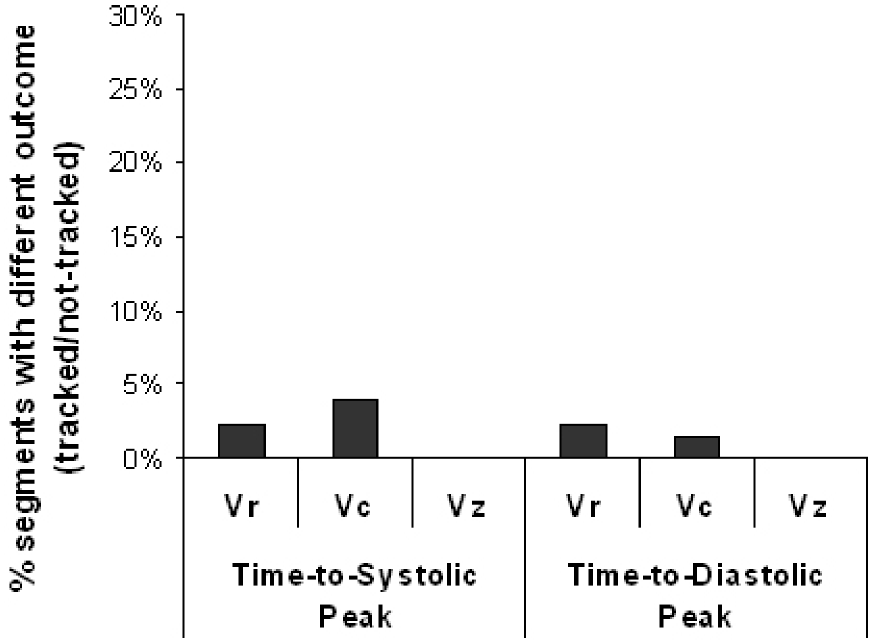

Figure 6.13: Segments with different outcomes for time-to-peak velocity measurements

Discussion

Databases describing the four parameters of the normal myocardial contraction pattern (peak systolic velocity, peak diastolic velocity, time-to-peak systolic velocity, and time-to-peak diastolic velocity) were constructed from a group of ten normal volunteers. Databases were constructed using both tracked and non-tracked velocity data, and it was determined that the choice of velocity data did not have a major affect on the value of the database parameters. Velocity data was also acquired in eight heart failure patients prior to CRT implantation, and patient values were compared to the normal databases, both on an individual patient basis and as a group. Systolic dyssynchrony values (SLD and T_{SD-}

$_{12}$) were computed for both the normal and patient populations, and significantly higher levels of dyssynchrony were detected in the patient population for both parameters.

Peak velocities

Peak velocity measurements within the normal database illustrated several main trends:

1. The direction of circumferential velocity changed along the long-axis of the LV, with basal and apical slices twisting in opposite directions.
2. Peak velocities measured in the longitudinal direction were consistently the largest velocity magnitude, while peak circumferential velocities were consistently the smallest in magnitude. This finding held true during both systole and diastole.
3. Peak diastolic velocities were larger than peak systolic velocities in all three directions of velocity.
4. Peak radial velocities were relatively constant between the apical, mid, and basal slices. Peak circumferential velocities were largest in the apical slice and smallest in the mid slice. Peak longitudinal velocities decreased with distance toward the apex, with the greatest velocities observed in the basal slice and the smallest velocities observed in the apical slice.
5. Peak circumferential velocities were relatively consistent throughout the entire imaging slice. Peak radial and longitudinal velocities, however, were consistently

larger in the lateral wall than the septal wall; this difference was observed across all three myocardial slices, both during systole and diastole. This observation can be explained by tethering effects from the right ventricle in the septal wall which restrict motion.

The normal database depicted the value of peak velocity within each myocardial segment averaged over the ten normal volunteers. It is reassuring to observe that the standard deviations of these average velocities were fairly small (Figure 6.3), indicating that at least within this population, the values of peak velocities are consistent. The widest standard deviation was observed for measurements of peak circumferential velocity during diastole. The magnitude of peak circumferential velocities was significantly less than the magnitudes of peak radial or longitudinal velocities, particularly during diastole. Since the same velocity encoding value (Venc=30cm/s) was used to encode velocities in all three directions, the lower velocities in the circumferential direction would have resulted in a lower velocity-to-noise ratio; this may help explain the larger standard deviation in the measurements.

During data analysis, the restriction was imposed that peak velocities during systole had to be positive, while peak velocities during diastole had to be negative. Essentially this imposed a minimum threshold or cutoff value on the peak velocities. In the present analysis, the value of this threshold was set at zero, but the threshold can be increased as a means of removing akinetic segments from the analysis. The present analysis was focused on constructing a database from normal velocity data, so such a threshold was not imposed at this time.

Time-to-peak velocities

The main findings for measurements of time-to-peak velocity throughout the normal myocardium were:

1. Time-to-peak velocity is uniform throughout the entire LV and across all ten normal volunteers.
2. Radial and longitudinal time-to-peak measurements are more robust than circumferential time-to-peak measurements.
3. No consistent, significant differences in timing between the septal and the lateral walls of the myocardium were observed.

The standard deviation of time-to-peak velocity measurements was significantly larger in the apical slice than either the mid or basal slices (Figure 6.5). This may be at least partially explained by the image acquisition method. During acquisition, rest slabs were placed on both sides of the imaging slab, not on either side of each imaging slice. Therefore, the signal from inflowing blood was nulled effectively in the basal and mid slices, but by the time the blood reached the apical slice, it had sufficient time to regain at least some signal strength, so the contrast between blood and myocardial tissue was decreased in the apical slice. This may have decreased the accuracy of measurements taken in the apical slice and thereby, increased the standard deviation of apical values in the normal database. For this reason, the apical myocardial segments (AHA segments 13-16) were excluded from the analysis of dyssynchrony.

Dyssynchrony Measurements

In the normal volunteers, myocardial contraction should be synchronous, and, ideally, the septal-to-lateral wall motion delay (SLD) should be zero. In most normal volunteers, the observed SLD was a single myocardial frame. This can be attributed to measurement error and does not imply an underlying level of dyssynchrony in the normal population.

Two normal volunteers had a SLD greater than 100 msec in the longitudinal direction. Although this suggests an underlying level of dyssynchrony within the normal population, closer examination of the velocity curves gives insight into the measurements. Longitudinal velocity curves often exhibit two systolic peaks, and either peak can be chosen as the “peak” value. The problem arises when the first and second peak values have different magnitudes in different walls of the myocardium, and an apparent dyssynchrony is detected.

The phenomenon is illustrated below with an example. Figure 6.14 shows the longitudinal velocity curves from one of the two normal volunteers with a SLD greater than 100msec. In both the septal and lateral walls, an initial systolic peak occurs simultaneously shortly after the opening of the aortic valve (AVo). In the septal wall, however, a second peak is also observed. Since the second peak is larger than the first, it is picked up by the automated algorithm as the peak value, and a SLD of 132 msec is detected in the normal volunteer. In the figure, the detected peak values in the septal and lateral walls are denotes with a *.

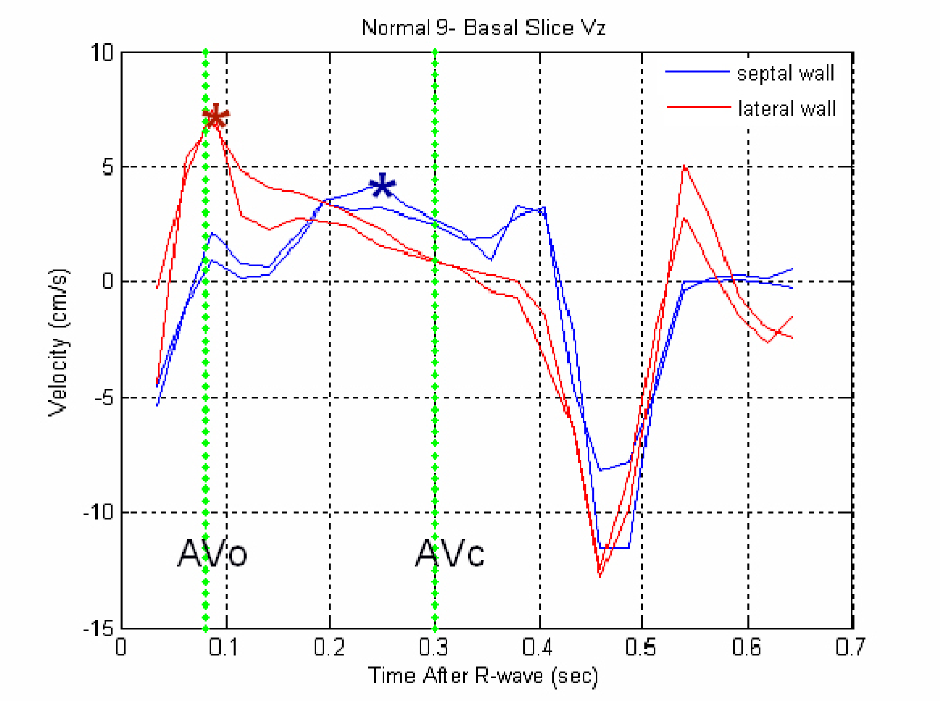

Figure 6.14: "Dyssynchrony" in the normal volunteer

The T_{SD-12} measure of dyssynchrony takes into account velocity curves from all regions of the myocardium, not just the septal and lateral walls. Therefore, T_{SD-12} should be more robust and be able to detect dyssynchrony in any region of the myocardium, not just between the septal and lateral walls. T_{SD-12} was even more efficient at separating normal and patient values than the SLD: the difference between the two groups was significant in the circumferential and longitudinal directions, and although the difference was not significant in the radial direction, patient values were still larger than normal values.

Tracked vs. Non-tracked Databases

The finding that only minor differences exist between databases constructed from tracked and non-tracked data is somewhat surprising. It was expected that tracking of individual pixels throughout the myocardium would produce velocity curves different from those derived from a stationary ROI placed in the myocardium throughout the cardiac cycle. The relatively large area over which velocities were average (1/6th of the myocardial slice in the basal and mid slices, and 1/4th of the myocardial slice in the apex), could have obscured some of these differences.

However, it is important to clarify that the non-tracked data did also follow myocardial motion in the radial direction. In order to measure velocities within the myocardium, a template was created for each frame of the cardiac cycle in which the endocardial and epicardial borders of the myocardium were manually traced. Myocardial velocities within these borders in each frame were averaged into six myocardial segments in accordance with the AHA segmentation guidelines. This method ensured that velocities outside of the myocardium were not included in the segmental average. However, the tracing of the endocardial and epicardial borders essentially followed or "tracked" these borders throughout the cardiac cycle, if only in the radial direction. No such tracking was performed in the circumferential or longitudinal directions. Therefore, the individual pixels within segments of the myocardium in the non-tracked database did change throughout the cardiac cycle.

Also important to note is that true tracking was only performed in the two in-plane directions. In the thru-plane direction, average velocity values were acquired throughout a 10mm imaging slice. Since the thru-plane velocity used in the tracking algorithm was the same regardless of the tracked thru-plane location, the pixels were not truly "tracked" in the thru-plane direction.

The largest standard deviation between the tracked and non-tracked databases was observed for measurements of time-to-peak circumferential velocity; this standard deviation (both during systole and diastole) was several times larger than the standard deviation for measurements of time-to-peak radial velocity. This may be at least partially explained by the lower values of circumferential velocities, which make circumferential velocity measurements more susceptible to noise.

A bias was observed in measurements of peak diastolic longitudinal velocity, with the tracked values being an average of more than 2 cm/s larger than the non-tracked values. The reason for this bias is not known at the time; in fact, it was expected that peak values from the tracking algorithm would be greater in magnitude than the non-tracked values, as the tracking algorithm follows the true motion of pixels throughout the cardiac cycle.

Comparison of Dyssynchrony Patients to the Normal Database

Individual Patient Data

Time-to-peak systolic velocity in the two patients compared individually to the normal database showed a delay in the lateral wall when compared to the normal database. Although this delay was expected in both the radial and longitudinal directions, it was only observed consistently in the longitudinal direction. At this time it is not clear if such a delay only exists in this direction, or if the velocity acquisition protocol is not sensitive enough in the radial direction to detect the delay.

In the current analysis, patient values more than two standard deviations from the normal mean were selected as being abnormal and potentially indicative of dyssynchrony. This two standard deviation cutoff value was selected based on the assumption that values within the normal database exhibit a normal distribution and that 95% of the normal data will be contained within two standard deviations of the mean value. However, further studies are necessary to determine if these assumptions are accurate and what cutoff value is truly indicative of dyssynchrony.

Different outcomes with Tracked and non-tracked databases

Measurements of peak circumferential velocity were much more likely to be classified differently whether compared to either the tracked or the non-tracked databases than either peak radial or longitudinal velocity measurements. Several factors may account for these trends. In general, peak circumferential velocities are smaller in magnitude than peak radial or longitudinal velocities. Since a uniform velocity encoding value was used for the measurement of velocities in all three directions, the velocity-to-noise ratio will be smaller for the smaller velocities of circumferential motion. This will make the signal more susceptible to noise and difficult to interpret.

In addition, peak velocity measurements were much more likely to be classified differently than time-to-peak velocity measurements. This may be explained by the fact that employing the tracking algorithm will likely change the magnitude of peak velocities without affecting the timing of the peak velocities.

Finally, the most robust measurements were time-to-peak measurements during diastole. Diastolic relaxation is a much more rapid process than systolic contraction. Diastolic relaxation often appears only in a single frame on velocity images and peak diastolic velocities are easily identified on velocity curves as sharp negative peaks. In comparison, systolic contraction is a slower process with lower velocities that often develop over several MR PVM time frames. It is not uncommon to see velocity curves with two peaks during systole, or in which systole is depicted as a slowly increasing curve. Therefore, it is much easier to accurately and reproducibly identify the time-to-peak diastolic contraction velocity.

Study Limitations

Age of Subjects

Average age of the volunteers for the normal database was 27.2+/-4.9 years, while the average age of the eight heart failure patients was 55.0+/-11.8 years. It has previously been shown that the magnitude of peak contraction velocities decreases with increasing age[161], and that aging leads to a prolongation of diastolic filling time[52,59]. Under ideal conditions, the normal database would have been constructed from volunteers agematched to the heart failure patient population. Since that was not possible for this study, comparisons between patient and normal values were only made for the timing of systolic velocities, not for the magnitude of peak velocities or the timing of diastolic velocities.

Twist in Middle Myocardial Slices

During normal cardiac contraction, basal and apical myocardial slices twist in opposing directions. In basal slices, systolic velocities are positive (clockwise rotation when observed from the apex) and diastolic velocities are negative (counter-clockwise rotation when observed from the apex). At the apex, systolic velocities are negative (counter-clockwise rotation) and diastolic velocities re positive (clockwise rotation). The direction of twist reverses somewhere along the length of the LV, but the exact location cannot be delineated based on three-slices of data collected in this study.

During systole, the algorithm that identified peak velocities searched for the largest positive circumferential velocity in the basal slice, but the largest negative circumferential velocity in the apical slice; during diastole the signs on the velocities were reversed. Since the direction of twist in the middle slice was unknown, the assumption was made that twist in the middle slice more closely resembled the twist in basal slice than the apical slice. However, it is possible that the middle slice was taken at a location twist more closely resembled the apical slices, and thus, the search for peak velocities was incorrect. In the future, a long-axis slice with three-directional velocity encoding or more detailed short axis slices would be helpful in identifying the location of twist reversal and correctly identifying peak velocities in the middle slice.

Time-to-Peak Analysis

Database values are in pure time after detection of the R-wave rather than percentage of cardiac cycle, meaning that the same scale is used for all subjects, regardless of heart rate. This approach was chosen over a sliding scale where time-to-peak was determined as a percentage of total cardiac cycle length because the length of systole is fairly constant, regardless of heart rate. Systolic length does not begin to change until high heart rates are reached, which we did not anticipate happening to subjects under resting conditions within the MR magnet. Therefore, measurements of time-to-peak systolic velocity conducted in a straight time-scale can be compared between subjects with different heart rate. The length of diastole, however, is highly variable depending on heart rate. However, the difference is primarily in the length of the resting diastole period, and not the active relaxation. Therefore, a subject with a drastically lower heart rate will have a much longer diastolic period, but during the majority of that time the heart will not be moving. Therefore, we felt that it was better to compare the straight times than to normalize to percentage of cardiac cycle. However, as has been reported previously, the most accurate option would have been to utilize a combination of the two[162].

Conclusions

Databases describing four parameters of the normal myocardial contraction pattern (peak systolic velocity, peak diastolic velocity, time-to-peak systolic velocity, and time-to-peak diastolic velocity) were constructed from a group of ten normal volunteers.

Databases were constructed using both tracked and non-tracked velocity data, and it was determined that the choice of velocity data did not have a major affect on the value of the database parameters. Velocity data was also acquired in eight heart failure patients prior to CRT implantation, and patient values were compared to the normal databases, both on an individual patient basis and as a group. Systolic dyssynchrony values (SLD and T_{SD-12}) were computed for both the normal and patient populations, and significantly higher levels of dyssynchrony were detected in the patient population for both parameters.

CHAPTER 7

DEVELOPMENT OF SOFTWARE FOR COMPUTING RADIAL STRAIN AND STRAIN RATE FROM MR PVM VELOCITY DATA

Introduction

The relatively high spatial resolution of MR PVM data offers the possibility of computing strain values within the myocardium on a pixel-by-pixel basis. Furthermore, MR PVM velocity data offers the possibility of differentiating between endocardial and epicardial strain and strain rate (SR) values. In addition, the three-directional nature of the underlying velocity data makes it possible to compute radial strain values, a quantity that is particularly difficult to measure with ultrasound.

The objectives of this study were 1) to develop a technique for measuring radial strain and SR from MR PVM tissue velocity data and 2) to evaluate differences in radial strain and SR between the endocardial and epicardial layers of the myocardium.

Methods

Study Population

Ten normal, healthy volunteers (mean age 27.7+/-5.1 yrs, 8 male) participated in this study. The study protocol was approved by the University's Institutional Review Board, and informed consent was obtained from all participants prior to participation.

Imaging Protocol

Survey images were acquired first, followed by two-chamber vertical long axis (VLA), four-chamber horizontal long axis (HLA), and short axis (SA) steady-state free procession (SSFP) cine images. Velocity images were acquired using the final protocol outlined in Chapter 3.

Background phase error was removed using a least-squares plane fitted to static tissue, as describing in Chapter 3[130]. The acquired three-directional velocities were converted to radial velocity (positive toward the center of the LV blood pool), longitudinal velocity (positive toward the apex), and circumferential velocity (positive for clockwise rotation when viewed from the apex).

Computation of Radial Strain and SR

Radial SR was calculated directly from radial velocity data. For each phase in the cardiac cycle, radial velocity was measured along 48 equally-spaced lines emanating radially outward from the center of the LV blood pool. The velocity difference between two points a half-pixel distance apart along a line in the myocardial wall was plotted against change in radius between the two points; the process was repeated for every combination of two points in the myocardium along a given line. SR at that myocardial location was calculated as the slope of the regression line[163].

By convention, radial SR values were defined as positive for myocardial thickening and negative for myocardial thinning. By using all the points along the radial line, the average transmural SR throughout the entire myocardial wall was determined. To compute endocardial and epicardial SR values, the thickness of the myocardial wall along each radial line was subdivided into two regions, and the SR was computed independently for each region.

Figure 7.1 illustrates the method for computing radial strain rate from MR PVM velocity data. Figure 7.1A shows the short-axis MR image of the myocardium and the 48 lines along which radial velocities were measured. Figure 7.1B shows a template of the segmented myocardial wall and points in a single line along which velocity differences were taken. In this particular example, the myocardium is 8-pixels thick; the myocardial template shows 15 points (half-pixel steps) where velocity differences were computed. Figure 7.1C shows a graph of change in radius (dr) vs. change in velocity (dV) between all points in the template shown in B. For the 15 locations shown in B, there are 105 unique two-value combinations of dV/dr, explaining the large number of points shown in 7.1C. Points used to compute transmural strain rate are shown as light gray dots; endocardial points are shown as crosses and epicardial points are shown as triangles. Figure 7.1D shows the strain rate curve throughout the entire cardiac cycle from the same region. The * denotes the strain rate values computed from the plot in C).

Strain was determined by integration of the SR curves ($\varepsilon=\int SR\, dt$). Drift was corrected by applying an algorithm currently used in ultrasound strain imaging. Briefly, the physical boundary condition that strain must return to its initial starting value was applied, and a linear correction was applied to the strain curve[164].

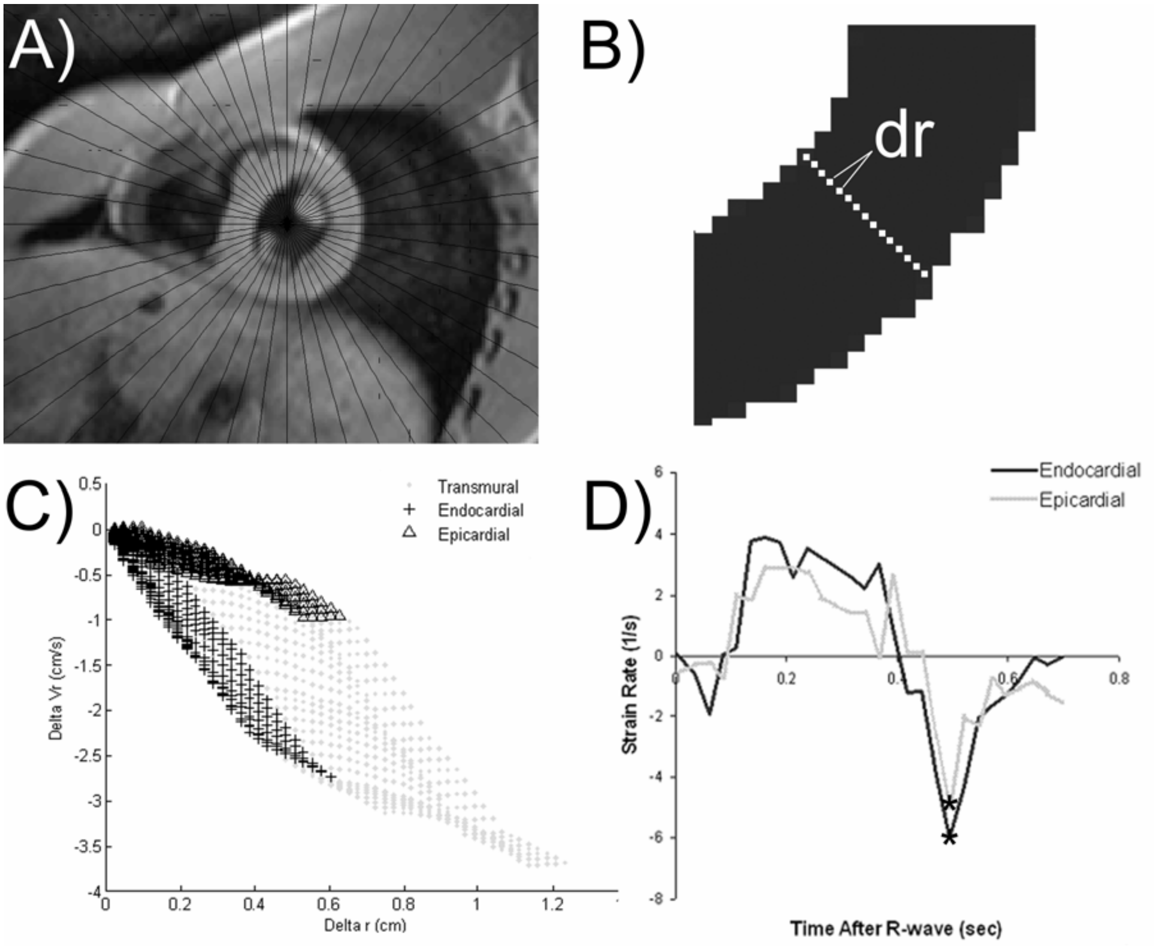

Figure 7.1*: Method for computing radial strain rate from MR PVM velocity data.*

For each imaging slice the analysis yielded transmural, endocardial, and epicardial strain and SR values for 48 myocardial locations in each phase of the cardiac cycle. In accordance with American Heart Association (AHA) guidelines for standardized myocardial segmentation, values in the mid and basal slices were each averaged into six segments[135].

Validation of Transmural Strain Values

Endocardial and epicardial borders were traced on a basal slice of short axis steady state free procession (SSFP) images acquired at the same location as the MR PVM tissue velocity maps using MASS (Myocardial Analysis Software, AZL, Leiden, The Netherlands). Radial strain values were computed from these contours based on myocardial thickness (T) over time. Eulerian strain was computed as the difference between myocardial thickness at a given time point (t) and the thickness at the end-diastolic starting point (t_o) divided by thickness at the current time point [$\varepsilon=[T(t)-T(t_o)]/T(t)$]. To compare data with transmural strain values computed from MR PVM velocity data, strain values were also averaged into six basal segments in accordance with AHA standardized myocardial segmentation guidelines.

Statistics

Peak transmural radial strain values computed from MR PVM tissue velocity data were compared to peak transmural radial strain values computed cine SSFP contours in the same AHA segment using Bland-Altman analysis. Peak endocardial and epicardial values were compared using a paired, two-tailed t-test with p-values <0.05 considered statistically significant.

Results

Three-directional velocity maps were successfully acquired in all study participants, and strain and SR values were computed from all radial velocity datasets.

Radial SR values were positive during systole (contraction) and negative during diastole (relaxation). Figure 7.2A shows transmural radial strain rate curves from the six AHA segments in the basal slice of a healthy volunteer. Figure 7.2B shows strain curves from the same six basal segments in the same volunteer. The curves clearly depict the evolution of myocardial contraction and relaxation.

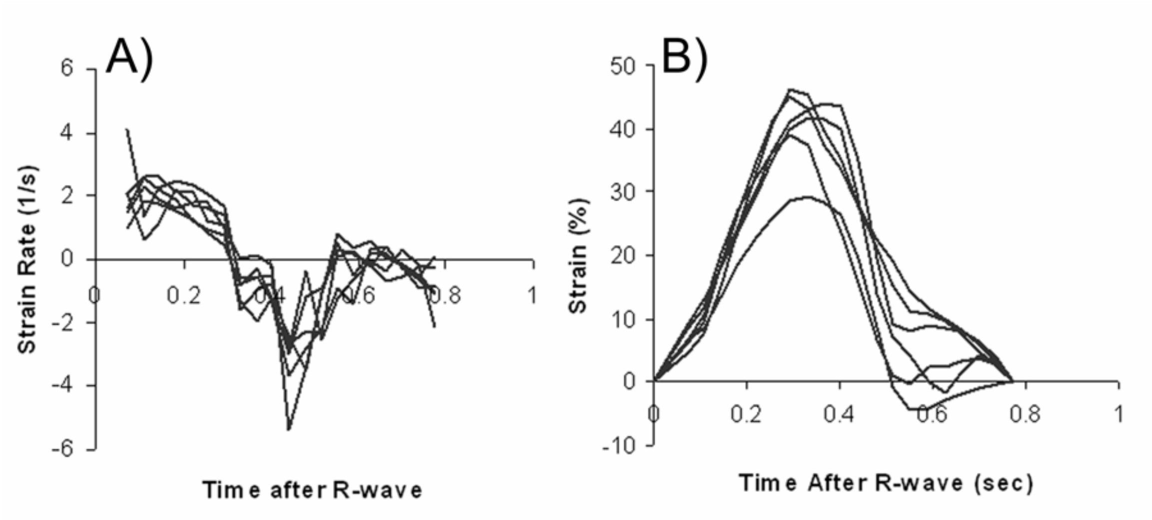

Figure 7.2: *Transmural radial strain and SR curves from a normal volunteer.*

Validation of Transmural Radial Strain Values

Excellent agreement was observed between peak strain values computed from contours drawn on the cine SSFP images and strain derived by MR PVM tissue velocity images. Peak strain values computed by cine SSFP and MR PVM were not significantly different in any of the six basal segments examined. Figure 7.3 shows the average of peak strain values by MR PVM tissue velocity mapping and cine SSFP wall thickening from 10 normal volunteers.

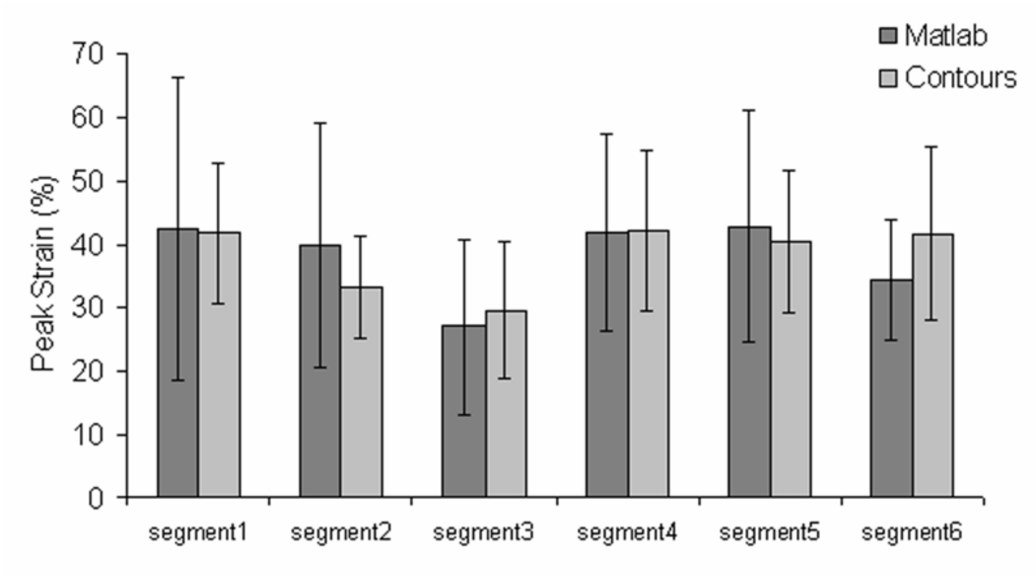

Figure 7.3*: Validation of peak transmural radial strain measurements.*

Across all six basal regions, average peak strain determined by the contours was 38.1+/- 5.4%, and by the MR PVM velocity technique was 38.0+/-6.2%, giving an average difference between the two techniques of 0.1%, Table 7.1. Bland-Altman analysis showed that the mean difference between the contour and MR PVM method for all measurements of peak strain was -0.18 +/- 18.3%.

Table 7.1*: Comparison of peak transmural strain values*

AHA segment #	**Contours on cine SSFP images (%)**	**Strain from MR PVM velocity data (%)**	**Difference Contours-MR PVM (%)**	**p-value**
1	41.8 +/-11.0	42.3 +/-23.9	-0.6	p=NS
2	33.3 +/- 8.1	39.9 +/- 19.3	-6.6	p=NS
3	29.5 +/- 10.9	27.0 +/- 13.8	2.5	p=NS
4	42.2+/-12.6	41.8 +/- 15.7	0.4	p=NS
5	40.5 +/- 11.2	42.8 +/-18.2	-2.3	p=NS
6	41.6 +/- 13.6	34.3+/-9.4	7.3	p=NS
average	*38.1+/-5.4*	*38.0+/-6.2*	*-0.1*	*P=NS*

Endocardial-Epicardial Strain Gradient

Peak endocardial radial strain values were significantly larger than peak epicardial strain values. In the basal slice, the value of peak endocardial radial strain was 45.3+/-25.6% and the value of peak epicardial radial strain was 35.6+/-20.7%, $p<0.05$. In the mid slice, peak endocardial values were also larger than peak epicardial values (peak endo=41.3+/-31.9%, peak epicardial radial strain=31.6+/-18.9%, $p<0.05$).

Endocardial-Epicardial SR Gradient

An endocardial-epicardial SR gradient was also observed, with peak endocardial SR values being larger than peak epicardial SR values. During systole this endocardial-epicardial SR gradient was observed in both the mid and basal slices. In the basal slice, peak endocardial SR values were 4.5+/-2.3 $s^{-1}$and peak epicardial SR values were 3.4+/-1.8 s^{-1}, $p<0.05$. In the mid slice, peak endocardial SR was 3.6+/-1.6 s^{-1} and peak epicardial SR was 2.9+/-1.3 s^{-1}, $p<0.05$. Figure 7.4 shows peak endocardial and epicardial strain and SR values during systole. * denotes where peak endocardial values were significantly larger than peak epicardial ($p<0.05$).

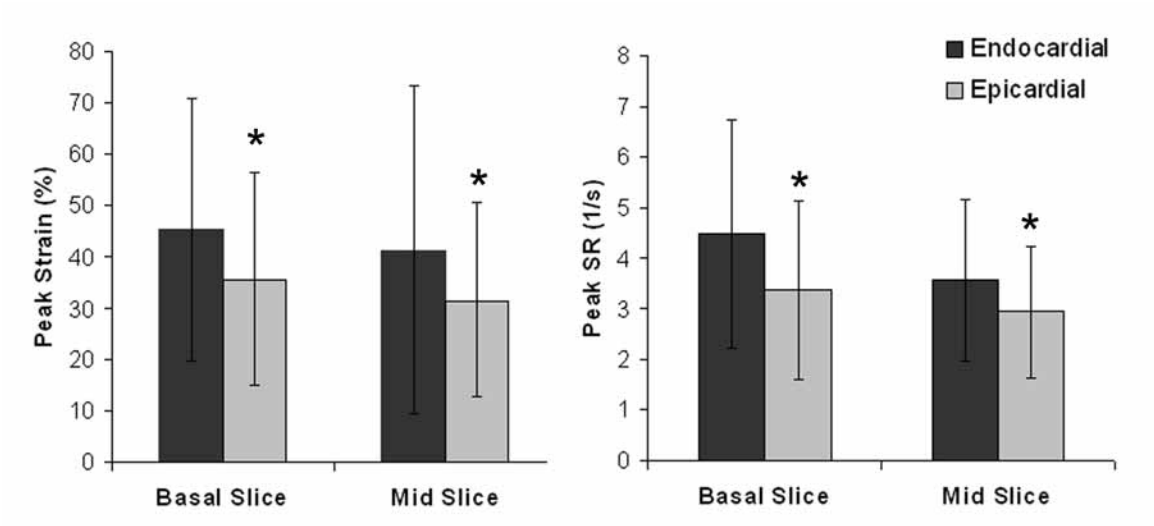

***Figure 7.4**: Peak endocardial and epicardial strain and SR values during systole.*

Peak endocardial SR values were also greater in magnitude than peak epicardial SR values during diastole, although the differences were not significant, Table 7.2. (Basal slice, peak endocardial SR=-4.9+/-2.3 s^{-1}, peak epicardial=-4.4+/-2.3 s^{-1}, p=NS; mid slice peak endocardial=-4.4+/-2.8 s^{-1}, peak epicardial=4.0+/-1.4 s^{-1}, p=NS).

Table 7. 2: *Peak Endocardial and Epicardial Strain Rate Values*

	Basal Slice	**Mid Slice**
Systole		
Endocardial Peak (s^{-1})	4.5+/-2.3	3.6+/-1.6
Epicardial Peak (s^{-1})	3.4+/-1.8	2.9+/-1.3
p-value	$p<0.05$	$p<0.05$
Diastole		
Endocardial Peak (s^{-1})	-4.9+/-2.3	-4.4+/-2.8
Epicardial Peak (s^{-1})	-4.4+/-2.3	-4.0+/-1.4
p-value	p=NS	p=NS

Discussion

This study presents methodology and illustrates the feasibility of computing radial strain and SR within the myocardium from PCMR tissue velocity data. Peak strain values computed from PCMR velocity data showed excellent agreement with peak transmural strain measurements from contours drawn on cine SSFP images acquired at the same myocardial location. The excellent spatial resolution of the acquired PCMR velocity data allowed for a distinction between transmural, endocardial and epicardial values. Endocardial-epicardial gradients were observed in both peak strain and SR values.

Comparison to Previously Published Values

Values of peak radial strain measured with TDI have ranged from 18 to 48%, with the average being around 36%[109,165-167]. The average value of peak transmural strain reported in the present study was 39.6 +/- 8.9%, which is in agreement with the mean of previously reported values[166,167].

Peak radial SR values of between 1.6 and 3.09 s^{-1} during systole and between -3.6 and -7.0s^{-1} during early diastole have been reported in the literature[109,147,165-167]. Peak radial SR in this study during systole (3.05+/-1.08 s^{-1}) and early diastole (-4.19+/-1.73s^{-1}) was within the previously published range.

Endocardial- Epicardial Strain Gradient

We observed peak radial strain values to be significantly larger in the endocardium than in the epicardium. The presence of an endocardial-epicardial strain gradient has previously been observed in the myocardium, both in animal models and in human studies[168-172]. However, the present study is the first to document the presence of a *radial* endocardial-epicardial strain gradient in human subjects.

Tagged MRI data has previously shown that the magnitude of peak endocardial *principal* strain is an average of 13+/-9% ($p<0.05$) greater than the magnitude of peak epicardial *principal* strain in open-chested dogs(endocardial=-24+/-7%, epicardial=-11+/-7%)[168]. In a close-chested canine study, the endocardium showed approximately twice as much *radial* strain as the epicardium(43.3% vs. 25.5%, $p<0.001$)[169]. In open-chested pigs, a linear relationship was demonstrated between transmural location and peak *radial* strain during ejection, with endocardial values greater than epicardial values[170].

Although no data is available on the presence of a radial strain gradient across the myocardium in human subjects, cross-fiber shortening in normal human hearts has repeatedly been shown to have a steep transmural gradient, with endocardial values being greater than epicardial values[171,172]. Although cross-fiber shortening describes strain along a different direction than radial strain (radial strain refers to strain in a myocardial coordinate system, while cross-fiber strain refers to a direction perpendicular to the orientation of the individual myocardial fibers[169]), a relationship has previously been established between cross-fiber strain and total wall thickening[169]. However, care must be taken when interpreting these results, as Rademakers et al established that cross-fiber strain and wall thickening were related, but the quantitative relationship between them was not determined.

Endocardial- Epicardial SR Gradient

This is the first study to demonstrate the presence of a *radial SR* gradient in the myocardium. SR is arguably a more sensitive marker of cardiac function than strain, more closely reflecting the underlying myocardial contractility. In addition, only SR (and not strain) has been shown to be load-independent[173]. During dobutamine infusion, increases in SR are seen before increases in strain[105], and SR has proven to be more sensitive at differentiating between reversible and non-reversible injury following ischemia[105].

A SR gradient between endocardial, epicardial, and midwall locations has been reported in the *longitudinal* direction of sheep. TDI showed that endocardial SR values were larger than midwall values, and that midwall values were larger than epicardial values (peak endo=-3.4+/-2.2, peak mid=-1.8+/-1.5, peak epi=-0.63+/-1.0)[108]. A transmural gradient of *scalar* SR values has also been documented across the myocardium in healthy human subjects during systole: peak endocardial values were roughly double peak epicardial values (endo=1.0s^{-1}, epi= 1.5-2.0s^{-1})[174].

Other SR Measurement Methods

Both strain and SR can be computed via a number of different methods, including TDI velocity data, echocardiographic speckle tracking, tagged MRI, or displacement encoded (DENSE) MRI[97,175-177]. However, each of these methods has its own set of drawbacks. Strain computation from TDI velocity data has problems with limited acoustic windows and is highly dependent on sonographer skill. In addition, radial strain is difficult to obtain throughout the entire myocardium due to near-field effects. The spatial resolution of tag lines in MRI tissue tagging is often insufficient for more than one tag intersection within the myocardial wall, and T1 relaxation causes tag fading in the later parts of the cardiac cycle.

The method for radial myocardial strain computation presented in this paper is based on PCMR velocity data. PCMR has many of the same advantages as DENSE imaging: information is available throughout the entire myocardium and throughout the entire cardiac cycle. In DENSE, the phase of the MR signal is used to encode position. Strain is then computed as a derivative of length, and SR is calculated as an additional derivative of the strain values. The two derivates may exacerbate noise and may require additional filtering or averaging over large regions. With PCMR, the phase of the MR signal is used to encode velocity, rather than position. SR is computed as a single spatial derivative of velocity, and strain values are obtained by integrating the SR data. In theory, strain and SR values computed with PCMR may be less susceptible to noise than DENSE measurements. Future work will involve a direct comparison of strain and SR measurements made with PCMR and DENSE.

In this study we chose to subdivide the myocardium into two regions (endocardial and epicardial), but it is possible to divide the myocardial wall into even small units and compute strain independently in each one, such as endocardial, midwall, and epicardial locations. The choice of subdivisions will be limited by pixel size and myocardial thickness.

PCMR methods to determine strain and SR have been previously suggested. Zhu et al. developed an accurate and reproducible strain computation method based on fitting tissue tracking results to a local deformation model[178]. Results from human data showed that maximum principal strain was dependent on radial location. The SR computation method presented in this paper differs from that presented by Zhu et al. in several ways. First, tissue tracking is not employed, so the computed strain values are Eulerian and not Lagrangian. In addition, the current method does not employ a model-fit, so no *a priori* knowledge about the LV is required. Arai et al. developed another method for computing SR from PCMR velocity data on a pixel-by-pixel basis[147]. The method required the application of a rigid-body motion correction scheme to the underlying velocity data which eliminated the gross heart translations and rotations of the chest prior to the execution of the strain measurement algorithm. The method presented in our study uses velocity difference from multiple pixels along the radial direction to compute the SR value, and the method can be performed without the rigid body motion correction. SR values computed by Arai et al.(2.0+/-0.6sec^{-1} during systole and -1.4+/-0.6sec^{-1} during early diastole) were slightly lower than those reported in the present study, but a direct comparison cannot be made between the open-chested canine model employed by Arai et al. and the in-vivo human subjects in the present study.

Study Limitations

A limitation of this study was that we conducted our analysis only in the radial direction. Peak radial strain values are approximately twice the magnitude of peak longitudinal strain values[108], and peak radial SR are significantly larger than peak longitudinal SR values[109]. Therefore, the argument can be made that radial function is the most important component of cardiac contraction. It has been demonstrated that during ischemia, radial motion abnormalities are detectable before longitudinal or circumferential motion abnormalities[106]. Furthermore, it has been shown that radial dyssynchrony (defined as the standard deviation of time to peak strain in six basal segments) is associated with depressed LV function and that radial dyssynchrony greater than 130 msec is predictive of acute response to Cardiac Resynchronization Therapy[110,111]. Therefore, we limited our present analysis to the radial direction. However, it should be noted that the same methodology could be used to compute both longitudinal and circumferential strains, although for the computation of longitudinal strains, PCMR tissue velocity images would require acquisition of two-or four-chamber views with longitudinal velocity encoding.

Velocity data acquired with PCMR has poor temporal resolution compared to ultrasound studies. In order to keep errors in strain measurements below 5%, a minimum of between 66 and 75 frames per second has been recommended for studies which derive strain from velocity data[112,164]. The MRI technique utilized in this study acquired velocity data at~40 frames per second. Therefore, it is possible that MRI is underestimating peak strain values and that not all aspects of the strain curves are being correctly resolved. Unfortunately, at present it is not possible to further increase the temporal resolution of the image acquisition protocol and still acquire velocities within a single scan.

The strain computation method presented in this paper makes the assumption that the transmural velocity distribution in the myocardium is linear. It has been suggested that this is a good assumption in normal hearts[179], and the dV/dr plots in Figure 7.1C show that the assumption holds well for this study population. However, the linear assumption may not hold in heart failure patients and the accuracy of the method may decrease. Furthermore, the linear-fit assumption is an really a smoothing or de-noising technique and may affect the SR measurements.

During contraction the myocardium undergoes twisting and shear, but the radial location at which strain is computed remains fixed throughout the cardiac cycle. Therefore, the SR measurements derived for any given myocardial region are really an average of SR in the myocardial tissue that moved to that material point throughout the cardiac cycle. Because ultimately the strain and SR measurements are averaged into larger regions in accordance with the AHA model for segmentation, it is unclear if this additional averaging has a substantial affect on the final values.

Conclusions

In conclusion, we have presented a method for deriving radial strain and SR values from PCMR velocity data. Excellent agreement was demonstrated between peak strain measurements derived with the presented method and strain measurements computed independently from contours drawn on cine SSFP images. The methodology allows for the possibility of differentiating between transmural, endocardial and epicardial values. The presence of an endocardial-epicardial gradient was demonstrated for both strain and SR in healthy volunteers.

CHAPTER 8

CONCLUSIONS

Project Summary

The overall goal of this project was to develop a method for identifying dyssynchrony and selecting patients for CRT based on myocardial wall velocities acquired with Magnetic Resonance Phase Velocity Mapping (MR PVM). To that end, a database describing normal myocardial contraction was developed. The database was used as a reference against which to compare patient values and identify wall-motion abnormalities present in dyssynchrony.

The focus of the first specific aim was to develop the MRI image acquisition and post-processing protocol for myocardial tissue velocity images. Starting with an ECG-gated, segmented GRE phase contrast sequence, navigator echo gating placement, velocity interleaving, the velocity encoding value, use of reconstruction filters, rest slabs, and SENSE were all explored. The optimal protocol was determined to be a segment (3 lines of k-space per cardiac phase), ECG-gated sequence with velocity directions interleaved by heartbeat employing a trailing navigator, Venc of 30cm/s, no reconstruction filters, rest slabs, and no SENSE. Furthermore, post-processing software for removing background phase correction, tissue tracking, and image standardization was developed.

Specific aim 2 used a myocardial motion phantom to verify the accuracy of the MR PVM sequence and optimize the acquisition parameters for myocardial tissue imaging. Excellent correlation was observed between expected and true motion (0.90 for longitudinal velocity and 0.93 for circumferential velocity). Mean difference between measured and true velocity throughout the entire cardiac cycle was -0.15+/-2.8cm/s in the longitudinal direction and 0.06+/-1.38 cm/s in the circumferential direction. MR PVM accurately detected the timing of peak velocities (mean $\text{diff}_{\text{measured-true}}$= 9.4+/-24.4msec in the longitudinal direction and 1.0+/-20.3msec in the circumferential direction), but slightly overestimated the magnitude of peak velocities (mean $\text{diff}_{\text{measured-true}}$=1.0+/-0.9cm/s in the longitudinal direction and of 3.2+/-1.9cm/s in the circumferential direction). A strong relationship was observed between temporal resolution and tracking accuracy (RMSE= 0.04*temp res + 0.32, R^2=0.91), while the effects of spatial resolution on tracking accuracy were not as strong (RMSE= -0.08*spatial resolution+1.66, R^2=0.18). Based on these results, it was concluded that 1) MR PVM can accurately measure myocardial velocities, and 2) high temporal resolution is much more important for tracking accuracy than high spatial resolution.

The purpose of specific aim 3 was to compare longitudinal myocardial velocities acquired with the optimized MR PVM sequence to Tissue Doppler Imaging, the clinical gold standard for measuring myocardial tissue velocities. The analysis was conducted in 10 normal volunteers and 10 heart failure patients scheduled for CRT. Excellent correlation was observed between myocardial tissue velocities measured with MR PVM and TDI, both in the normal volunteers (R=0.88) and the heart failure patients (R=0.75). Similar to the results from the phantom, MR PVM slightly overestimated peak velocities

(TDI=0.59*MR+0.3, R=0.96; mean $\text{diff}_{\text{MR-TDI}}$=4.35+/-3.7cm/s), but was accurate in measuring the timing of peak velocities (TDI=0.96*MR+0.02, R=0.07; mean $\text{diff}_{\text{MR-TDI}}$=5 msec+/-44msec). Reproducibility was comparable for MR PVM and TDI in measuring both peak velocity and time-to-peak velocity. The main conclusion from this specific aim was that MR PVM can be used to measure *in-vivo* myocardial tissue velocities in normal subjects and dyssynchrony patients.

The goal of specific aim 4 was to construct a database describing the normal myocardial contraction pattern in a group of healthy volunteers. Databases describing four parameters of the normal myocardial contraction pattern (peak systolic velocity, peak diastolic velocity, time-to-peak systolic velocity, and time-to-peak diastolic velocity) were constructed from a group of ten normal volunteers. Databases were constructed using both tracked and non-tracked velocity data, and it was determined that the choice of velocity data did not have a major affect on the value of the database parameters. Velocity data was also acquired in eight heart failure patients prior to CRT implantation, and patient values were compared to the normal databases, both on an individual patient basis and as a group. Systolic dyssynchrony values (SLD and $T_{\text{SD-12}}$) were computed for both the normal and patient populations. Significantly higher ($p<0.05$) levels of dyssynchrony were detected in the patient population for both dyssynchrony parameters. The normal database developed in this specific aim can be used as a reference against which to compare patient values and identify potential markers of dyssynchrony.

The goals of specific aim 5 were 1) to develop a technique for measuring radial strain and strain rate (SR) from MR PVM tissue velocity data, and 2) to evaluate differences in radial strain and SR between the endocardial and epicardial layers of the myocardium. Peak transmural strain values computed with the developed method were compared to peak strain values derived from contours drawn on cine SSFP. Excellent agreement between the two methods (peak $\varepsilon_{\text{cine SSFP}}$=38.1+/- 5.4%, peak $\varepsilon_{\text{MR PVM}}$= 38.0+/- 6.2%, p=NS) was observed in a group of 10 normal volunteers. Furthermore, the developed methodology allows for the possibility of differentiating between transmural, endocardial and epicardial values, and the presence of an endocardial-epicardial gradient was demonstrated for both strain and SR in the healthy volunteers.

Clinical Implications

The overall goal of this project was to develop a screening method based on MR PVM velocity data to identify myocardial motion abnormalities present in dyssynchrony. The work presented in this thesis provides a vital preliminary step towards this goals, as this project demonstrates the feasibility of using the MR PVM technique to measure myocardial motion in-vivo in both normal volunteers and heart failure patients prior to receiving CRT. The normal databases constructed in aim 4 can be used as a starting point for identifying differences in myocardial motion parameters between responders and non-responders and predicting response to CRT prior to device implantation.

Suggestions for Further Work

Combining MR PVM data with delayed-enhancement imaging

Information from delayed enhancement gadolinium imaging, which can identify the presence, location, and transmurality of scar burden following myocardial infarct, could be combined with MR PVM data to provide a more complete description of myocardial function. Recent research has shown that a larger scar burden and fewer viable myocardial segments are predicative of non-response to CRT[27,30-35]; the combination of MR PVM and gadolinium enhancement could help identify patients unlikely to respond to CRT.

When patient values were individually compared to the normal database in this project, time-to-peak systolic velocity in the radial direction for patient 1 did not show any delayed regions (areas in which patient values were more than two standard deviations away from the normal mean). This was an unexpected finding, as the heart failure of patient 1 was known to be ischemic in origin and an inferior wall infarct had previously been documented. However, a Bulls-eye plot of time-to-peak systolic radial velocity for just patient 1 showed a region of delayed systolic contraction in the inferior wall. The delayed region correlated well with the infracted area, which was seen as an area of decreased myocardial thickness, Figure 8.1. In the figure, the white arrows indicate the orientation of the anterior RV insertion point and the white asterick indicates the area of infarction or delayed contraction.

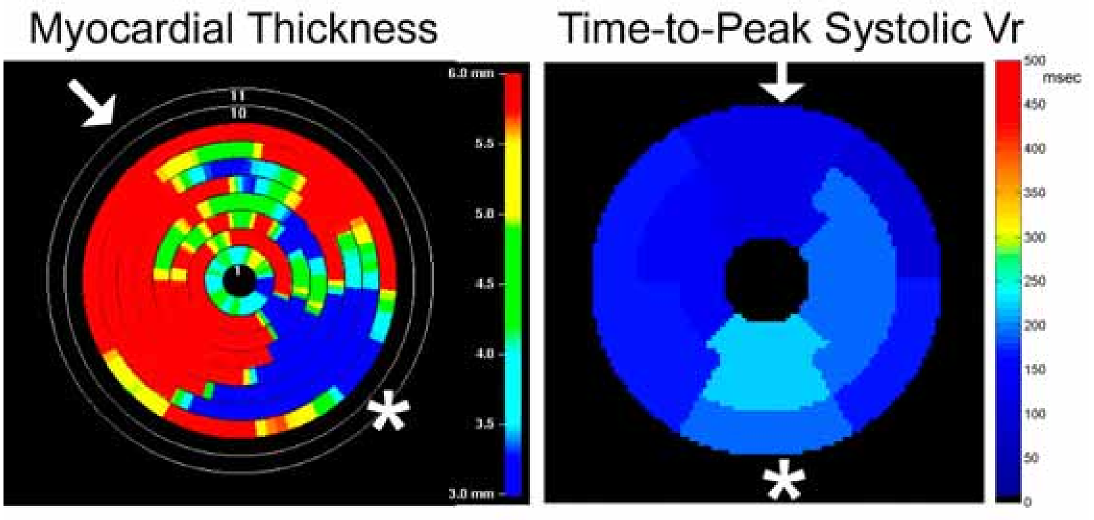

Figure 8.1: Agreement between myocardial thickness and delayed time-to-peak in patient 1.

Although this was the area with the greatest delay, it would not be a suitable location for a pacing lead, as the myocardial thickness map suggests that it is an infracted region. The combination of the scar map and the time-to-peak velocity map of the myocardium suggest that the lateral wall—in which time-to-peak is only slightly delayed, but which does not have transmural scar burden—would be a more suitable pacing site. Information from both the time-to-peak map and the scar map are needed to make this conclusion.

Cross-Correlation Delay with MR PVM velocity data

The databases for quantifying normal cardiac function and identifying dyssynchrony presented in this work are based on a "time-to-peak" analysis. While this analysis has been used extensively to identify dyssynchrony[75,151], it suffers from the significant drawback that only a single point from the entire velocity curve in each myocardial segment is utilized in the analysis. At the temporal resolution used for the acquisition of MR PVM velocity data, only one of approximately 30 points throughout the cardiac cycle is used, meaning that over 90% of the collected data is not used in the analysis.

Our lab has developed a mathematical method to quantify dyssynchrony based on data collected *throughout* the cardiac cycle (not just peak values). The method uses a cross-correlation (XC) function to calculate a temporal delay between two myocardial tissue velocity profiles. Some preliminary data suggests that the XC delay between two velocity curves would provides a more accurate measure of dyssynchrony and may be better able to separate subjects with dyssynchrony from normal volunteers than methods based on “times-to-peak” analysis[180].

For example, the normal volunteer shown in Figure 6.14 was identified as having dyssynchronous contraction based on a septal-to-lateral delay of 132msec and a TSD-12 value of 73msec. Inspection of the velocity curves from the septal and lateral walls, however, clearly shows that this volunteer does not have any dyssynchrony. The XC delay was able to correctly classify this volunteer as normal, as the XC delay between the septal and lateral walls in the basal slice was calculated to be 0msec.

Future work could focus on developing a database of the normal XC delay and determining if the XC delay could be utilized to identify dyssynchrony patients and separate clinical CRT responders and non-responders.

Final Thoughts

Predicting which patients will benefit from CRT is a complex and difficult issue, as response to CRT is not only mediated by the underlying mechanical dyssynchrony in the myocardial wall, but also other factors such as lead position, heart failure progression, and the location of myocardial infarct scars. Therefore, at best, this project can only address one of the many underlying factors affecting response to CRT. However, it is hoped that the MR imaging protocol and the normal database developed in this project will provide useful insights into normal myocardial contraction and can one day be part of a tool used to more specifically identify patients suitable for CRT.

APPENDIX A

NORMAL DATABASE FROM NON-TRACKED VELOCITY DATA

The non-tracked database was constructed in an identical manner to the tracked database described in Chapter 6, but with the exception that the data was not input into the tracking algorithm. In other words, this database is constructed from MR PVM velocity data as it appears directly from the scanner (although background phase correction was still applied).

The non-tracked database had essentially the same features as the tracked database. For peak velocity measurements, values were similar (Table X), and the standard deviation across the ten normal volunteers was low in both databases. Furthermore, both databases showed a difference in the magnitude of peak contraction velocity between the septal and the lateral walls (with velocity magnitude in the lateral wall being larger).

Time-to-peak velocity measurements were also nearly identical between the tracked and non-tracked databases. The non-tracked database showed slightly higher standard deviation for measurements of time-to-peak longitudinal systolic velocity, while the tracked database had a slightly higher standard deviation for measurements of time-to-peak longitudinal diastolic velocity, mainly within the apical regions.

Table A.1: Peak velocity database from non-tracked data

AHA Segment #		**Time-to-Peak Systolic Velocity** (msec after R-wave detection)			**Time-to-Peak Diastolic Velocity** (msec after R-wave detection)		
		Vr	**Vc**	**Vz**	**Vr**	**Vc**	**Vz**
Basal Slice	1	5.1+/-1.0	2.3+/-1.1	4.6+/-1.5	-7.0+/-1.8	-2.3+/-1.1	-10.9+/-2.1
	2	3.3+/-1.2	3.0+/-1.1	3.9+/-0.7	-4.2+/-1.5	-2.3+/-1.4	-10.3+/-1.8
	3	2.5+/-0.8	3.8+/-1.2	4.5+/-0.9	-5.5+/-2.2	-3.2+/-1.2	-10.1+/-1.9
	4	3.5+/-1.3	3.5+/-1.1	6.9+/-1.8	-6.8+/-1.3	-4.1+/-1.3	-11.7+/-3.0
	5	4.0+/-1.2	3.2+/-1.3	7.9+/-2.0	-7.4+/-1.1	-3.7+/-1.3	-14.9+/-3.8
	6	4.2+/-0.6	3.1+/-1.1	6.9+/-1.7	-8.5+/-1.5	-3.8+/-1.2	-14.2+/-2.7
Middle Slice	7	3.5+/-0.5	1.2+/-0.8	3.8+/-1.6	-6.2+/-1.7	-1.7+/-1.2	-7.4+/-2.0
	8	2.8+/-0.7	2.1+/-1.0	3.3+/-1.3	-5.7+/-1.7	-2.1+/-0.8	-7.1+/-2.3
	9	3.1+/-0.9	2.2+/-0.9	4.1+/-1.2	-5.7+/-1.4	-2.0+/-0.7	-6.4+/-2.0
	10	3.5+/-1.3	1.1+/-0.7	5.9+/-1.6	-5.7+/-1.5	-2.5+/-0.6	-7.9+/-2.7
	11	3.5+/-1.1	0.8+/-0.9	6.7+/-1.5	-7.0+/-1.3	-1.7+/-0.8	-10.3+/-2.3
	12	4.2+/-1.2	1.9+/-1.9	5.8+/-1.6	-6.7+/-1.5	-2.1+/-1.5	-9.6+/-2.1
Apical Slice	13	2.3+/-1.1	-4.7+/-1.6	2.7+/-1.0	-5.2+/-1.7	4.0+/-1.3	-3.8+/-1.9
	14	2.5+/-0.9	-3.0+/-1.7	1.8+/-0.9	-4.5+/-2.2	1.8+/-0.8	-2.7+/-1.6
	15	4.6+/-1.3	-1.9+/-1.5	3.7+/-1.4	-5.1+/-1.5	2.9+/-1.2	-3.9+/-1.8
	16	4.2+/-1.6	-2.9+/-1.0	5.3+/-1.4	-6.1+/-1.7	3.5+/-1.9	-6.1+/-2.1

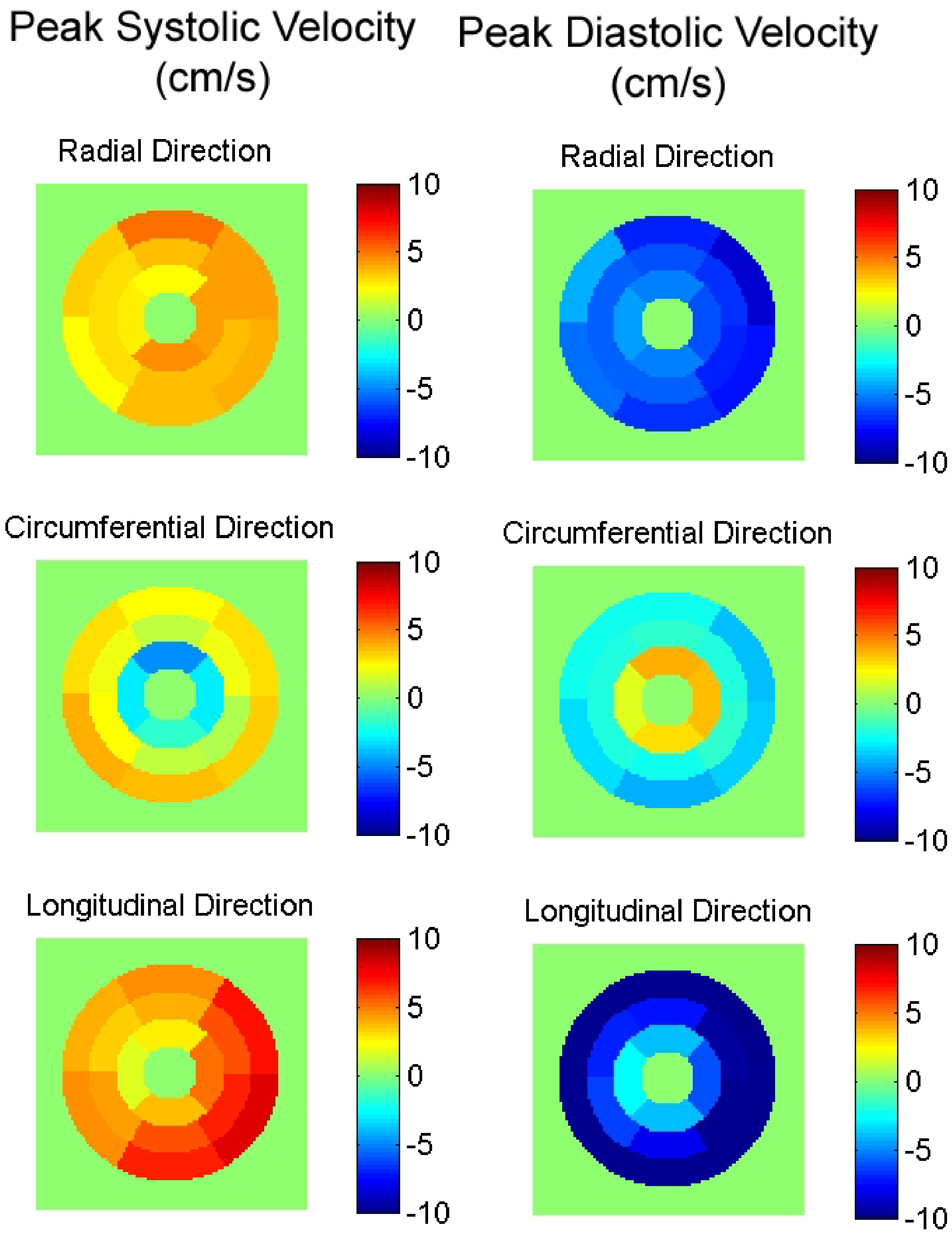

Figure A.1: Peak Velocity Database from non-tracked data

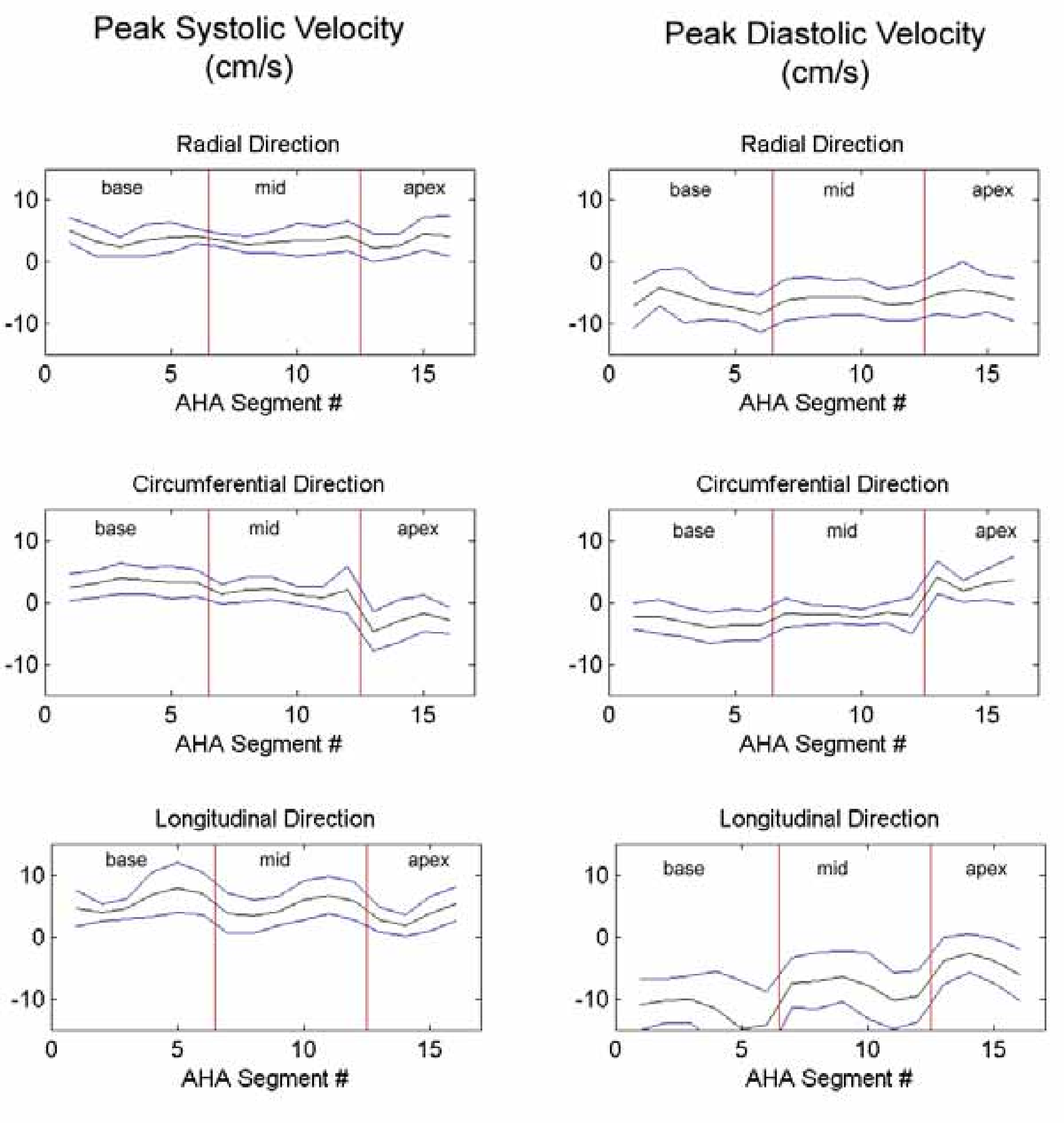

Figure A.2: Mean +/-2std of peak velocity in non-tracked database

Table A.2: Time-to-peak velocity database from non-tracked data

AHA Segment #		Time-to-Peak Systolic Velocity (msec after R-wave detection)			Time-to-Peak Diastolic Velocity (msec after R-wave detection)		
		Vr	**Vc**	**Vz**	**Vr**	**Vc**	**Vz**
Basal Slice	1	120.7+/-38.0	177.2+/-36.8	151.6+/-61.1	490.4+/-60.1	585.8+/-138.8	508.5+/-33.0
	2	131.1+/-46.5	195.2+/-59.7	184.9+/-60.8	531.6+/-91.4	531.8+/-85.9	511.0+/-35.4
	3	182.0+/-47.5	190.2+/-52.8	164.4+/-68.0	549.8+/-42.4	439.6+/-57.4	503.4+/-35.0
	4	174.5+/-41.2	201.0+/-34.1	105.2+/-41.4	488.1+/-39.0	449.4+/-67.6	500.8+/-34.0
	5	179.7+/-59.6	187.6+/-47.6	92.4+/-15.9	477.7+/-35.1	472.5+/-76.5	503.4+/-35.0
	6	156.7+/-39.3	172.3+/-47.4	100.1+/-18.5	480.2+/-35.4	498.1+/-54.6	505.9+/-33.1
Middle Slice	7	154.4+/-49.1	221.0+/-64.7	131.4+/-81.9	521.3+/-37.6	573.1+/-179.9	518.8+/-32.3
	8	174.8+/-47.4	154.0+/-57.1	174.3+/-76.0	536.7+/-42.2	542.5+/-116.8	508.5+/-36.2
	9	184.7+/-24.6	179.8+/-37.1	146.0+/-57.2	536.8+/-29.3	547.2+/-108.1	511.4+/-34.3
	10	187.4+/-43.8	187.6+/-64.5	95.0+/-17.1	511.0+/-40.7	521.3+/-83.6	498.2+/-37.6
	11	200.2+/-64.3	164.6+/-65.1	92.4+/-15.9	498.2+/-40.9	564.6+/-90.1	518.7+/-42.9
	12	136.0+/-54.9	192.9+/-86.3	95.0+/-16.9	505.9+/-33.1	575.8+/-134.1	505.9+/-33.8
Apical Slice	13	151.9+/-53.8	110.2+/-36.3	92.4+/-10.6	524.0+/-37.2	436.4+/-56.6	503.4+/-29.6
	14	184.8+/-32.5	141.4+/-69.5	201.3+/-109.1	560.1+/-48.4	523.7+/-138.3	539.4+/-65.3
	15	174.5+/-29.1	174.7+/-89.7	92.5+/-10.9	537.1+/-41.5	585.0+/-100.0	495.6+/-38.7
	16	138.6+/-66.4	118.1+/-52.1	95.0+/-16.9	516.2+/-37.6	454.6+/-109.4	500.7+/-40.4

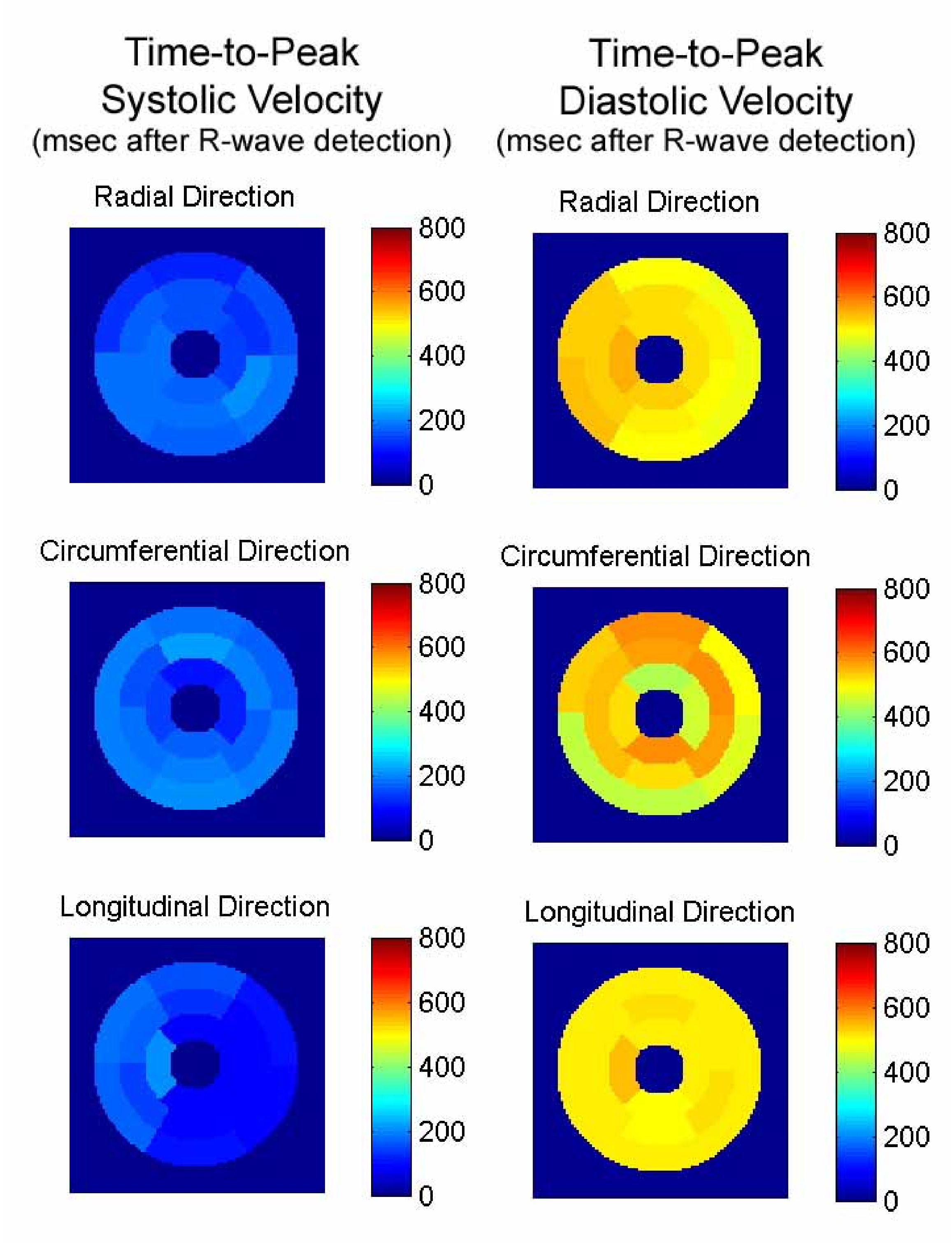

Figure A.3 Time-to-peak velocity database from non-tracked data

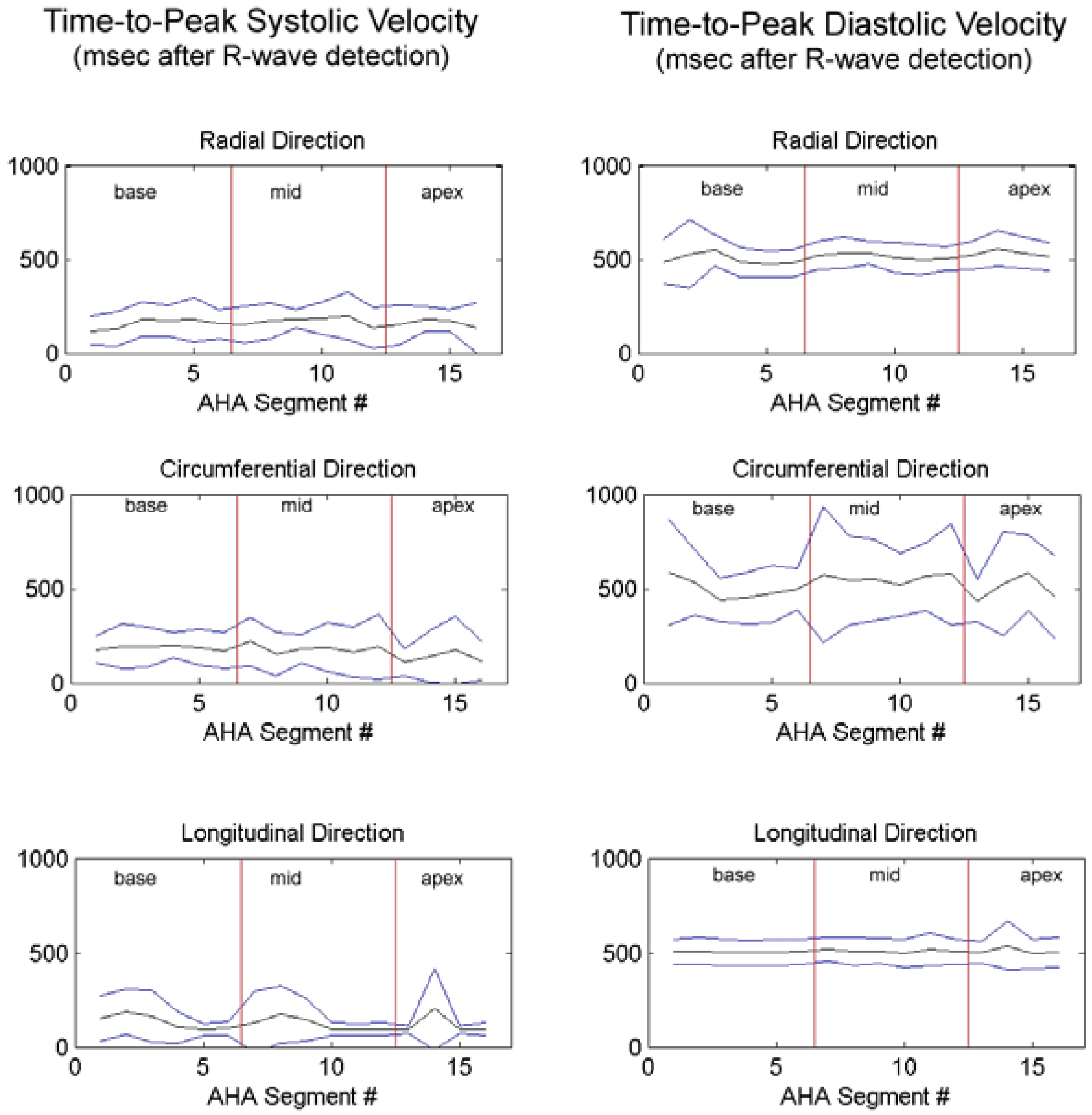

Figure A.4 Mean +/-2std of time-to-peak velocity in non- tracked database

REFERENCES

1. (AHA) AHA. Heart Disease and Stroke Statistics - 2004 Update. In. Dallas, Texas: American Heart Association; 2004:http://www.americanheart.org/downloadable/heart/1072969766940HSStats2004Update.pdf.
2. Abraham WT, Fisher WG, Smith AL, Delurgio DB, Leon AR, Loh E, Kocovic DZ, Packer M, Clavell AL, Hayes DL, Ellestad M, Trupp RJ, Underwood J, Pickering F, Truex C, McAtee P, Messenger J. Cardiac resynchronization in chronic heart failure. *N Engl J Med*. 2002;346:1845-1853.
3. Trautmann SI, Kloss M, Auricchio A. Cardiac resynchronization therapy. *Curr Cardiol Rep*. 2002;4:371-8.
4. Kass DA. Ventricular resynchronization: pathophysiology and identification of responders. *Rev Cardiovasc Med*. 2003;4 Suppl 2:S3-S13.
5. Sogaard P, Egeblad H, Kim WY, Jensen HK, Pedersen AK, Kristensen BO, Mortensen PT. Tissue Doppler imaging predicts improved systolic performance and reversed left ventricular remodeling during long-term cardiac resynchronization therapy. *J Am Coll Cardiol*. 2002;40:723-30.
6. Nelson GS, Berger RD, Fetics BJ, Talbot M, Spinelli JC, Hare JM, Kass DA. Left ventricular or biventricular pacing improves cardiac function at diminished energy cost in patients with dilated cardiomyopathy and left bundle-branch block. *Circulation*. 2000;102:3053-9.
7. Medtronic. Press Release: Medtronic Announces FDA Approval of InSync Marquis Cardiac Resynchronization Therapy System. In; 2003.
8. USFDA. New Device Approval - Guidant Cardiac Resynchronization Therapy Defibrillator System including the CONTAK CD pluse generator and the EASYTRAK left ventricular coronary venous lead. In; 2002.
9. Abraham WT. Cardiac resynchronization therapy: a review of clinical trials and criteria for identifying the appropriate patient. *Rev Cardiovasc Med*. 2003;4 Suppl 2:S30-S37.
10. Zardini M, Tritto M, Bargiggia G, Forzani T, Santini M, Perego GB, Bocchiardo M, Raviele A, Salerno-Uriarte JA. The InSync Italian Registry: analysis of clinical outcome and considerations on the selection of candidates to left ventricular resynchronization. *European Heart Journal Supplements*. 2000;2:J16-J22.
11. Porciani MC, Puglisi A, Colella A, Peraldo C, Gaita F, Romano M, Pistis G, Curnis A, Sabini A, Musilli N, Padeletti L. Echocardiographic evaluation of the effect of biventricular pacing: the InSync Italian Registry. *European Heart Journal Supplements*. 2000;2:J23-J30.
12. Ricci R, Ansalone G, Toscano S, Pignalberi C, Lunati M, Gasparini M, Padeletti L, Disertori M, Ravazzi PA, Santini M. Cardiac Resynchronization: materials, technique and results. The InSync Italian Registry. *European Heart Journal Supplements*. 2000;2:J6-J15.
13. St John Sutton MG, Plappert T, Abraham WT, Smith AL, DeLurgio DB, Leon AR, Loh E, Kocovic DZ, Fisher WG, Ellestad M, Messenger J, Kruger K, Hilpisch KE, Hill MR. Effect of cardiac resynchronization therapy on left

ventricular size and function in chronic heart failure. *Circulation*. 2003;107:1985-90.

14. Bristow MR, Feldman AM, Saxon LA. Heart failure management using implantable devices for ventricular resynchronization: Comparison of Medical Therapy, Pacing, and Defibrillation in Chronic Heart Failure (COMPANION) trial. COMPANION Steering Committee and COMPANION Clinical Investigators. *J Card Fail*. 2000;6:276-285.
15. Kerwin WF, Botvinick EH, O'Connell JW, Merrick SH, DeMarco T, Chatterjee K, Scheibly K, Saxon LA. Ventricular contraction abnormalities in dilated cardiomyopathy: effect of biventricular pacing to correct interventricular dyssynchrony. *J Am Coll Cardiol*. 2000;35:1221-7.
16. Abraham WT. Cardiac resynchronization therapy for heart failure: biventricular pacing and beyond. *Curr Opin Cardiol*. 2002;17:346-352.
17. Nishimura RA, Hayes DL, Holmes DR, Jr., Tajik AJ. Mechanism of hemodynamic improvement by dual-chamber pacing for severe left ventricular dysfunction: an acute Doppler and catheterization hemodynamic study. *J Am Coll Cardiol*. 1995;25:281-8.
18. Yu CM, Chau E, Sanderson JE, Fan K, Tang MO, Fung WH, Lin H, Kong SL, Lam YM, Hill MR, Lau CP. Tissue Doppler echocardiographic evidence of reverse remodeling and improved synchronicity by simultaneously delaying regional contraction after biventricular pacing therapy in heart failure. *Circulation*. 2002;105:438-445.
19. Lindner O, Vogt J, Kammeier A, Wielepp P, Holzinger J, Baller D, Lamp B, Hansky B, Korfer R, Horstkotte D, Burchert W. Effect of cardiac resynchronization therapy on global and regional oxygen consumption and myocardial blood flow in patients with non-ischaemic and ischaemic cardiomyopathy. *Eur Heart J*. 2005;26:70-6.
20. Rouleau F, Merheb M, Geffroy S, Berthelot J, Chaleil D, Dupuis JM, Victor J, Geslin P. Echocardiographic assessment of the interventricular delay of activation and correlation to the QRS width in dilated cardiomyopathy. *Pacing Clin Electrophysiol*. 2001;24:1500-6.
21. Auricchio A, Stellbrink C, Sack S, Block M, Vogt J, Bakker P, Mortensen P, Klein H. The Pacing Therapies for Congestive Heart Failure (PATH-CHF) study: rationale, design, and endpoints of a prospective randomized multicenter study. *Am J Cardiol*. 1999;83:130D-135D.
22. Lecoq G, Leclercq C, Leray E, Crocq C, Alonso C, de Place C, Mabo P, Daubert C. Clinical and electrocardiographic predictors of a positive response to cardiac resynchronization therapy in advanced heart failure. *Eur Heart J*. 2005.
23. Molhoek SG, L VANE, Bootsma M, Steendijk P, Van Der Wall EE, Schalij MJ. QRS duration and shortening to predict clinical response to cardiac resynchronization therapy in patients with end-stage heart failure. *Pacing Clin Electrophysiol*. 2004;27:308-13.
24. Bax JJ, Bleeker GB, Marwick TH, Molhoek SG, Boersma E, Steendijk P, van der Wall EE, Schalij MJ. Left ventricular dyssynchrony predicts response and prognosis after cardiac resynchronization therapy. *J Am Coll Cardiol*. 2004;44:1834-40.

25. Auricchio A, Ding J, Spinelli JC, Kramer AP, Salo RW, Hoersch W, KenKnight BH, Klein HU. Cardiac resynchronization therapy restores optimal atrioventricular mechanical timing in heart failure patients with ventricular conduction delay. *J Am Coll Cardiol*. 2002;39:1163-1169.
26. Lunati M, Paolucci M, Oliva F, Frigerio M, Magenta G, Cattafi G, Vecchi R, Vicini I, Cavaglia S. Patient selection for biventricular pacing. *J Cardiovasc Electrophysiol*. 2002;13:S63-7.
27. Reuter S, Garrigue S, Barold SS, Jais P, Hocini M, Haissaguerre M, Clementy J. Comparison of characteristics in responders versus nonresponders with biventricular pacing for drug-resistant congestive heart failure. *Am J Cardiol*. 2002;89:346-50.
28. Oguz E, Dagdeviren B, Bilsel T, Akdemir O, Erdinler I, Akyol A, Ulufer T, Tezel T, Gurkan K. Echocardiographic prediction of long-term response to biventricular pacemaker in severe heart failure. *Eur J Heart Fail*. 2002;4:83-90.
29. Pitzalis MV, Iacoviello M, Romito R, Massari F, Rizzon B, Luzzi G, Guida P, Andriani A, Mastropasqua F, Rizzon P. Cardiac resynchronization therapy tailored by echocardiographic evaluation of ventricular asynchrony. *J Am Coll Cardiol*. 2002;40:1615-1622.
30. Adelstein EC, Saba S. Scar burden by myocardial perfusion imaging predicts echocardiographic response to cardiac resynchronization therapy in ischemic cardiomyopathy. *Am Heart J*. 2007;153:105-12.
31. Bleeker GB, Kaandorp TA, Lamb HJ, Boersma E, Steendijk P, de Roos A, van der Wall EE, Schalij MJ, Bax JJ. Effect of posterolateral scar tissue on clinical and echocardiographic improvement after cardiac resynchronization therapy. *Circulation*. 2006;113:969-76.
32. Bleeker GB, Schalij MJ, Van Der Wall EE, Bax JJ. Postero-lateral scar tissue resulting in non-response to cardiac resynchronization therapy. *J Cardiovasc Electrophysiol*. 2006;17:899-901.
33. White JA, Yee R, Yuan X, Krahn A, Skanes A, Parker M, Klein G, Drangova M. Delayed enhancement magnetic resonance imaging predicts response to cardiac resynchronization therapy in patients with intraventricular dyssynchrony. *J Am Coll Cardiol*. 2006;48:1953-60.
34. Ypenburg C, Roes SD, Bleeker GB, Kaandorp TA, de Roos A, Schalij MJ, van der Wall EE, Bax JJ. Effect of total scar burden on contrast-enhanced magnetic resonance imaging on response to cardiac resynchronization therapy. *Am J Cardiol*. 2007;99:657-60.
35. Ypenburg C, Schalij MJ, Bleeker GB, Steendijk P, Boersma E, Dibbets-Schneider P, Stokkel MP, van der Wall EE, Bax JJ. Impact of viability and scar tissue on response to cardiac resynchronization therapy in ischaemic heart failure patients. *Eur Heart J*. 2007;28:33-41.
36. Fauchier L, Babuty D, Cosnay P, Fauchier JP. Cardiac resynchronization in chronic heart failure: some considerations about the cost-effectiveness.[comment]. *European Heart Journal*. 2003;24:879; author reply 879.
37. Leclercq C, Hare JM. Ventricular resynchronization: current state of the art. *Circulation*. 2004;109:296-9.

38. Bakker PF, Meijburg HW, de Vries JW, Mower MM, Thomas AC, Hull ML, Robles De Medina EO, Bredee JJ. Biventricular pacing in end-stage heart failure improves functional capacity and left ventricular function. *J Interv Card Electrophysiol*. 2000;4:395-404.
39. Auricchio A, Stellbrink C, Sack S, Block M, Vogt J, Bakker P, Huth C, Schondube F, Wolfhard U, Bocker D, Krahnefeld O, Kirkels H. Long-term clinical effect of hemodynamically optimized cardiac resynchronization therapy in patients with heart failure and ventricular conduction delay. *J Am Coll Cardiol*. 2002;39:2026-2033.
40. Bleeker GB, Schalij MJ, Molhoek SG, Verwey HF, Holman ER, Boersma E, Steendijk P, Van Der Wall EE, Bax JJ. Relationship between QRS duration and left ventricular dyssynchrony in patients with end-stage heart failure. *J Cardiovasc Electrophysiol*. 2004;15:544-9.
41. Yu CM, Yang H, Lau CP, Wang Q, Wang S, Lam L, Sanderson JE. Regional left ventricle mechanical asynchrony in patients with heart disease and normal QRS duration: implication for biventricular pacing therapy. *Pacing Clin Electrophysiol*. 2003;26:562-570.
42. Gasparini M, Mantica M, Galimberti P, Marconi M, Genovese L, Faletra F, Simonini S, Klersy C, Coates R, Gronda E. Beneficial effects of biventricular pacing in patients with a "narrow" QRS. *Pacing Clin Electrophysiol*. 2003;26:169-74.
43. Leclercq C, Faris O, Tunin R, Johnson J, Kato R, Evans F, Spinelli J, Halperin H, McVeigh E, Kass DA. Systolic improvement and mechanical resynchronization does not require electrical synchrony in the dilated failing heart with left bundle-branch block. *Circulation*. 2002;106:1760-1763.
44. Bax JJ, Abraham T, Barold SS, Breithardt OA, Fung JW, Garrigue S, Gorcsan J, 3rd, Hayes DL, Kass DA, Knuuti J, Leclercq C, Linde C, Mark DB, Monaghan MJ, Nihoyannopoulos P, Schalij MJ, Stellbrink C, Yu CM. Cardiac resynchronization therapy: Part 1--issues before device implantation. *J Am Coll Cardiol*. 2005;46:2153-67.
45. Bax JJ, Ansalone G, Breithardt OA, Derumeaux G, Leclercq C, Schalij MJ, Sogaard P, St John Sutton M, Nihoyannopoulos P. Echocardiographic evaluation of cardiac resynchronization therapy: ready for routine clinical use? A critical appraisal. *J Am Coll Cardiol*. 2004;44:1-9.
46. Karwatowski SP, Mohiaddin RH, Yang GZ, Firmin DN, Sutton MSJ, Underwood SR, Longmore DB. Assessment of Regional Left Ventricular Motion with MR Velocity Mapping in Healthy Subjects. *Journal of Magnetic Resonance Imaging*. 1994;2:152-155.
47. Jones CJ, Raposo L, Gibson DG. Functional importance of the long axis dynamics of the human left ventricle. *Br Heart J*. 1990;63:215-20.
48. Karwatowski SP, Mohiaddin RH, Yang GZ, Firmin DN, St John Sutton M, Underwood SR. Regional myocardial velocity imaged by magnetic resonance in patients with ischaemic heart disease. *Br Heart J*. 1994;72:332-338.
49. Young AA, Kramer CM, Ferrari MD, Axel L, Reichek N. Three Dimensional Left Ventricular Deformation in Hypertrophic Cardiomyopathy. *Circulation*. 1994;90:854-867.

50. Maier SE, Fischer SE, McKinnon GC, Hess OM, Krayenbuehl HP, Boesiger P. Evaluation of left ventricular segmental wall motion in hypertrophic cardiomyopathy with myocardial tagging. *Circulation*. 1992;86:1919-28.
51. Young AA, Axel L. Three-dimensional motion and deformation of the heart wall: estimation with spatial modulation of magnetization--a model-based approach. *Radiology*. 1992;185:241-7.
52. Nagel E, Stuber M, Lakatos M, Scheidegger MB, Boesiger P, Hess OM. Cardiac rotation and relaxation after anterolateral myocardial infarction. *Coron Artery Dis*. 2000;11:261-7.
53. Markl M, Schneider B, Hennig J, Peschl S, Winterer J, Krause T, Laubenberger J. Cardiac phase contrast gradient echo MRI: measurement of myocardial wall motion in healthy volunteers and patients. *Int J Card Imaging*. 1999;15:441-452.
54. Petitjean C, Rougon N, Cluzel P. Assessment of myocardial function: a review of quantification methods and results using tagged MRI. *J Cardiovasc Magn Reson*. 2005;7:501-16.
55. Hillenbrand HB, Lima JA, Bluemke DA, Beache GM, McVeigh ER. Assessment of myocardial systolic function by tagged magnetic resonance imaging. *J Cardiovasc Magn Reson*. 2000;2:57-66.
56. Lorenz CH, Pastorek JS, Bundy JM. Delineation of normal human left ventricular twist throughout systole by tagged cine magnetic resonance imaging. *J Cardiovasc Magn Reson*. 2000;2:97-108.
57. Young AA, Imai H, Chang CN, Axel L. Two-dimensional left ventricular deformation during systole using magnetic resonance imaging with spatial modulation of magnetization. *Circulation*. 1994;89:740-52.
58. Matter C, Nagel E, Stuber M, Boesiger P, Hess OM. Assessment of systolic and diastolic LV function by MR myocardial tagging. *Basic Res Cardiol*. 1996;91 Suppl 2:23-8.
59. Nagel E, Stuber M, Burkhard B, Fischer SE, Scheidegger MB, Boesiger P, Hess OM. Cardiac rotation and relaxation in patients with aortic valve stenosis. *Eur Heart J*. 2000;21:582-9.
60. Buchalter MB, Weiss JL, Rogers WJ, Zerhouni EA, Weisfeldt ML, Beyar R, Shapiro EP. Noninvasive quantification of left ventricular rotational deformation in normal humans using magnetic resonance imaging myocardial tagging. *Circulation*. 1990;81:1236-44.
61. Yun KL, Niczyporuk MA, Daughters GT, 2nd, Ingels NB, Jr., Stinson EB, Alderman EL, Hansen DE, Miller DC. Alterations in left ventricular diastolic twist mechanics during acute human cardiac allograft rejection. *Circulation*. 1991;83:962-73.
62. Rademakers FE, Buchalter MB, Rogers WJ, Zerhouni EA, Weisfeldt ML, Weiss JL, Shapiro EP. Dissociation Between Left Ventricular Untwisting and Filling Accentuation by Catecholamines. *Circulation*. 1992;85:1572-1581.
63. Beyar R, Yin FC, Hausknecht M, Weisfeldt ML, Kass DA. Dependence of left ventricular twist-radial shortening relations on cardiac cycle phase. *Am J Physiol*. 1989;257:H1119-26.
64. Pitzalis MV, Iacoviello M, Romito R, Massari F, Rizzon B, Luzzi G, Guida P, Andriani A, Mastropasqua F, Rizzon P. Cardiac resynchronization therapy

tailored by echocardiographic evaluation of ventricular asynchrony. *Journal of the American College of Cardiology*. 2002;40:1615-22.

65. Breithardt OA, Stellbrink C, Kramer AP, Sinha AM, Franke A, Salo R, Schiffgens B, Huvelle E, Auricchio A, Failure P-CSGPTfCH. Echocardiographic quantification of left ventricular asynchrony predicts an acute hemodynamic benefit of cardiac resynchronization therapy. *Journal of the American College of Cardiology*. 2002;40:536-45.
66. Kawaguchi M, Murabayashi T, Fetics BJ, Nelson GS, Samejima H, Nevo E, Kass DA. Quantitation of basal dyssynchrony and acute resynchronization from left or biventricular pacing by novel echo-contrast variability imaging. *Journal of the American College of Cardiology*. 2002;39:2052-8.
67. Kapetanakis S, Cooklin M, Monaghan MJ. Mechanical resynchronisation in biventricular pacing illustrated by real time transthoracic three dimensional echocardiography. *Heart (British Cardiac Society)*. 2004;90:482.
68. Galiuto L, Ignone G, DeMaria AN. Contraction and relaxation velocities of the normal left ventricle using pulsed-wave tissue Doppler echocardiography. *Am J Cardiol*. 1998;81:609-14.
69. Silva CE, Ferreira LD, Peixoto LB, Monaco CG, Gil MA, Ortiz J. Study of the myocardial contraction and relaxation velocities through Doppler tissue imaging echocardiography: A new alternative in the assessment of the segmental ventricular function. *Arq Bras Cardiol*. 2002;78:200-11.
70. Cardim N, Oliveria AG, Longo S, Ferreria R, Pereira A, Reis RP, Correria JM. Regional Myocardial Function in Healthy Adults. Assessment Through Tissue Doppler Echocardiography. *Arquivos brasileiros de cardiologia.* 2003;80:474-82.
71. Yu CM, Fung WH, Lin H, Zhang Q, Sanderson JE, Lau CP. Predictors of left ventricular reverse remodeling after cardiac resynchronization therapy for heart failure secondary to idiopathic dilated or ischemic cardiomyopathy. *Am J Cardiol*. 2003;91:684-688.
72. Sutherland GR, Kukulski T, Kvitting JE, D'Hooge J, Arnold M, Brandt E, Hatle L, Wranne B. Quantitation of left-ventricular asynergy by cardiac ultrasound. *Am J Cardiol*. 2000;86:4G-9G.
73. Ansalone G, Giannantoni P, Ricci R, Trambaiolo P, Laurenti A, Fedele F, Santini M. Doppler myocardial imaging in patients with heart failure receiving biventricular pacing treatment. *Am Heart J*. 2001;142:881-896.
74. Ansalone G, Giannantoni P, Ricci R, Trambaiolo P, Fedele F, Santini M. Doppler myocardial imaging to evaluate the effectiveness of pacing sites in patients receiving biventricular pacing. *J Am Coll Cardiol*. 2002;39:489-499.
75. Bax JJ, Marwick TH, Molhoek SG, Bleeker GB, van Erven L, Boersma E, Steendijk P, van der Wall EE, Schalij MJ. Left ventricular dyssynchrony predicts benefit of cardiac resynchronization therapy in patients with end-stage heart failure before pacemaker implantation. *Am J Cardiol*. 2003;92:1238-40.
76. Notabartolo D, Merlino JD, Smith AL, DeLurgio DB, Vera FV, Easley KA, Martin RP, Leon AR. Usefulness of the peak velocity difference by tissue Doppler imaging technique as an effective predictor of response to cardiac resynchronization therapy. *Am J Cardiol*. 2004;94:817-20.

77. Yu CM, Chau E, Sanderson JE, Fan K, Tang MO, Fung WH, Lin H, Kong SL, Lam YM, Hill MR, Lau CP. Tissue Doppler echocardiographic evidence of reverse remodeling and improved synchronicity by simultaneously delaying regional contraction after biventricular pacing therapy in heart failure. *Circulation*. 2002;105:438-45.
78. Yu CM, Lin H, Zhang Q, Sanderson JE. High prevalence of left ventricular systolic and diastolic asynchrony in patients with congestive heart failure and normal QRS duration. *Heart*. 2003;89:54-60.
79. Yu CM, Fung JW, Zhang Q, Chan CK, Chan YS, Lin H, Kum LC, Kong SL, Zhang Y, Sanderson JE. Tissue Doppler imaging is superior to strain rate imaging and postsystolic shortening on the prediction of reverse remodeling in both ischemic and nonischemic heart failure after cardiac resynchronization therapy. *Circulation*. 2004;110:66-73.
80. Yu CM, Zhang Q, Fung JW, Chan HC, Chan YS, Yip GW, Kong SL, Lin H, Zhang Y, Sanderson JE. A novel tool to assess systolic asynchrony and identify responders of cardiac resynchronization therapy by tissue synchronization imaging. *J Am Coll Cardiol*. 2005;45:677-84.
81. Sade LE, Kanzaki H, Severyn D, Dohi K, Gorcsan J, 3rd. Quantification of radial mechanical dyssynchrony in patients with left bundle branch block and idiopathic dilated cardiomyopathy without conduction delay by tissue displacement imaging. *Am J Cardiol*. 2004;94:514-8.
82. Sade LE, Severyn DA, Kanzaki H, Dohi K, Gorcsan J, 3rd. Second-generation tissue Doppler with angle-corrected color-coded wall displacement for quantitative assessment of regional left ventricular function. *Am J Cardiol*. 2003;92:554-60.
83. Gorcsan J, 3rd, Kanzaki H, Bazaz R, Dohi K, Schwartzman D. Usefulness of echocardiographic tissue synchronization imaging to predict acute response to cardiac resynchronization therapy. *Am J Cardiol*. 2004;93:1178-81.
84. Yu CM, Fung JW, Zhang Q, Chan CK, Chan YS, Lin H, Kum LC, Kong SL, Zhang Y, Sanderson JE. Tissue Doppler imaging is superior to strain rate imaging and postsystolic shortening on the prediction of reverse remodeling in both ischemic and nonischemic heart failure after cardiac resynchronization therapy. *Circulation*. 2004;110:66-73.
85. Yu CM, Zhang Q, Fung JW, Chan HC, Chan YS, Yip GW, Kong SL, Lin H, Zhang Y, Sanderson JE. A novel tool to assess systolic asynchrony and identify responders of cardiac resynchronization therapy by tissue synchronization imaging. *J Am Coll Cardiol*. 2005;45:677-684.
86. Lafitte S, Bordachar P, Lafitte M, Garrigue S, Reuter S, Reant P, Serri K, Lebouffos V, Berrhouet M, Jais P, Haissaguerre M, Clementy J, Roudaut R, DeMaria AN. Dynamic ventricular dyssynchrony: an exercise-echocardiography study. *J Am Coll Cardiol*. 2006;47:2253-9.
87. Reichek N. MRI myocardial tagging. *J Magn Reson Imaging*. 1999;10:609-16.
88. Axel L, Dougherty L. MR imaging of motion with spatial modulation of magnetization. *Radiology*. 1989;171:841-5.
89. McVeigh ER. MRI of Myocardial Function: Motion Tracking Techniques. *Magnetic Resonance Imaging*. 1996;14:137-150.

90. Lardo AC, Abraham TP, Kass DA. Magnetic resonance imaging assessment of ventricular dyssynchrony: current and emerging concepts. *J Am Coll Cardiol*. 2005;46:2223-8.
91. Osman NF, Prince JL. Regenerating MR tagged images using harmonic phase (HARP) methods. *IEEE Trans Biomed Eng*. 2004;51:1428-33.
92. Osman NF, Kerwin WS, McVeigh ER, Prince JL. Cardiac motion tracking using CINE harmonic phase (HARP) magnetic resonance imaging. *Magn Reson Med*. 1999;42:1048-60.
93. Pelc NJ, Bernstein MA, Shimakawa A, Glover GH. Encoding strategies for three-direction phase-contrast MR imaging of flow. *J Magn Reson Imaging*. 1991;1:405-413.
94. Pelc NJ, Herfkens RJ, Shimakawa A, Enzmann DR. Phase contrast cine magnetic resonance imaging. *Magn Reson Q*. 1991;7:229-254.
95. van Dijk P. Direct cardiac NMR imaging of heart wall and blood flow velocity. *J Comput Assist Tomogr*. 1984;8:429-436.
96. Vick G, Cheung T, Beerbaum P, Muthupillai R. Role of MR flow imaging in assessing congenital heart disease. *MEDICAMUNDI*. 2002;46:53-58.
97. Aletras AH, Ding S, Balaban RS, Wen H. DENSE: displacement encoding with stimulated echoes in cardiac functional MRI. *J Magn Reson*. 1999;137:247-52.
98. Kim D, Gilson WD, Kramer CM, Epstein FH. Myocardial tissue tracking with two-dimensional cine displacement-encoded MR imaging: development and initial evaluation. *Radiology*. 2004;230:862-71.
99. Kim D, Epstein FH, Gilson WD, Axel L. Increasing the signal-to-noise ratio in DENSE MRI by combining displacement-encoded echoes. *Magn Reson Med*. 2004;52:188-92.
100. Pelc NJ, Drangova M, Pelc LR, Zhu Y, Noll DC, Bowman BS, Herfkens RJ. Tracking of cyclic motion with phase-contrast cine MR velocity data. *J Magn Reson Imaging*. 1995;5:339-345.
101. D'Hooge J, Heimdal A, Jamal F, Kukulski T, Bijnens B, Rademakers F, Hatle L, Suetens P, Sutherland GR. Regional strain and strain rate measurements by cardiac ultrasound: principles, implementation and limitations. *Eur J Echocardiogr*. 2000;1:154-70.
102. Urheim S, Edvardsen T, Torp H, Angelsen B, Smiseth OA. Myocardial strain by Doppler echocardiography. Validation of a new method to quantify regional myocardial function. *Circulation*. 2000;102:1158-64.
103. Sutherland GR, Di Salvo G, Claus P, D'Hooge J, Bijnens B. Strain and strain rate imaging: a new clinical approach to quantifying regional myocardial function. *J Am Soc Echocardiogr*. 2004;17:788-802.
104. Voigt JU, Arnold MF, Karlsson M, Hubbert L, Kukulski T, Hatle L, Sutherland GR. Assessment of regional longitudinal myocardial strain rate derived from doppler myocardial imaging indexes in normal and infarcted myocardium. *J Am Soc Echocardiogr*. 2000;13:588-98.
105. Jamal F, Strotmann J, Weidemann F, Kukulski T, D'Hooge J, Bijnens B, Van de Werf F, De Scheerder I, Sutherland GR. Noninvasive quantification of the contractile reserve of stunned myocardium by ultrasonic strain rate and strain. *Circulation*. 2001;104:1059-65.

106. Armstrong G, Pasquet A, Fukamachi K, Cardon L, Olstad B, Marwick T. Use of peak systolic strain as an index of regional left ventricular function: comparison with tissue Doppler velocity during dobutamine stress and myocardial ischemia. *J Am Soc Echocardiogr*. 2000;13:731-7.
107. Galderisi M, Mele D, Marino PN. Quantitation of stress echocardiography by tissue Doppler and strain rate imaging: a dream come true? *Ital Heart J*. 2005;6:9-20.
108. Hashimoto I, Li X, Hejmadi Bhat A, Jones M, Zetts AD, Sahn DJ. Myocardial strain rate is a superior method for evaluation of left ventricular subendocardial function compared with tissue Doppler imaging. *J Am Coll Cardiol*. 2003;42:1574-83.
109. Pierre-Justin G, Lancellotti P, Pierard LA. What indices quantify regional myocardial function during supine bicycle in healthy subject: natural strain and strain rate? *Int J Cardiol*. 2005;102:21-31.
110. Dohi K, Pinsky MR, Kanzaki H, Severyn D, Gorcsan J, 3rd. Effects of radial left ventricular dyssynchrony on cardiac performance using quantitative tissue Doppler radial strain imaging. *J Am Soc Echocardiogr*. 2006;19:475-82.
111. Dohi K, Suffoletto MS, Schwartzman D, Ganz L, Pinsky MR, Gorcsan J, 3rd. Utility of echocardiographic radial strain imaging to quantify left ventricular dyssynchrony and predict acute response to cardiac resynchronization therapy. *Am J Cardiol*. 2005;96:112-6.
112. Gilman G, Khandheria BK, Hagen ME, Abraham TP, Seward JB, Belohlavek M. Strain rate and strain: a step-by-step approach to image and data acquisition. *J Am Soc Echocardiogr*. 2004;17:1011-20.
113. Hashimoto I, Mori Y, Rusk RA, Davies CH, Li X, Mack GK, Sahn DJ. Strain rate imaging: an in vitro "validation" study using a physiologic balloon model mimicking the left ventricle. *Echocardiography*. 2002;19:669-77.
114. Ehman RL, Felmlee JP. Adaptive technique for high-definition MR imaging of moving structures. *Radiology*. 1989;173:255-63.
115. Wang Y, Rossman PJ, Grimm RC, Riederer SJ, Ehman RL. Navigator-echo-based real-time respiratory gating and triggering for reduction of respiration effects in three-dimensional coronary MR angiography. *Radiology*. 1996;198:55-60.
116. Oshinski JN, Hofland L, Mukundan S, Jr., Dixon WT, Parks WJ, Pettigrew RI. Two-dimensional coronary MR angiography without breath holding. *Radiology*. 1996;201:737-43.
117. Atalay MK, Poncelet BP, Kantor HL, Brady TJ, Weisskoff RM. Cardiac susceptibility artifacts arising from the heart-lung interface. *Magn Reson Med*. 2001;45:341-5.
118. Reeder SB, Faranesh AZ, Boxerman JL, McVeigh ER. In vivo measurement of T*2 and field inhomogeneity maps in the human heart at 1.5 T. *Magn Reson Med*. 1998;39:988-98.
119. Felmlee JP, Ehman RL. Spatial presaturation: a method for suppressing flow artifacts and improving depiction of vascular anatomy in MR imaging. *Radiology*. 1987;164:559-64.

120. Pruessmann KP, Weiger M, Scheidegger MB, Boesiger P. SENSE: sensitivity encoding for fast MRI. *Magn Reson Med*. 1999;42:952-62.

121. Delfino J, Johnson K, Eisner R, Eder S, Leon A, Oshinski J. Three Directional Myocardial Phase Contrast Tissue Velocity Imaging without Breath Holding: An in-vivo and in-vitro study. *Radiology*. in press.

122. Haacke EM, Brown RW, Thompson MR, Venkatesan R. *Magnetic Resonance Imaging: Physical Principles and Sequence Design*. New York: John Wiley and Sons, Inc; 1999.

123. Forster J, Sieverding L, Breuer J, Schick F, Dammann F, Apitz J, Lutz O. High-resolution cardiac imaging using an interleaved 3D double slab technique. *Magn Reson Imaging*. 1998;16:1155-1162.

124. Nayak KS, Rivas PA, Pauly JM, Scott GC, Kerr AB, Hu BS, Nishimura DG. Real-time black-blood MRI using spatial presaturation. *J Magn Reson Imaging*. 2001;13:807-812.

125. Wolf RL, Ehman RL, Riederer SJ, Rossman PJ. Analysis of systematic and random error in MR volumetric flow measurements. *Magn Reson Med*. 1993;30:82-91.

126. Markl M, Bammer R, Alley MT, Elkins CJ, Draney MT, Barnett A, Moseley ME, Glover GH, Pelc NJ. Generalized reconstruction of phase contrast MRI: analysis and correction of the effect of gradient field distortions. *Magn Reson Med*. 2003;50:791-801.

127. Bernstein MA, Zhou XJ, Polzin JA, King KF, Ganin A, Pelc NJ, Glover GH. Concomitant gradient terms in phase contrast MR: analysis and correction. *Magn Reson Med*. 1998;39:300-8.

128. Norris DG, Hutchison JM. Concomitant magnetic field gradients and their effects on imaging at low magnetic field strengths. *Magn Reson Imaging*. 1990;8:33-7.

129. Vaals JV, Bergman A. Optimization of Eddy-Current Compensation. *Journal of Magnetic Resonance* 1990;90:52-70.

130. Walker PG, Cranney GB, Scheidegger MB, Waseleski G, Pohost GM, Yoganathan AP. Semiautomated method for noise reduction and background phase error correction in MR phase velocity data. *J Magn Reson Imaging*. 1993;3:521-530.

131. Constable RT, Rath KM, Sinusas AJ, Gore JC. Development and evaluation of tracking algorithms for cardiac wall motion analysis using phase velocity MR imaging. *Magn Reson Med*. 1994;32:33-42.

132. Lingamneni A, Hardy PA, Powell KA, Pelc NJ, White RD. Validation of cine phase-contrast MR imaging for motion analysis. *J Magn Reson Imaging*. 1995;5:331-8.

133. Drangova M, Zhu Y, Bowman B, Pelc NJ. In vitro verification of myocardial motion tracking from phase-contrast velocity data. *Magn Reson Imaging*. 1998;16:863-70.

134. Pelc LR, Sayre J, Yun K, Castro LJ, Herfkens RJ, Miller DC, Pelc NJ. Evaluation of myocardial motion tracking with cine-phase contrast magnetic resonance imaging. *Invest Radiol*. 1994;29:1038-1042.

135. Cerqueira MD, Weissman NJ, Dilsizian V, Jacobs AK, Kaul S, Laskey WK, Pennell DJ, Rumberger JA, Ryan T, Verani MS. Standardized myocardial

segmentation and nomenclature for tomographic imaging of the heart: a statement for healthcare professionals from the Cardiac Imaging Committee of the Council on Clinical Cardiology of the American Heart Association. *Circulation*. 2002;105:539-42.

136. Chu KC, Rutt BK. Polyvinyl alcohol cryogel: an ideal phantom material for MR studies of arterial flow and elasticity. *Magn Reson Med*. 1997;37:314-9.
137. Bland JM, Altman DG. Statistical methods for assessing agreement between two methods of clinical measurement. *Lancet*. 1986;1:307-310.
138. Streif JU, Herold V, Szimtenings M, Lanz TE, Nahrendorf M, Wiesmann F, Rommel E, Haase A. In vivo time-resolved quantitative motion mapping of the murine myocardium with phase contrast MRI. *Magn Reson Med*. 2003;49:315-321.
139. Dulce MC, Mostbeck GH, O'Sullivan M, Cheitlin M, Caputo GR, Higgins CB. Severity of aortic regurgitation: interstudy reproducibility of measurements with velocity-encoded cine MR imaging. *Radiology*. 1992;185:235-240.
140. Chatzimavroudis GP, Oshinski JN, Franch RH, Walker PG, Yoganathan AP, Pettigrew RI. Evaluation of the precision of magnetic resonance phase velocity mapping for blood flow measurements. *J Cardiovasc Magn Reson*. 2001;3:11-19.
141. Firmin DN, Nayler GL, Klipstein RH, Underwood SR, Rees RS, Longmore DB. In vivo validation of MR velocity imaging. *J Comput Assist Tomogr*. 1987;11:751-6.
142. Bryant DJ, Payne JA, Firmin DN, Longmore DB. Measurement of flow with NMR imaging using a gradient pulse and phase difference technique. *J Comput Assist Tomogr*. 1984;8:588-93.
143. Summers PE, Holdsworth DW, Nikolov HN, Rutt BK, Drangova M. Multisite trial of MR flow measurement: phantom and protocol design. *J Magn Reson Imaging*. 2005;21:620-31.
144. Zhu Y, Drangova M, Pelc NJ. Fourier tracking of myocardial motion using cine-PC data. *Magn Reson Med*. 1996;35:471-80.
145. Zhu Y, Pelc NJ. Three-dimensional motion tracking with volumetric phase contrast MR velocity imaging. *J Magn Reson Imaging*. 1999;9:111-8.
146. Zhou Y, Carroll TJ, Grist TM, Frayne R. Design and validation of a motion stage for in vitro MR experiments. *J Magn Reson Imaging*. 1999;10:972-7.
147. Arai AE, Gaither CC, 3rd, Epstein FH, Balaban RS, Wolff SD. Myocardial velocity gradient imaging by phase contrast MRI with application to regional function in myocardial ischemia. *Magn Reson Med*. 1999;42:98-109.
148. Drangova M, Bowman B, Pelc N. Physiologic motion phantom for MRI applications. *J Magn Reson Imaging*. 1996;6:513-8.
149. Young AA, Axel L, Dougherty L, Bogen DK, Parenteau CS. Validation of tagging with MR imaging to estimate material deformation. *Radiology*. 1993;188:101-8.
150. Kvitting JP, Ebbers T, Engvall J, Sutherland GR, Wranne B, Wigstrom L. Three-directional myocardial motion assessed using 3D phase contrast MRI. *J Cardiovasc Magn Reson*. 2004;6:627-636.
151. Bax JJ, Molhoek SG, van Erven L, Voogd PJ, Somer S, Boersma E, Steendijk P, Schalij MJ, Van der Wall EE. Usefulness of myocardial tissue Doppler

echocardiography to evaluate left ventricular dyssynchrony before and after biventricular pacing in patients with idiopathic dilated cardiomyopathy. *Am J Cardiol*. 2003;91:94-7.

152. Garrigue S, Reuter S, Labeque JN, Jais P, Hocini M, Shah DC, Haissaguerre M, Clementy J. Usefulness of biventricular pacing in patients with congestive heart failure and right bundle branch block. *Am J Cardiol*. 2001;88:1436-41, A8.
153. Walker A, Olsson E, Wranne B, Ringqvist I, Ask P. Accuracy of spectral Doppler flow and tissue velocity measurements in ultrasound systems. *Ultrasound Med Biol*. 2004;30:127-132.
154. Miyatake K, Yamagishi M, Tanaka N, Uematsu M, Yamazaki N, Mine Y, Sano A, Hirama M. New method for evaluating left ventricular wall motion by color-coded tissue Doppler imaging: in vitro and in vivo studies. *J Am Coll Cardiol*. 1995;25:717-724.
155. Jung B, Schneider B, Markl M, Saurbier B, Geibel A, Hennig J. Measurement of left ventricular velocities: phase contrast MRI velocity mapping versus tissue-doppler-ultrasound in healthy volunteers. *J Cardiovasc Magn Reson*. 2004;6:777-783.
156. Paelinck BP, de Roos A, Bax JJ, Bosmans JM, van Der Geest RJ, Dhondt D, Parizel PM, Vrints CJ, Lamb HJ. Feasibility of tissue magnetic resonance imaging: a pilot study in comparison with tissue Doppler imaging and invasive measurement. *J Am Coll Cardiol*. 2005;45:1109-16.
157. Markl M, Schneider B, Hennig J. Fast phase contrast cardiac magnetic resonance imaging: improved assessment and analysis of left ventricular wall motion. *J Magn Reson Imaging*. 2002;15:642-653.
158. Stuber M, Scheidegger MB, Fischer SE, Nagel E, Steinemann F, Hess OM, Boesiger P. Alterations in the local myocardial motion pattern in patients suffering from pressure overload due to aortic stenosis. *Circulation*. 1999;100:361-8.
159. Hansen DE, Daughters GT, 2nd, Alderman EL, Stinson EB, Baldwin JC, Miller DC. Effect of acute human cardiac allograft rejection on left ventricular systolic torsion and diastolic recoil measured by intramyocardial markers. *Circulation*. 1987;76:998-1008.
160. Yu CM, Bax JJ, Monaghan M, Nihoyannopoulos P. Echocardiographic evaluation of cardiac dyssynchrony for predicting a favourable response to cardiac resynchronisation therapy. *Heart*. 2004;90 Suppl 6:vi17-vi22.
161. Oxenham HC, Young AA, Cowan BR, Gentles TL, Occleshaw CJ, Fonseca CG, Doughty RN, Sharpe N. Age-related changes in myocardial relaxation using three-dimensional tagged magnetic resonance imaging. *J Cardiovasc Magn Reson*. 2003;5:421-30.
162. Vembar M, Garcia MJ, Heuscher DJ, Haberl R, Matthews D, Bohme GE, Greenberg NL. A dynamic approach to identifying desired physiological phases for cardiac imaging using multislice spiral CT. *Med Phys*. 2003;30:1683-93.
163. Hanekom L, Lundberg V, Leano R, Marwick TH. Optimisation of strain rate imaging for application to stress echocardiography. *Ultrasound Med Biol*. 2004;30:1451-60.

164. D'hooge J, Jamal F, Bijnens B, Heimdal A, Thoen J, Werf FVd, Sutherland GR, Suetens P. Calculation of Strain Values from Strain Rate Curves: How Should This be Done? *IEEE Ultrasonics Symposium*. 2000:1269-1272.
165. Edvardsen T, Gerber BL, Garot J, Bluemke DA, Lima JA, Smiseth OA. Quantitative assessment of intrinsic regional myocardial deformation by Doppler strain rate echocardiography in humans: validation against three-dimensional tagged magnetic resonance imaging. *Circulation*. 2002;106:50-6.
166. Serri K, Reant P, Lafitte M, Berhouet M, Le Bouffos V, Roudaut R, Lafitte S. Global and regional myocardial function quantification by two-dimensional strain: application in hypertrophic cardiomyopathy. *J Am Coll Cardiol*. 2006;47:1175-81.
167. Kowalski M, Kukulski T, Jamal F, D'Hooge J, Weidemann F, Rademakers F, Bijnens B, Hatle L, Sutherland GR. Can natural strain and strain rate quantify regional myocardial deformation? A study in healthy subjects. *Ultrasound Med Biol*. 2001;27:1087-97.
168. Azhari H, Weiss JL, Rogers WJ, Siu CO, Zerhouni EA, Shapiro EP. Noninvasive quantification of principal strains in normal canine hearts using tagged MRI images in 3-D. *Am J Physiol*. 1993;264:H205-16.
169. Rademakers FE, Rogers WJ, Guier WH, Hutchins GM, Siu CO, Weisfeldt ML, Weiss JL, Shapiro EP. Relation of regional cross-fiber shortening to wall thickening in the intact heart. Three-dimensional strain analysis by NMR tagging. *Circulation*. 1994;89:1174-82.
170. Matre K, Fannelop T, Dahle GO, Heimdal A, Grong K. Radial strain gradient across the normal myocardial wall in open-chest pigs measured with doppler strain rate imaging. *J Am Soc Echocardiogr*. 2005;18:1066-73.
171. Tseng WY, Reese TG, Weisskoff RM, Brady TJ, Wedeen VJ. Myocardial fiber shortening in humans: initial results of MR imaging. *Radiology*. 2000;216:128-39.
172. MacGowan GA, Shapiro EP, Azhari H, Siu CO, Hees PS, Hutchins GM, Weiss JL, Rademakers FE. Noninvasive measurement of shortening in the fiber and cross-fiber directions in the normal human left ventricle and in idiopathic dilated cardiomyopathy. *Circulation*. 1997;96:535-41.
173. Weidemann F, Jamal F, Sutherland GR, Claus P, Kowalski M, Hatle L, De Scheerder I, Bijnens B, Rademakers FE. Myocardial function defined by strain rate and strain during alterations in inotropic states and heart rate. *Am J Physiol Heart Circ Physiol*. 2002;283:H792-9.
174. Beache GM, Wedeen VJ, Weisskoff RM, O'Gara PT, Poncelet BP, Chesler DA, Brady TJ, Rosen BR, Dinsmore RE. Intramural mechanics in hypertrophic cardiomyopathy: functional mapping with strain-rate MR imaging. *Radiology*. 1995;197:117-24.
175. Amundsen BH, Helle-Valle T, Edvardsen T, Torp H, Crosby J, Lyseggen E, Stoylen A, Ihlen H, Lima JA, Smiseth OA, Slordahl SA. Noninvasive myocardial strain measurement by speckle tracking echocardiography: validation against sonomicrometry and tagged magnetic resonance imaging. *J Am Coll Cardiol*. 2006;47:789-93.
176. Toyoda T, Baba H, Akasaka T, Akiyama M, Neishi Y, Tomita J, Sukmawan R, Koyama Y, Watanabe N, Tamano S, Shinomura R, Komuro I, Yoshida K.

Assessment of regional myocardial strain by a novel automated tracking system from digital image files. *J Am Soc Echocardiogr*. 2004;17:1234-8.

177. Sampath S, Derbyshire JA, Atalar E, Osman NF, Prince JL. Real-time imaging of two-dimensional cardiac strain using a harmonic phase magnetic resonance imaging (HARP-MRI) pulse sequence. *Magn Reson Med*. 2003;50:154-63.

178. Zhu Y, Drangova M, Pelc NJ. Estimation of deformation gradient and strain from cine-PC velocity data. *IEEE Trans Med Imaging*. 1997;16:840-51.

179. Gorcsan J, 3rd, Deswal A, Mankad S, Mandarino WA, Mahler CM, Yamazaki N, Katz WE. Quantification of the myocardial response to low-dose dobutamine using tissue Doppler echocardiographic measures of velocity and velocity gradient. *Am J Cardiol*. 1998;81:615-23.

180. Fornwalt B, Arita T, Bhasin M, Voulgaris G, Merlino J, Leon A, Fyfe D, Oshinski J. Cross-correlation quantification of dyssynchrony: a new method for quantifying the synchrony of contraction and relaxation in the heart. *J Am Soc Echocardiogr*. 2007;in press.